Mathematics of Super-Resolution Biomedical Imaging

Tutorials

Giovanni S. Alberti, Habib Ammari and Francisco Romero
(version (19.04.2018) with corrections by A. Dabrowski)

Contents

CHAPTER 1

Basic mathematical concepts

1.1. The singular value decomposition

1.1.1. Basic properties. Let H and K be Hilbert spaces. We saw in the lecture notes (§2.6) that a compact operator $A\colon H \to K$ may be expanded with the singular value decomposition as

$$Af = \sum_{l \in L} \sigma_l (f, f_l)_H \, g_l, \tag{1.1}$$

where:

- L is either a finite set or $L = \mathbb{N}$;
- $\sigma_l > 0$ are called singular values, and form a non-increasing sequence converging to 0 (if $L = \mathbb{N}$);
- $\{f_l\}_l$ and $\{g_l\}_l$ are called right and left singular vectors, and are orthonormal systems of H and K, respectively.

In other words, the action of the operator A on a vector f may be described as follows: the component of f along f_l is mapped into g_l, with a weight σ_l.

EXAMPLE 1.1. Let $H = L^2([0,1])$ and $A\colon H \to H$ be defined by

$$Af(t) = \int_0^t f(s)\, ds, \qquad f \in H. \tag{1.2}$$

By the Ascoli-Arzelà theorem, A is compact. The adjoint of A is given by

$$A^* g(s) = \int_s^1 g(t)\, dt.$$

In order to compute the singular values and the singular vectors, we need to consider the equation $A^*Af = \lambda f$, namely

$$\int_s^1 \int_0^t f(\tau)\, d\tau dt = \lambda f(s).$$

It immediately follows that $f(1) = 0$. Moreover, differentiating this identity yields

$$-\int_0^s f(\tau)\, d\tau = \lambda f'(s).$$

Arguing as before, we obtain $f'(0) = 0$ and $\lambda f''(s) + f(s) = 0$. To sum up, we have obtained

$$\begin{cases} \lambda f'' + f = 0 \quad \text{in (0,1)}, \\ f(1) = 0, \\ f'(0) = 0. \end{cases}$$

This eigenvalue problem may be easily solved. The solutions are given by

$$\lambda_l = \sigma_l^2 = \frac{4}{(2l-1)^2\pi^2}, \qquad f_l(s) = \sqrt{2}\cos(\sigma_l^{-1}s), \qquad l \in \mathbb{N}^*. \tag{1.3}$$

Finally, the identity $Af_l = \sigma_l g_l$ yields

$$g_l(t) = \sqrt{2}\sin(\sigma_l^{-1}t), \qquad l \in \mathbb{N}^*. \tag{1.4}$$

1.1.2. Solving inverse problems with the SVD. The SVD of an operator is very useful when solving equation of the form $Af = g$, where g is known and f is the unknown of the problem. In many inverse problems, the governing operator A is compact.

Suppose for simplicity that the problem has a unique solution. Then, writing $g = \sum_l (g, g_l)_K g_l$, in view of (1.1) we obtain

$$\sum_{l\in L}(g, g_l)_K g_l = g = Af = \sum_{l\in L}\sigma_l(f, f_l)_H g_l.$$

Therefore, since the g_ls are linearly independent we obtain $(f, f_l)_H = \sigma_l^{-1}(g, g_l)_K$, whence

$$f = \sum_{l\in L}\sigma_l^{-1}(g, g_l)_K f_l. \tag{1.5}$$

The above identity gives an explicit solution of $Af = g$ in terms of the scalar products of g with the singular vectors g_l.

Suppose now that H and K are infinite dimensional, with A compact and $L = \mathbb{N}^*$. From the theory, we already know that A cannot have a continuous inverse[1]. This can be clearly seen in (1.5): since $\sigma_l \to 0$, very small perturbation in $(g, g_l)_K$ for large l will result in arbitrary large changes in f. In this case, we say that the problem is ill-posed. The asymptotic behaviour of the singular values at infinity tells us how severe the ill-posedness is: the faster the decay, the more unstable the reconstruction becomes.

EXAMPLE 1.2. Let us reconsider the operator introduced in the previous example:

$$Af(t) = \int_0^t f(s)\,ds, \qquad f \in H.$$

The equation $Af = g$ has the trivial solution $f = g'$. However, this operation is not stable, as we now see. Consider the sequence of functions

$$g_j(t) = \frac{\sin(jt)}{j}, \qquad j \in \mathbb{N}^*.$$

We have $g_j \to 0$ in H but $g_j' = \cos(\cdot/j) \not\to 0$ in H. In other words, if we look at g_j as being small noise added to zero, the inversion stays away from zero even if the noise level goes to zero.

Formula (1.5) allows us to gain some insight into this issue. Using (1.3) and (1.4) we obtain

$$f(s) = 2\sum_{l\in\mathbb{N}}\sigma_l^{-1}(g, \sin(\sigma_l^{-1}\cdot))_2\cos(\sigma_l^{-1}s), \qquad \sigma_l = \frac{2}{(2l-1)\pi}.$$

[1] If A had a continuous inverse A^{-1}, then $I = AA^{-1}$ would be a compact operator, which would imply that $\dim K < \infty$.

The terms $(g, \sin(\sigma_l^{-1}\cdot))_2$ can be seen as Fourier coefficients of g at frequency $\sim \sigma_l^{-1}$. We noted before that the instabilities arise as $l \to \infty$, since $\sigma_l^{-1} \to \infty$. Therefore, instabilities arise at high frequencies: differentiating high frequencies components is an unstable process. This is perfectly consistent with the example we discussed above: the functions g_j contain higher and higher frequencies as $j \to \infty$.

1.1.3. Regularisation by truncation. In the above example, we showed that differentiation corresponds to inverting a compact operator, and is therefore an unstable process. In other words, if small noise is added to our datum, large errors may appear during the inversion. Thanks to the SVD decomposition, we saw that the largest instabilities arise at high frequencies, namely as $l \to \infty$, since $\sigma_l^{-1} \to \infty$. In order to solve this issue, a very natural idea is to truncate expansion (1.5) to

$$f = \sum_{l:\sigma_l^{-1} \geq \gamma} \sigma_l^{-1} (g, g_l)_K f_l,$$

for some $\gamma > 0$. In this way, the contributions coming from high values of σ_l^{-1} are simply discarded: this makes the reconstruction more stable. Note that this formula may be equivalently rewritten as

$$f = \sum_{l=1}^{l^*} \sigma_l^{-1} (g, g_l)_K f_l, \tag{1.6}$$

for some $l^* \in \mathbb{N}$.

EXAMPLE 1.3. We consider again the previous example about integration and differentiation, and apply this regularisation technique. We use Matlab. In order to discretise the problem, we approximate $L^2([0,1])$ with $\mathbb{R}^N$ with the map

$$f \in L^2([0,1]) \mapsto (f((i-1)/(N-1)))_i \in \mathbb{R}^N.$$

(In the implementation, we set $N = 200$.) The operator in (1.2) can be represented by the matrix $A \in \mathbb{R}^{N,N}$ given by

$$A = N^{-1} \begin{bmatrix} 1 & 0 & \cdots & 0 \\ 1 & 1 & \ddots & \vdots \\ \vdots & \ddots & \ddots & 0 \\ 1 & \cdots & 1 & 1 \end{bmatrix}.$$

Indeed, we are approximating the integral of f with a simple weighted sum of the entries of the vector. The numerical implementation of the approach for the function $g(t) = 3t^3 - 2t^2$ is presented in Listing 1.1, to which we refer for the details. Here we briefly comment the results.

We use white Gaussian noise, so that the relative error of the measurement is about 1%. The reconstruction with no regularisation is shown in Figure 1.1a (namely, with $l^* = N = 200$), and the reconstruction done using only the first $l^* = 50$ terms in (1.6) is shown in Figure 1.1b. Note that, in view of (1.3) and (1.4), (1.6) corresponds to performing a low-pass filter to g before differentiating it.

The relative error of the reconstruction as a function of the truncation level in (1.6) is shown in Figure 1.2.

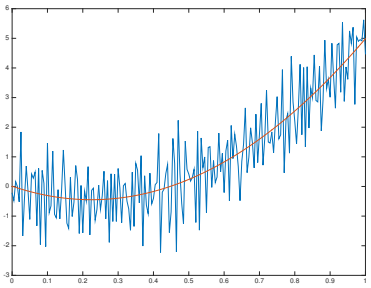

(A) The direct differentiation of the noisy version of g.

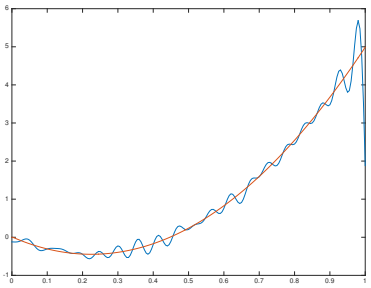

(B) The truncated SVD method for the differentiation of g.

FIGURE 1.1. The truncated SVD method.

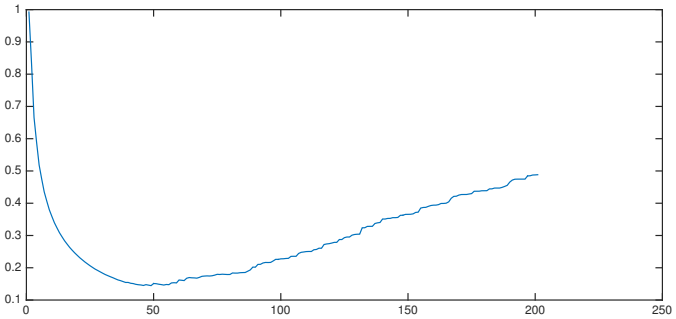

FIGURE 1.2. The relative error of the reonstruction as a function of the number of singular values used.

LISTING 1.1. Code for Example 1.3.

```
%% 1. Exact differentiation
clear
N = 200;
step = 1/(N-1);
T = [0:step:1]';
g = 3*T.^3 - 2*T.^2;

figure
subplot(2,3,1)
plot(T,g); axis([0 1 -.2 1.1])
title('g(t) = 3t^3 - 2t^2')
subplot(2,3,4)
plot(T(1:end-1),diff(g)/step,'r'); axis([0 1 -2 6])
title('g''(t)')

%% 2. Noisy case
```

```
17
18 err = randn(N,1)/300; % White Gaussian noise
19 g_err = g + err;
20
21 subplot(2,3,2)
22 plot(T,g_err); axis([0 1 -.2 1.1])
23 title(['g_e = g + noise. Rel. error = ',sprintf('%.3f',norm(err)/norm(g)),
       '.'])
24 subplot(2,3,5)
25 plot(T(1:end-1),diff(g_err)/step); axis([0 1 -2 6])
26 title('g_e' by direct differentiation')
27
28 %% 3. Inversion of the matrix and SVD
29
30 A = zeros(N,N);
31 for i = 1:N
32     for l = 1:i
33         A(i,l) = 1/N;
34     end
35 end
36 freal = A\g;
37
38 subplot(2,3,3)
39 plot(T,A\g_err,T,freal); axis([0 1 -2 6])
40 title('g_e' by inverting A')
41
42 [U,S,V] = svd(A);
43 f = zeros(N,1);
44 for l = 1:N
45     f = f + dot(g_err,U(:,l))*V(:,l)/S(l,l);
46 end
47
48 subplot(2,3,6)
49 plot(T,f,T,freal); axis([0 1 -2 6])
50 title('g_e' by inverting A with SVD')
51
52 %% 4. Regularization by truncation of the SVD
53
54 f = zeros(N,1); error = f;
55
56 figure
57 for l = 1:50
58     f = f + dot(g_err,U(:,l))*V(:,l)/S(l,l);
59     subplot(1,2,1)
60     plot(T,f,T,freal); axis([0 1 -2 6])
61     error(l) = norm(f-freal)/norm(freal);
62     title(['l <= ',num2str(l),'. Rel. error = ',num2str(error(l))])
63     subplot(1,2,2)
64     plot(error(1:l)); axis([1 N 0 1])
65     title('Relative error as a function of the number of \sigma_l')
66     pause(1/sqrt(l))
67 end
```

1.1.4. Tikhonov regularisation. It is worth pointing out that the regularisation by truncation of the SVD is almost equivalent with Tikhonov regularisation. Using the above notation, suppose that we want to solve the inverse problem $Af = g$. As explained in the lecture notes, Tikhonov regularisation consists in the minimisation of the functional

$$\min_{f\in H} \|Af - g\|_K^2 + \alpha\|f\|_H^2, \tag{1.7}$$

for some regularisation parameter $\alpha > 0$. The case $\alpha = 0$ corresponds to the direct inversion of A without regularisation.

The SVD decomposition allows us to find an explicit expression of the minimiser. Indeed, write

$$Af = \sum_{l\in L} \sigma_l (f, f_l)_H \, g_l, \qquad f = \sum_{l\in L} (f, f_l)_H \, f_l, \qquad g = \sum_{l\in L} (g, g_l)_K \, g_l.$$

We are now looking for an expression of $(f, f_l)_H$ in terms of $(g, g_l)_K$. For simplicity, write $(f, f_l)_H = x_l (g, g_l)_K$ for some unknown x_l to be determined. By the Pythagorean theorem for Hilbert spaces, since $\{f_l\}_l$ and $\{g_l\}_l$ are orthonormal systems of H and K, we obtain

$$\begin{aligned}
\|Af - g\|_K^2 + \alpha\|f\|_H^2 &= \|\sum_{l\in L} (\sigma_l (f, f_l)_H - (g, g_l)_K) g_l\|_K^2 + \alpha \|\sum_{l\in L} (f, f_l)_H \, f_l\|_H^2 \\
&= \sum_{l\in L} (\sigma_l (f, f_l)_H - (g, g_l)_K)^2 + \alpha (f, f_l)_H^2 \\
&= \sum_{l\in L} (\sigma_l x_l (g, g_l)_K - (g, g_l)_K)^2 + \alpha x_l^2 (g, g_l)_K^2 \\
&= \sum_{l\in L} (g, g_l)_K^2 \left((\sigma_l x_l - 1)^2 + \alpha x_l^2 \right).
\end{aligned}$$

Therefore, the minimisation of (1.7) boils down to finding, for each l, the minimum of the function $w_l(x) = (\sigma_l x - 1)^2 + \alpha x^2$. Since $w_l'(x) = 2((\sigma_l^2 + \alpha)x - 2\sigma_l$, we obtain $x_l = \frac{\sigma_l}{\sigma_l^2 + \alpha}$, whence

$$(f, f_l)_H = \frac{\sigma_l}{\sigma_l^2 + \alpha} (g, g_l)_K.$$

As a consequence, the solution of the minimisation problem (1.7) is given by

$$f = \sum_{l\in L} \frac{\sigma_l}{\sigma_l^2 + \alpha} (g, g_l)_K f_l.$$

Note that, for $\alpha = 0$, this formula reduces to (1.5): this is expected, since in this case there is no regularisation performed. On the other hand, for $\alpha > 0$, this formula is similar to (1.6). Indeed, for $\sigma_l \gg \alpha$, we have $\frac{\sigma_l}{\sigma_l^2 + \alpha} \approx \sigma_l^{-1}$ and for $\sigma_l \ll \alpha$ we have $\frac{\sigma_l}{\sigma_l^2 + \alpha} \approx 0$.

1.2. Random medium generation

When working in some aspects of inverse problems, in particular in medical imaging, it is often of great need to have realistic models for the coefficients that arise for each problem. Biological tissues in reality are not deterministic nor constant, so a good model to approximate clinical examples includes randomness and uncertainty.

We want to be able to generate random media, with predefined statistics, to produce examples of data for forwards models, and afterwards test any inverse problem's stability on it.

1.2.1. Fourier transform. We will need the isometric Fourier transform for $d \in \mathbb{N}$; it is defined as:

$$\hat{f}(\xi) = \frac{1}{(2\pi)^{d/2}} \int_{\mathbb{R}^d} f(x) e^{-ix\cdot\xi} dx.$$

To approximate its value in a fast fashion using Matlab, we will use the Fast Fourier transform algorithm already implemented in Matlab as function `fft.m`. The fast Fourier algorithm computes the discrete Fourier transform.

For the following we will consider $d = 1$, as for higher dimensions it extends naturally by iterating the Fourier transform in each dimension. Let $N \in \mathbb{N}$ be the amount of samples of a function, namely $f[j], j \in \{0, 1, \ldots, N-1\}$, then the **discrete Fourier transform** is

$$X_k = \sum_{j=0}^{N-1} f[j] \cdot e^{-2\pi i k j/N}, \quad k \in \{0, 1, \ldots, N-1\}$$

To approximate the Fourier transform we will assume a bounded function such that $\text{supp}(f) \subset (-a/2, a/2), a > 0$, then for equidistant samples in space $x_j = \frac{a}{N}(j - N/2), j \in \{0, 1, \ldots, N-1\}$ and frequency $\xi_k = \frac{2\pi}{a}(k - N/2), k \in \{0, 1, \ldots, N-1\}$, we have that

$$\hat{f}(\xi_k) \approx \frac{a}{N\sqrt{2\pi}} e^{-i\pi N/2} (-1)^k \sum_{j=0}^{N-1} f(x_j)(-1)^j e^{-i2\pi jk/N} \quad j, k \in \{0, 1, \ldots, N-1\}.$$

Where considering the vectors $\vec{f}_j = f(x_j) \in \mathbb{C}^N$, $(\pm 1)_j = (-1)^j, j \in \{0, 1, \ldots, N-1\}$ and the Matlab notation for point to point product $(a. * b)_j = a_j * b_j$, we can rewrite this expression as

$$\hat{\vec{f}} \approx \frac{a}{N\sqrt{2\pi}} e^{-i\pi N/2} (\pm 1). * DFT(\vec{f}. * (\pm 1)), \quad \text{where } \hat{\vec{f}}_k := \hat{f}(\xi_k),$$

with **DFT** the discrete fourier transform of the vector.

PROOF. Write the Fourier transform evaluated at ξ_k and approximate the integral of the Fourier transform evaluating the function in points x_j. Afterwards distribute terms. □

Remark: Notice that, to enhance the resolution of the Fourier transform, instead of needing to take more samples, it is needed to augment the support of the samples.

1.2.2. Continuous-time Gaussian white noise. Let $W_i \sim \mathcal{N}(0, 1)$ be a family of independent normally distributed random variables, for a fixed interval $[a, b]$ and $N \in \mathbb{N}$, consider the step $h_N = (b - a)/N$ and the grid $x_j^N = a + h(j + 1/2), j \in \{0, 1, \ldots, N-1\}$. We define the 1-dimensional continuous-time Gaussian white noise restricted to the interval $[a, b]$ as the distribution resulting from the following limit

$$W = \lim_{N\to\infty} \frac{1}{\sqrt{h_N}} \sum_{j=0}^{N-1} W_j \mathbb{1}_{[x_j^N - h/2, x_j^N + h/2]}(x).$$

For any smooth function f with support contained in $[a,b]$, we have that the integration against the Gaussian white noise is a normally distributed random variable with variance $||f||^2_{L^2(a,b)}$, i.e.

$$\int_a^b Wf(x)dx \sim \mathcal{N}(0, ||f||^2_{L^2(a,b)}).$$

PROOF. By definition the integral is

$$\begin{aligned}\int_a^b Wf(x)dx &= \lim_{N\to\infty} \frac{1}{\sqrt{h_N}} \sum_{j=0}^{N-1} W_j \int_a^b \mathbb{1}_{[x_j^N - h_N/2, x_j^N + h_N/2]}(x) f(x)dx \\ &= \lim_{N\to\infty} \frac{1}{\sqrt{h_N}} \sum_{j=0}^{N-1} W_j \int_{x_j^N - h_N/2}^{x_j^N + h_N/2} f(x)dx \\ &\sim \mathcal{N}\left(0, \lim_{N\to\infty} h_N \sum_{j=0}^{N-1} \left(\frac{1}{h_N} \int_{x_j^N - h_N/2}^{x_j^N + h_N/2} f(x)dx\right)^2\right).\end{aligned}$$

Since $h_N^{-1} \int_{x_j^N - h_N/2}^{x_j^N + h_N/2} f(x)dx \to f(x_j)$, we have that

$$\lim_{N\to\infty} h_N \sum_{j=0}^{N-1} \left(\frac{1}{h_N} \int_{x_j^N - h_N/2}^{x_j^N + h_N/2} f(x)dx\right)^2 = \int_a^b f(x)^2 dx. \qquad \square$$

Formally, to approximate this distribution with $N \in \mathbb{N}$ sample points, it is enough to take N independent random Gaussian variables W_i and consider

$$W \approx \sqrt{h_N} \sum_{j=0}^{N-1} W_j \delta_{x_j^N} \tag{1.8}$$

Remark 1: For the needed applications, we are not loosing generality by just considering Gaussian random variables. Because if we consider any i.i.d. family of random variables, the Lyapunov central limit theorem tells us that the limit of the sum of these variables converges to a Normal random variable.

Remark 2: For higher dimensions the construction is similar. A d-dimensional rectangular grid is considered, we generate independent Gaussian variables in each point of the grid, and all are multiplied by $\Pi_{j=1}^d \sqrt{h_d}$, where $h_d = (b_d - a_d)/N_d$, The length of the corresponding dimension in the domain divided by the amounts of points taken. The main property holds $\int Wf dx \sim \mathcal{N}(0, ||f||_{L^2(\mathbb{R}^d)})$.

1.2.3. Generation of an isotropic random medium. Let $C(y)$ be an even function with positive Fourier transform. Let W be a Gaussian white noise and F a filter satisfying $(2\pi)^{d/2}|\hat{F}(\xi)|^2 = \hat{C}(\xi)$, then the random medium U generated as

$$U(x) = (2\pi)^{d/2} \mathcal{F}^{-1}(\hat{F} \cdot \hat{W}) \ = F * W,$$

satisfies as covariance $C(y) = \mathbb{E}(U(x-y/2)U(x+y/2))$ and at each point behaves as $U(x) \sim \mathcal{N}(0, C(0))$.

PROOF. For simplicity assume F is 1-dimensional with finite support. Take $N \in \mathbb{N}$ and a sufficiently big grid $z_j, j \in \{0, 1, .., N-1\}$. Using the delta approximation for the Gaussian white noise, we have that

$$U(x) = F * W(x) \approx \sum_{j=0}^{N-1} \sqrt{h_N} F(x - z_j) W_j.$$

With this we compute the covariance function

$$\begin{aligned} &Cov(x-y/2, x+y/2) := \mathbb{E}\left[U(x-y/2)U(x+y/2)\right] \\ &= \lim_{N\to\infty} \mathbb{E}\left[\left(\sum_{j=0}^{N-1} \sqrt{h}_N F(x-y/2-z_j)W_j\right)\left(\sum_{k=0}^{N-1} \sqrt{h}_N F(x+y/2-z_k)W_k\right)\right]. \end{aligned}$$

Performing the cross products and afterwards taking the expectation, all terms where $j = k$ are zero as the W_j are independent, hence

$$Cov(x-y/2, x+y/2) = \lim_{N\to\infty} h_N \sum_{j=0}^{N-1} F(x-y/2-z_j)F(x+y/2-z_j).$$

Taking the limit on N, we obtain the integral

$$\begin{aligned} Cov(x-y/2, x+y/2) &= \int_{\mathbb{R}} F(x-y/2-z)F(x+y/2-z)dz \\ &= \int_{\mathbb{R}} F(z')F(y+z')dz', \end{aligned}$$

and applying the fourier transform on y, we arrive to our result

$$\begin{aligned} \hat{Cov}(\xi) &= \int_{\mathbb{R}} F(z')\mathcal{F}_y\left[F(y+z')\right](\xi)dz' \\ &= \int_{\mathbb{R}} F(z')e^{iz'\xi}\hat{F}(\xi)dz' \\ &= \sqrt{2\pi}\hat{F}(-\xi)\hat{F}(\xi) \\ &= \sqrt{2\pi}|\hat{F}(\xi)|^2. \end{aligned}$$

□

Remark: From the proof, it is clear that the available covariance functions must have a positive Fourier transform.

1.2.4. Numerical implementation. On the course web-page there is an available and well documented code to generate random media with any function handle input covariance. The implementation follows the given guidelines of this class. The Fourier transform is implemented as described in section 1.2.1, the Gaussian white noise is generated using approximation (1.8), which in Matlab consists in generating a N-dimensional independent Gaussian random variables with variance $\sqrt{h_N}$ and the covariance is inputed as a function handle.

In figure 1.3 we have two examples of random media with its respective statistics; these random media are generated in an extended domain, but for visualisation we restrict ourselves to observe the first 50 correlation lengths. Each column was generated with different correlation functions, these being respectively

$$C_1(x) = e^{-x^2/(2l^2)}\ x \in \mathbb{R}, \qquad C_2(x) = \cos(\frac{3\pi}{4l}x)(2l - |x|)\ x \in [-2l, 2l],$$

where l is the **correlation length**, which is a non strictly well defined coefficient that measures the distance at which we would see correlated values.

For **2 dimensional** random media the process is the same and there is also the possibility to generate them in the last section of the provided code. Be careful because if a desired 1-dimensional covariance function has positive Fourier transform, that does not imply that its 2-dimensional version will have it. In Figure 1.4 there are two examples of random media, corresponding to the same $C_1(|x|)$ and $C_2(|x|)$.

LISTING 1.2. Random Medium Generator

```
% 1d Random Medium Generator

% Medium parameters
    lengthMedium=1000000;
    N=2^21;
    h=lengthMedium/N;
    x=h*( (0:N-1)-N/2); % spatial grid
% Desired correlation function
    corr_length=10;
    % Gaussian correlation
%       C=@(x)exp(-x.*x/2/corr_length^2);
    % sinc function
%       C=@(x) sinc(2*pi*x/corr_length);
    % Piramid-shaped correlation
%       C=@(x) 10*heaviside(2*corr_length-abs(x)).*(1-abs(x)/2/
    corr_length);
    % Cosine
        C=@(x) cos(x*pi*3/4/corr_length).*heaviside(2*corr_length - abs(x)
            );
    % Smoothed Cosine
%       C=@(x) cos(x*pi*3/4/corr_length).*(1 - abs(x)/2/corr_length).*
    heaviside(2*corr_length - abs(x));
    % High-low Step
%       C=@(x) 1*heaviside(1.5*corr_length-abs(x)) - 0.25*heaviside(2*
    corr_length - abs(x));

% generating Gaussian white noise, the coefficient is as the integration
% multiplies by h.
    n=randn(1,N)*sqrt(1/h);

% Taking the Fourier transforms
    Fourier_n=FourierTransform(n,lengthMedium);
    Fourier_C=FourierTransform(C(x),lengthMedium);

% Computing the random medium inverting the Fourier transform
```

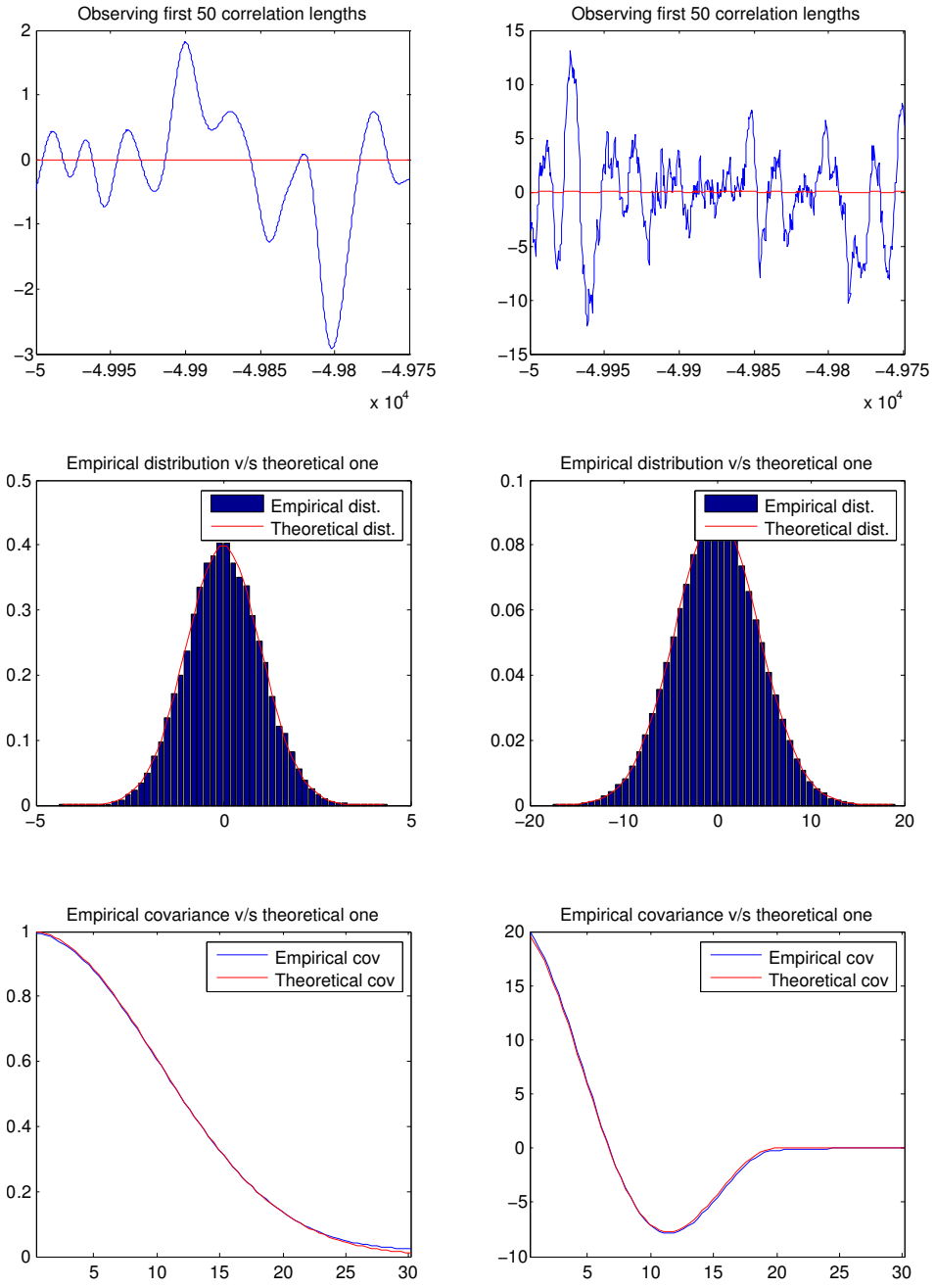

FIGURE 1.3. The left column correspond to random medium generated with a Gaussian correlation function C_1, the right hand side column correspond to a random medium generated with an attenuated and cropped cosine function C_2.

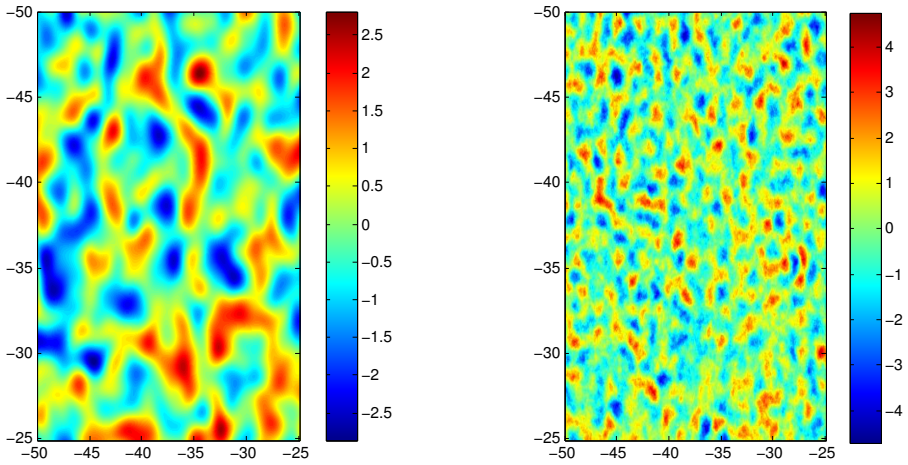

FIGURE 1.4. To the left a Gaussian 2 dimensional random medium, and to the right hand side one generated using an attenuated cosine correlation.

```
32      RandomMedium=sqrt(2*pi)*FourierTransform(sqrt(abs(Fourier_C))/sqrt(
            sqrt(2*pi)).*Fourier_n,2*pi*N/lengthMedium);
33
34  %% Observing random medium statistics
35
36  figure
37  subplot(2,2,1)
38  obsPoints=N;
39  plot(x(1:obsPoints),real(RandomMedium(1:obsPoints)))
40  hold on
41  plot(x(1:obsPoints),imag(RandomMedium(1:obsPoints)),'r')
42  hold off
43  title('Full random medium')
44
45  gca=subplot(2,2,2);
46  % To see the local shape of the random medium, equal to 50 correlation
47  % lengths
48      if lengthMedium>25*corr_length
49          aux=find(x-x(1)>25*corr_length);
50          obsPoints=aux(1);
51      else
52          obsPoints=N;
53      end
54  plot(x(1:obsPoints),real(RandomMedium(1:obsPoints)))
55  hold on
56  plot(x(1:obsPoints),imag(RandomMedium(1:obsPoints)),'r')
57  hold off
58  set(gca,'XLim',[x(1),x(obsPoints)])
59  title('Observing first 50 correlation lengths')
```

```
60
61 subplot(2,2,3)
62 % Distribution of the obtained random medium
63     [hh,hhh]=hist(real(RandomMedium),50);
64     bar(hhh,hh/sum(hh*(hhh(2)-hhh(1))))
65     hold on
66 % Expected distribution
67     sigma2=C(0);
68     disty=@(x)(exp(-x.*x/2/sigma2)/sqrt(2*pi*sigma2));
69     plot(hhh,disty(hhh),'r');
70     legend('Empirical dist.', 'Theoretical dist.');
71     title('Empirical distribution v/s theoretical one');
72
73 gca=subplot(2,2,4);
74 % Empirical covariance of the random medium
75
76     % We want to see only close to the 0 for the covariance.
77     aux=find(x-x(1)>3*corr_length);
78     obsPoints=aux(1);
79     if (obsPoints<20)
80         disp('h too small to see properly the covariance, augment N');
81     end
82     empCov=zeros(obsPoints-1,1);
83     waity=waitbar(1/obsPoints,'covariansing');
84     for i=1:obsPoints-1
85     waitbar(i/obsPoints,waity);
86     empCov(i)=sum(RandomMedium(1:end-i).*RandomMedium(1+i:end))/(length(
           RandomMedium)-i);
87     end
88     close(waity)
89     plot(x(2:obsPoints)-x(1),real(empCov))
90     hold on
91     % Plotting expected covariance
92     plot(x(2:obsPoints)-x(1), C(x(2:obsPoints)-x(1)),'r')
93     hold off
94     legend('Empirical cov','Theoretical cov');
95     title('Empirical covariance v/s theoretical one');
96     set(gca,'XLim',[x(2)-x(1),x(obsPoints)-x(1)])
97 %% 2D Random Medium.
98
99 if 1 %to activate or deactivate this section
100
101 % Medium parameters (For a square, and we treat each variable separatedly)
102     lengthMedium=100;
103     N2=2^22;
104     N=sqrt(N2);
105     h=lengthMedium/N;
106     x=h*( (0:N-1)-N/2); % spatial grid
107     [X,Y]=meshgrid(x,x);
108 % Desired correlation function
109     corr_length=1;
110     % Gaussian correlation
111 %         G=@(x)exp(-x.*x/2/corr_length^2);
```

```
112     % sinc function
113 %         G=@(x) sinc(2*pi*x/(10*corr_length));
114     % Cone-shaped correlation
115         G=@(x) 10*heaviside(2*corr_length-abs(x)).*(1-abs(x)/2/corr_length
                );
116 %     % Cosine
117 %         G=@(x) cos(x*pi*3/4/corr_length).*heaviside(2*corr_length - abs(
    x));
118     % Smoothed Cosine
119         %G=@(x) cos(x*pi*3/4/corr_length).*(1 - abs(x)/2/corr_length).*
              heaviside(2*corr_length - abs(x));
120     % High-low Step
121         %G=@(x) 1*heaviside(1.5*corr_length-abs(x)) - 0.25*heaviside(2*
              corr_length - abs(x));
122
123     C=@(x,y) G(sqrt(x.^2+y.^2));
124 % generating Gaussian white noise.
125     n=randn(N,N)*sqrt(N/lengthMedium)^2;
126
127 % Taking the Fourier transforms
128     Fourier_n=zeros(N,N);
129     for i=1:N
130         [Fourier_n(:,i),xi]=FourierTransform(n(:,i)',lengthMedium);
131     end
132     for i=1:N
133         Fourier_n(i,:)=FourierTransform(Fourier_n(i,:),lengthMedium);
134     end
135
136     Fourier_C=zeros(N,N);
137     for i=1:N
138         [Fourier_C(:,i),xi]=FourierTransform(C(X(:,i),Y(:,i))',
              lengthMedium);
139     end
140     for i=1:N
141         Fourier_C(i,:)=FourierTransform(Fourier_C(i,:),lengthMedium);
142     end
143
144 % Computing the random medium inverting the Fourier transform
145
146     RandomMedium=sqrt(abs(Fourier_C))/sqrt(2*pi).*Fourier_n;
147     for i=1:N
148         RandomMedium(:,i)=sqrt(2*pi)*FourierTransform(RandomMedium(:,i)',2*
              pi*N/lengthMedium);
149     end
150     for i=1:N
151         RandomMedium(i,:)=sqrt(2*pi)*FourierTransform(RandomMedium(i,:),2*
              pi*N/lengthMedium);
152     end
153
154  % Plotting
155 figure
156  subplot(1,3,1)
157  % total random medium
```

```
158       imagesc(x,x,real(RandomMedium))
159       title('whole random medium')
160
161
162    subplot(1,3,2)
163    % zoom to random medium
164       if lengthMedium>25*corr_length
165           aux=find(x-x(1)>25*corr_length);
166           obsPoints=aux(1);
167       else
168           obsPoints=N;
169       end
170       imagesc(x(1:obsPoints),x(1:obsPoints),real(RandomMedium(1:obsPoints,
              1:obsPoints)))
171       title('Closer look')
172
173    subplot(1,3,3)
174    % Pointwise histogram
175   % Distribution of the obtained random medium
176       [hh,hhh]=hist(real(RandomMedium),50);
177       bar(hhh,hh/sum(hh*(hhh(2)-hhh(1))))
178       hold on
179   % Expected distribution
180       sigma2=C(0,0);
181       disty=@(x)(exp(-x.*x/2/sigma2)/sqrt(2*pi*sigma2));
182       plot(hhh,disty(hhh),'r');
183       legend('Empirical dist.', 'Theoretical dist.');
184       title('Empirical distribution v/s theoretical one');
185   end
```

LISTING 1.3. Fourier transform computation

```
1  function [fhat,xi] = FourierTransform(f,a)
2  % INPUTS:
3  % f is a vector of size N=2^k, representing samples of a function over the
4  % grid x_j = a/N*(j-N/2), j=0,1,... N-1. i.e. from interval [a/2,a/2[
5  % OUTPUTS:
6  % fhat is the fourier transform of f, sampled on grid xi.
7
8  N=length(f);
9  plusminusones=mod(2:2:2*N,4)-1; %Vector [1,-1,1,-1,1,...-1]
10
11 fhat=a/N/sqrt(2*pi)*exp(-1i*pi*N/2)*plusminusones.*fft(f.*plusminusones);
12
13 xi = 2*pi/a*((0:N-1) - N/2);
```

1.3. Kramers-Kronig relations

We saw in the lecture notes (§2.4) that the real and imaginary parts of the Fourier transform f of a real causal function satisfy the Kramers-Kronig relations

$$\Re f(\omega) = \frac{2}{\pi}\,\text{p.v.}\int_0^\infty \frac{s\,\Im f(s)}{s^2-\omega^2}\,ds, \tag{1.9}$$

$$\Im f(\omega) = -\frac{2\omega}{\pi}\,\text{p.v.}\int_0^\infty \frac{\Re f(s)}{s^2-\omega^2}\,ds, \tag{1.10}$$

for $\omega \in \mathbb{R}$. In theory, these relations allow the reconstruction of the real or imaginary part of f from the knowledge of the other. However, this would require measurements at all frequencies, and in particular at arbitrarily large frequencies, which is clearly unpractical. We consider here a slightly simpler problem: reconstruct f from the knowledge of $f(\omega)$ only for certain frequencies $\omega \in D$, for some $D \subseteq \mathbb{R}^+$.

For simplicity, take $D = (0,1)$. We suppose that $\Re f$ and $\Im f$ are known in D and wish to reconstruct $\Re f$ in $\mathbb{R}^+$ (similar considerations are valid for the reconstruction of $\Im f$).

First, approximate $\Re f$ with a function $g\colon \mathbb{R}^+ \to \mathbb{R}$ defined by

$$g(\omega) = \begin{cases} \Re f(\omega) & \text{if } \omega \in (0,1], \\ p_2(\omega)e^{-\alpha(\omega-1)} & \text{if } \omega \in (1,\infty), \end{cases}$$

where p_2 is a second order polynomial chosen in such a way that $g \in C^2(\mathbb{R}^+)$ and $\alpha > 0$. The function g is known, is equal to $\Re f$ in D and decays rapidly as $\omega \to \infty$. In view of (1.10), we can compute an approximation f_i of $\Im f$ by

$$f_i(\omega) := -\frac{2\omega}{\pi}\,\text{p.v.}\int_0^\infty \frac{g(s)}{s^2-\omega^2}\,ds.$$

Since g is known, f_i can be computed.

Using (1.10) and the fact that $\Re f = g$ in D we immediately obtain

$$-\frac{2\omega}{\pi}\int_1^\infty \frac{\Re f(s) - g(s)}{s^2-\omega^2}\,ds = \Im f(\omega) - f_i(\omega), \qquad \omega \in (0,1).$$

In this identity, the right hand side is known for $\omega \in (0,1)$, and the unknown is the quantity $r(s) = \Re f(s) - g(s)$ for $s \in (1,\infty)$. Once r is reconstructed, $\Re f$ can be computed, since g is known. Thus, it remains to show how to reconstruct r from the above identity.

In other words, we have to invert the operator $r \mapsto Ar$ defined by

$$Ar(\omega) = -\frac{2\omega}{\pi}\int_1^\infty \frac{r(s)}{s^2-\omega^2}\,ds, \qquad \omega \in (0,1).$$

Let us define the proper space where to define the operator A. Let

$$H = \{r \in W^{1,2}((1,\infty)) : r(1) = 0\} \quad \text{and} \quad K = L^2((0,1)),$$

and consider the operator $A\colon H \to K$. By the invertibility of the Hilbert transform, A is injective. Moreover, the operator A is compact (see the lemma below). Therefore, it has an unbounded inverse, and so the inverse problem is ill-posed, as expected. However, it may be solved with the SVD decomposition (see Section 1.1), and a suitable regularisation may be easily performed (see §1.1.3).

It remains to show that $A\colon H \to K$ is compact.

LEMMA 1.4. *The operator $A\colon H \to K$ is compact.*

PROOF. Let $\{r_n\}_n$ be a bounded sequence in H, namely

$$\|r_n\|^2_{W^{1,2}((1,\infty))} := \|r_n\|^2_{L^2((1,\infty))} + \|r_n'\|^2_{L^2((1,\infty))} \le C \tag{1.11}$$

for some $C > 0$. This implies that there exists $r \in H$ such that $r_n \rightharpoonup r$ in $W^{1,2}$ (up to a subsequence)[2]. In particular, $r_n' \rightharpoonup r'$ in L^2. In view of the Rellich-Kondrachov theorem, the embedding $W^{1,2}((1,\infty)) \hookrightarrow L^2((1,\infty))$ is compact. Thus, $r_n \to r$ in $L^2((1,\infty))$. Without loss of generality, assume that $r = 0$.

Writing $r_n(s) = \int_1^s r_n'(t)\,dt$ we have

$$\begin{aligned} Ar_n(\omega) &= -\frac{2\omega}{\pi}\int_1^\infty \frac{r_n(s)}{s^2-\omega^2}\,ds \\ &= -\frac{2\omega}{\pi}\int_1^\infty \int_1^s \frac{r_n'(t)}{s^2-\omega^2}\,dt\,ds \\ &= -\frac{2\omega}{\pi}\int_1^\infty \int_t^\infty \frac{r_n'(t)}{s^2-\omega^2}\,ds\,dt \\ &= -\frac{1}{\pi}\int_1^\infty r_n'(t)\int_t^\infty \frac{2\omega}{s^2-\omega^2}\,ds\,dt. \end{aligned}$$

Elementary calculus yields

$$\int_t^\infty \frac{2\omega}{s^2-\omega^2}\,ds = \int_t^\infty \frac{1}{s-\omega} - \frac{1}{s+\omega}\,ds = \log\left(\frac{t+\omega}{t-\omega}\right).$$

Combining these two identities we obtain

$$Ar_n(\omega) = -\frac{1}{\pi}\int_1^\infty r_n'(t)\log\left(\frac{t+\omega}{t-\omega}\right)\,dt. \tag{1.12}$$

Therefore, by Cauchy-Schwartz inequality and (1.11) we have

$$\begin{aligned} |Ar_n(\omega)| &\le \frac{1}{\pi}\|r_n'\|_{L^2((1,\infty))}\|\log\left((t+\omega)/(t-\omega)\right)\|_{L^2((1,\infty))} \\ &\le \frac{C}{\pi}\|\log\left((t+\omega)/(t-\omega)\right)\|_{L^2((1,\infty))}. \end{aligned}$$

It can be easily proven that $\|\log\left((t+\omega)/(t-\omega)\right)\|_{L^2((1,\infty))} \le C'$ for some constant $C' > 0$ independent of ω. Therefore

$$|Ar_n(\omega)| \le CC'/\pi, \qquad \omega \in (0,1).$$

Finally, $Ar_n \to 0$ in $L^2((0,1))$ by the dominated convergence theorem, since $Ar_n \to 0$ almost everywhere (by (1.12) and the fact that $r_n' \rightharpoonup r'$ in L^2). This shows that A is compact. □

[2]The weak convergence $r_n \rightharpoonup r$ in $W^{1,2}$ means that

$$(r_n, v)_{W^{1,2}((1,\infty))} \longrightarrow (r, v)_{W^{1,2}((1,\infty))}, \qquad v \in W^{1,2}((1,\infty)),$$

where $(\cdot,\cdot)_{W^{1,2}((1,\infty))}$ denotes the scalar product associated to the norm defined in (1.11).

1.4. The Spherical means Radon transform

The spherical mean Radon transform, which integrates a function over all spheres centered at points of a given set, is useful in multi-wave tomography. For instance, in photo-acoustic imaging under some simplifications, the spherical mean data of an unknown function (the absorbed optical energy density) is measured by acoustic transducers, and the imaging problem is to invert that transform.

Let Ω be a bounded open set of $\mathbb{R}^d$. The spherical mean Radon transform $\mathcal{R} : \mathcal{C}^0(\mathbb{R}^d) \to \mathcal{C}^0(\partial\Omega \times \mathbb{R}^+)$ with centers on $\partial\Omega$ is given for $f \in \mathcal{C}^0(\mathbb{R}^d)$ by

$$\mathcal{R}[f](x,s) = \frac{1}{\omega_d} \int_S f(x + s\xi) d\sigma(\xi), \quad (x,s) \in \partial\Omega \times \mathbb{R}^d,$$

where S denotes the unit sphere in $\mathbb{R}^d$ and ω_d its surface measure.

1.4.1. The Wave equation. To motivate the interest in studying the spherical means Radon transform, we look at the wave equation. Let $f, g \in \mathcal{C}^0(\mathbb{R}^n)$ be functions with compact support, we are interested in solving the following initial value problem

$$\begin{cases} \frac{\partial^2}{\partial t^2} p(x,t) - \Delta_x p(x,t) &= 0, & \mathbb{R}^d \times \mathbb{R}^+, \\ p(x,0) &= f(x), & \mathbb{R}^d, \\ \frac{\partial}{\partial t} p(x,0) &= g(x), & \mathbb{R}^d. \end{cases}$$

To do it so, we take the Fourier transform in space. Lets define $\hat{p}(\xi,t) = \mathcal{F}_x[p(\cdot,t)](\xi)$ and then, by the Fourier transform property with respect to the derivatives, we obtain a family of ODE's parametrized by $t \in \mathbb{R}^+$

$$\partial_{tt}\hat{p}(\xi,t) + |\xi|^2 \hat{p}(\xi,t) = 0, \;\; \hat{p}(\xi,0) = \hat{f}(\xi), \;\; \partial_t \hat{p}(\xi,0) = \hat{g}(\xi), \;\; \forall \xi \in \mathbb{R}^d, t \in \mathbb{R}^t,$$

whose solution is given by

$$\hat{p}(\xi,t) = \hat{f}(\xi)\cos(|\xi|t) + \hat{g}(\xi)\frac{\sin(|\xi|t)}{|\xi|}.$$

So taking the inverse of the Fourier transform and using the convolution formula, we arrive to

$$p(x,t) = (2\pi)^{d/2} f * \partial_t U_t(x) + (2\pi)^{d/2} g * U_t(x), \qquad \forall x \in \mathbb{R}^d, t \in \mathbb{R}^+,$$

where

$$U_t(x) = \mathcal{F}_x^{-1}\left[\frac{\sin(|\cdot|t)}{|\cdot|}\right](x,t),$$

is the fundamental solution. The explicit form of this fundamental solution for $d = 2, 3$ is given by:

$$U_t(x) = \begin{cases} \frac{1}{2\pi(t^2-|x|^2)^{1/2}} \mathbb{1}_{|x|<t}(x,t), & d = 2, \\ \delta(t-|x|)/4\pi|x|, & d = 3. \end{cases}$$

Lets consider $f = 0$, then the value of the solution $p(x,t)$ on some surface $\partial\Omega$ enclosing g will be

$$p(x,t) = \begin{cases} \int_0^t \frac{s\mathcal{R}[g](x,s)}{\sqrt{t^2-s^2}} ds, & d = 2, \\ t\mathcal{R}[g](x,t), & d = 3. \end{cases}$$

Thus if we are interested in recovering the initial speed from the external measurements, we need to be able to invert the spherical means Radon transform.

1.4.2. Backprojection. Consider now Ω is the sphere on dimension d ($\partial\Omega = S$), and the spherical means Radon transform defined on the Schwartz space, i.e. $\mathcal{R} : \mathcal{S}(\mathbb{R}^d) \to \mathcal{S}(S \times \mathbb{R}^+)$. We define the **Backprojection operator** $\mathcal{R}^* : \mathcal{S}(S \times \mathbb{R}^+) \to \mathcal{S}(\mathbb{R}^d)$ as

$$\mathcal{R}^*[g] = \frac{1}{\omega_d} \int_S \frac{g(y, |x-y|)}{|x-y|^{d-1}} d\sigma(y).$$

If we consider the L^2 internal product in both Schwartz spaces, the backprojection operator is the adjoint of the spherical means operator.

PROOF. Consider $f \in \mathcal{S}(\mathbb{R}^d), g \in \mathcal{S}(S \times \mathbb{R}^+)$, then

$$\begin{aligned}
\langle f, \mathcal{R}^*[g] \rangle_{L^2(\mathbb{R}^d)} &= \int_{\mathbb{R}^d} f(x) \frac{1}{\omega_d} \int_S \frac{g(y, |x-y|)}{|x-y|^{d-1}} d\sigma(y) dx, \\
&= \int_S \int_{\mathbb{R}^d} \frac{1}{\omega_d} f(z+y) \frac{g(y, |z|)}{|z|^{d-1}} dz d\sigma(y), \\
&= \int_S \int_{\mathbb{R}^+} \int_S \frac{1}{\omega_d} f(y+tw) g(y,t) d\sigma(w) dt d\sigma(y), \\
&= \int_S \int_{\mathbb{R}^+} \mathcal{R}[f](y,t) g(y,t) dt d\sigma(y), \\
&= \langle \mathcal{R}[f], g \rangle_{L^2(S \times \mathbb{R}^+)}.
\end{aligned}$$

□

Remark: This adjoint operator allows us to extend the domain of definition of the Spherical means Radon transform to the Tempered Distribution space S', as

$$\langle \mathcal{R}(T), f \rangle = \langle T, \mathcal{R}^*(f) \rangle.$$

This adjoint operator $\mathcal{R}^*$ is called backprojection because it defines a preliminary, and naive way of attempting to invert the spherical means Radon transform. Namely the backprojection algorithm

$$f(x) \approx \mathcal{R}^*\mathcal{R}[f](x) = \frac{1}{\omega_d} \int_S \frac{1}{\omega_d} \int_S \frac{f(y + |x-y|w)}{|x-y|^{d-1}} d\sigma(w) d\sigma(y).$$

Intuitively, this algorithm at each point $x \in \Omega$ gives as value the average of all the available spherical integrals of f that go trough that point. Since the reconstruction is based on averages of integrals, it assigns positive value to all points in space (if $f \geq 0$) and the obtained reconstructions are heavily smoothed.

1.4.3. Filtered Backprojection. There are explicit inversion formulae for the Spherical means Radon transform. For the particular case of $\partial\Omega = S$ and f with compact support compactly contained in Ω, for $d = 2, 3$ these formulae are

$$f(x) = \begin{cases} \frac{1}{2\pi} \nabla \cdot \int_S y \frac{\frac{\partial}{\partial s}(s\mathcal{R}[f])(y, |x-y|)}{|x-y|} d\sigma(y), & d = 2, \\ \frac{1}{2\pi} \int_S \int_0^2 \left[\frac{\partial}{\partial s} s \frac{\partial}{\partial s} \mathcal{R}[f] \right](y,s) \log|s^2 - |y-x|^2| ds d\sigma(y), & d = 3. \end{cases}$$

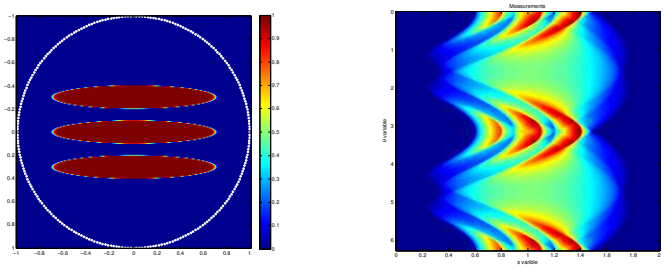

FIGURE 1.5. In the left, the function we seek to reconstruct and the available points on the sphere where the Spherical Radon transform will be sampled. In the right hand side, we have the obtained measurements. The right hand side image is the Spherical Radon transform, with $s \in [0,2]$ and $\theta \in [0,2\pi)$.

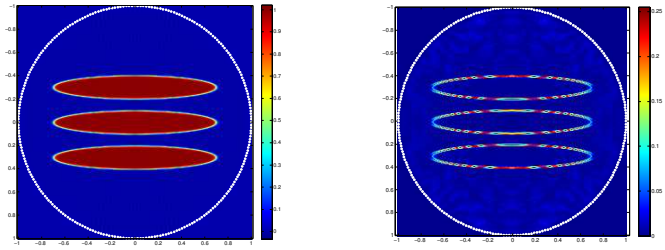

FIGURE 1.6. In the left, the reconstructed function and, in the right hand side, the relative error map. As it can be observed, the error is concentrated on the high frequency zones of the objective function.

These formulae belong to a type of inversion formulae called Filtered Backprojection, that are of the form

$$f(x) = \mathcal{R}^* \mathcal{B} \mathcal{R} f,$$

where $\mathcal{B}$ is considered to be a filter of data $\mathcal{R}[f]$, hence the name of it. For instance, in the case $d = 2$, the filter is

$$\mathcal{B}[g](x,t) = \int_0^2 \frac{\partial^2 g}{ds^2}(x,s) \log(|s^2 - t^2|) ds.$$

1.4.4. Numerical examples. There are codes in the webpage of the course that simulate the 2-dimensional spherical means Radon transform measurements for $\partial\Omega = S$ and afterwards inverts it using the filtered backprojection. The parameters of the codes are the resolution of the function f, its shape and the amount of samples of $\mathcal{R}[f](s_i, \theta_j)$, where $s_i \in (0,2)$ are uniformly sampled, and θ_j can be considered non-uniform on S. In figures 1.5, 1.6 and 1.7 there are two examples.

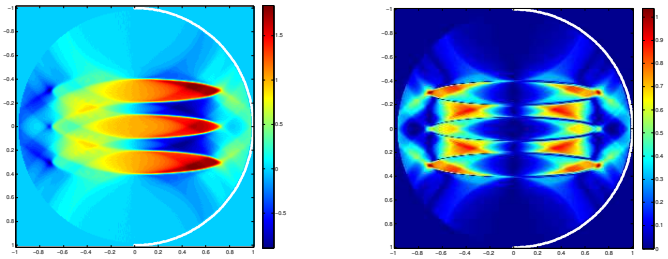

FIGURE 1.7. Reconstruction of the same object, but with the samples on the θ variables concentrated on the right hand side of the image. To the right hand side there is the relative error map. As it can be seen, the reconstruction strongly deteriorates.

1.5. Neumann-Poincaré operator

Introduce the operator $\mathcal{K}_D : L^2(\partial D) \to L^2(\partial D)$ given by

$$\mathcal{K}_D[\varphi](x) = \frac{1}{\omega_d} \int_{\partial D} \frac{(y-x)\cdot \nu_y}{|x-y|^d} \varphi(y)\, d\sigma(y) \ . \tag{1.13}$$

The operator defined by

$$\mathcal{K}_D^*[\varphi](x) = \frac{1}{\omega_d} \int_{\partial D} \frac{(x-y)\cdot \nu_x}{|x-y|^d} \varphi(y)\, d\sigma(y) \ , \tag{1.14}$$

is the L^2-adjoint of $\mathcal{K}_D$. Furthermore, if D is a bounded $\mathcal{C}^2$-domain, then the operators $\mathcal{K}_D$ and $\mathcal{K}_D^*$ are compact operators in $L^2(\partial D)$.

Suppose that D is a two dimensional disk with radius r_0. Then,

$$\frac{(x-y)\cdot \nu_x}{|x-y|^2} = \frac{1}{2r_0} \quad \forall\ x, y \in \partial D, x \neq y \ ,$$

and therefore, for any $\varphi \in L^2(\partial D)$,

$$\mathcal{K}_D^*[\varphi](x) = \mathcal{K}_D[\varphi](x) = \frac{1}{4\pi r_0} \int_{\partial D} \varphi(y)\, d\sigma(y) \ , \tag{1.15}$$

for all $x \in \partial D$.

For $d \geq 3$, if D is a ball with radius r_0, then, we have

$$\frac{(x-y)\cdot \nu_x}{|x-y|^d} = \frac{1}{2r_0} \frac{1}{|x-y|^{d-2}} \quad \forall\ x, y \in \partial D, x \neq y \ ,$$

and for any $\varphi \in L^2(\partial D)$ and $x \in \partial D$,

$$\mathcal{K}^*[\varphi](x) = \mathcal{K}_D[\varphi](x) = \frac{(2-d)}{2r_0} \mathcal{S}_D[\varphi](x) \ , \tag{1.16}$$

where $\mathcal{S}_D$ is the single layer potential.

If D is an ellipse whose semi-axes are on the x_1- and x_2-axes and of length a and b, then, by using the parametric representation $X(t) = (a\cos t, b \sin t), 0 \leq t \leq 2\pi$, for the boundary ∂D, we have

$$\mathcal{K}_D[\varphi](x) = \frac{ab}{2\pi(a^2+b^2)} \int_0^{2\pi} \frac{\varphi(X(t))}{1 - Q\cos(t+\theta)}\, dt \ , \tag{1.17}$$

where $x = X(\theta)$ and $Q = (a^2 - b^2)/(a^2 + b^2)$.

1.5.1. Symmetrization of the Neumann-Poincaré operator. The following Calderón's identity holds:

$$\mathcal{S}_D \mathcal{K}_D^* = \mathcal{K}_D \mathcal{S}_D \quad \text{on } W^2_{-1/2}(\partial D)\,. \tag{1.18}$$

Consider the three-dimensional case. Since the single layer potential becomes a unitary operator from $W^2_{-1/2}(\partial D)$ onto $W^2_{1/2}(\partial D)$, the operator $\mathcal{K}_D^*$ can be symmetrized using Calderón identity (1.18) and hence becomes self-adjoint. It is then possible to write its spectral decomposition. Let $\mathcal{H}^*(\partial D)$ be the space $W^2_{-1/2}(\partial D)$ with the inner product

$$(u, v)_{\mathcal{H}^*} = -(u, \mathcal{S}_D[v])_{-\frac{1}{2},\frac{1}{2}}\,, \tag{1.19}$$

where $(\cdot,\cdot)_{-\frac{1}{2},\frac{1}{2}}$ is the duality pairing between $W^2_{-1/2}(\partial D)$ and $W^2_{1/2}(\partial D)$, which is equivalent to the original one (on $W^2_{-1/2}(\partial D)$). The following results hold:

(i) The operator $\mathcal{K}_D^*$ is self-adjoint in the Hilbert space $\mathcal{H}^*(\partial D)$;

(ii) Let (λ_j, φ_j), $j = 0, 1, 2, \ldots$ be the eigenvalue and normalized eigenfunction pair of $\mathcal{K}_D^*$ in $\mathcal{H}^*(\partial D)$, then $\lambda_0 = 1/2$, $\lambda_j \in]-\frac{1}{2}, \frac{1}{2}[$ for $j \geq 1$, and $\lambda_j \to 0$ as $j \to \infty$;

(iii) The following spectral representation formula holds: for any $\psi \in W^2_{-1/2}(\partial D)$,

$$\mathcal{K}_D^*[\psi] = \sum_{j=0}^{\infty} \lambda_j (\psi, \varphi_j)_{\mathcal{H}^*} \otimes \varphi_j\,.$$

In two dimensions, even though the single-layer potential $\mathcal{S}_D : W^2_{-1/2}(\partial D) \to W^2_{1/2}(\partial D)$ is not, in general, invertible nor injective, i.e., $-(u, \mathcal{S}_D[v])_{-\frac{1}{2},\frac{1}{2}}$ does not define an inner product, a symmetrization technique similar to the three-dimensional case can be applied.

Note that using (1.15), it follows that if D is a disk, then the spectrum of $\mathcal{K}_D^*$ is $1/2$. Furthermore, by using (1.16) it can be shown that the spectrum of $\mathcal{K}_D^*$ in the case where D is a ball is $1/(2(2j+1))$, $j = 0, 1, \ldots$. If D is an ellipse of semi-axes a and b, then $0, 1/2$ and $\pm(1/2)((a-b)/(a+b))^j$, $j = 1, 2, \ldots$ are the eigenvalues of $\mathcal{K}_D^*$, which can be expressed by (1.17).

1.5.1.1. *Code.* In the course's web-page there is a Matlab code that computes the $\mathcal{K}$ operator and its adjoint. The code relies on a data structure that represents the 2 dimensional curve ∂D, on this curve we approximate a basis for $L^2(\partial D)$ by defining points on ∂D and taking the family of functions that value 1 in only one point and 0 in the others. Over this discrete family we compute the $\mathcal{K}$ that is represented as a Matrix.

For the case of an ellipse of semi-axes $a = 3, b = 2$, using the code we can generate a sufficiently big matrix for $\mathcal{K}$ such that we can estimate the first eigenvalues, being these

```
> 0.500
> 0.100
> 0.100
> 0.020
> 0.020
> 0.004
```

```
> 0.004
...
```

which coincides with the ones given by the theory.

1.5.2. Polarization tensor. The polarization tensor is defined by

$$M(\lambda, D) = \int_{\partial D} y(\lambda I - \mathcal{K}^*)^{-1}[\nu](y)\, d\sigma(y),$$

where ν is the outward normal to ∂D. It plays a key role in imaging.

There are also available codes to compute the polarization tensor of any curve. For the case of an ellipse whose axes are aligned with the coordinate axes, we know its polarization tensor is given by the 2x2 matrix

$$M(\lambda, B) = (k-1)|B| \begin{pmatrix} \frac{a+b}{a+kb} & 0 \\ 0 & \frac{a+b}{b+ka} \end{pmatrix}, \quad \text{where } k = \frac{2\lambda+1}{2\lambda-1}.$$

These values coincides to the one computed with Matlab:

```
> 20.9440        0
> 0              17.1360
```

The polarization tensor of multiple domains (say $D_1 \cup D_2$) can be defined by by

$$M(\lambda, D_1 \cup D_2) = \int_{\partial D_1} y\varphi_1(y)\, d\sigma(y) + \int_{\partial D_2} y\varphi_2(y)\, d\sigma(y),$$

where (φ_1, φ_2) is solution to

$$\begin{pmatrix} \lambda I - \mathcal{K}_{D_1}^* & -\frac{\partial \mathcal{S}_{D_2}}{\partial \nu^{(1)}}\big|_{\partial D_1} \\ -\frac{\partial \mathcal{S}_{D_1}}{\partial \nu^{(2)}}\big|_{\partial D_2} & \lambda I - \mathcal{K}_{D_2}^* \end{pmatrix} \begin{pmatrix} \varphi_1 \\ \varphi_2 \end{pmatrix} = \begin{pmatrix} \nu^{(1)} \\ \nu^{(2)} \end{pmatrix},$$

where $\nu^{(1)}$ and $\nu^{(2)}$ are the outward normal to ∂D_1 and ∂D_2, respectively.

As example, for the case of two discs of radius 0.5 and 0.3, located at $(0.5, 0.5)$ and $(-0.8, -0.5)$ respectively, the computed polarization tensor is

```
> 0.7264       -0.1689
> 0.0660        1.1023
```

CHAPTER 2

Anomaly Imaging Algorithms

In this tutorial we will apply the accurate asymptotic formulas derived in the course for the purpose of identifying the location and certain properties of the inclusions. We consider conductivity and electromagnetic imaging, and single out simple fundamental algorithms which are tested and uploaded in the course's web-page.

We will construct various reconstruction algorithms that take advantage of the smallness of the inclusions. In particular, Multiple Signal Classification algorithm (MUSIC), backpropagation and Kirchhoff migration.

All written codes are uploaded in the course's web-page. The computations make use of Matlab's PDE toolbox, as it is required to implement the direct solution for each reconstruction method. The implementation and use of the PDE toolbox will not be detailed as it is not in the scope of the course.

2.1. The Ill-posedness of Electrical Impedance Tomography

Before considering more sophisticated inversion schemes based on anomaly detection, let us see that the direct approach for the reconstruction in Electrical Impedance Tomography (EIT) leads to a severely ill-posed problem. This motivates the use of more advanced algorithms.

We refer to the lecture notes, where EIT is discussed and a model derived (§6). Here, we shall use a linearized approximation. The inversion boils down to solving a linear system of equations

$$MA = X$$

where M is the sensitivity matrix (known), A is the unknown image (written as a column vector) and X is the vector of boundary measurements.

As discussed in §1.1.2, the ill-posedness of this inverse problem may be characterized by the decay of the singular values of M. The singular values of M, when considering a homogenous background in the unit ball in two-dimensions are shown in Figure 2.1. As it can be clearly seen, the exponential decay of the singular values indicates that this inverse problem is severely ill-posed, and so suitable regularization techniques have to be implemented.

2.2. Direct Imaging for the Conductivity Problem

We will apply the conductivity problem asymptotic formula

$$u(x) \quad = \quad U(x) - \delta^d \nabla U(z) \cdot M(\lambda, B) \nabla_z N(x,z) + O(\delta^{d+1}) \,, \tag{2.1}$$

for the purpose of identifying the location and certain properties of the conductivity inclusions. Two simple fundamental algorithms that take advantage of the

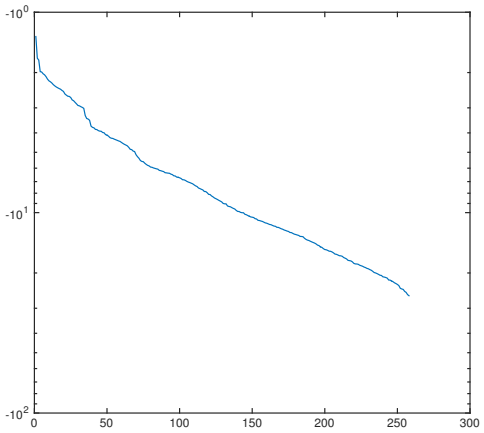

FIGURE 2.1. The decay of the singular values of the sensitivity matrix M in a semi-logarithmic scale.

smallness of the inclusions are singled out: projection-type algorithms and MUSIC-type algorithms. These algorithms are fast, stable, and efficient.

2.2.1. Detection of a Single Inclusion: A Projection-Type Algorithm. The projection-type location search algorithm makes use of constant current sources. Let Ω be the background medium and let U be the background solution. One wants to apply a special type of current that makes ∇U constant in the inclusion D. The injection current $g = a \cdot \nu$ for a fixed unit vector $a \in \mathbb{R}^d$ yields $\nabla U = a$ in Ω.

Let the conductivity inclusion D be of the form $z + \delta B$. Let w be a smooth harmonic function in Ω. From (2.1) it follows that the weighted boundary measurements $I_w[U]$ satisfies

$$I_w[U] := \int_{\partial\Omega} (u - U)(x) \frac{\partial w}{\partial \nu}(x)\, d\sigma(x) \approx -\delta^d \nabla U(z) \cdot M(\lambda, B) \nabla w(z)\,, \tag{2.2}$$

where $\lambda = (k+1)/(2(k-1))$, k being the conductivity of D.

Assume for the sake of simplicity that $d = 2$ and D is a disk. Set

$$w(x) = -(1/2\pi) \log|x - y| \quad \text{for } y \in \mathbb{R}^2 \setminus \overline{\Omega}, x \in \Omega\,.$$

Since w is harmonic in Ω, using the course's derived formula for the polarization tensor of ellipses and equation (2.2), it follows that

$$I_w[U] \approx \frac{(k-1)|D|}{\pi(k+1)} \frac{(y - z) \cdot a}{|y - z|^2}\,, \quad y \in \mathbb{R}^2 \setminus \overline{\Omega}\,. \tag{2.3}$$

The first step for the reconstruction procedure is to locate the inclusion. The location search algorithm is as follows. Take two observation lines Σ_1 and Σ_2 contained in $\mathbb{R}^2 \setminus \overline{\Omega}$ given by

$$\Sigma_1 := \text{ a line parallel to } a\,,$$
$$\Sigma_2 := \text{ a line normal to } a\,.$$

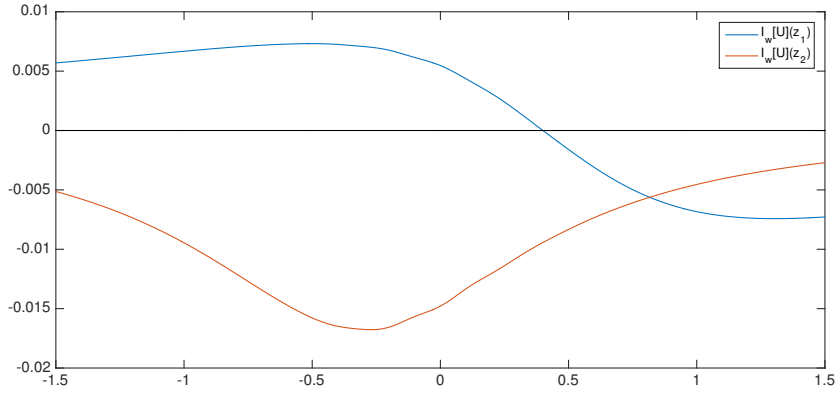

FIGURE 2.2. The plots of the functions $I_w[U](z_i)$ for $z_i \in \Sigma_i$, $i = 1, 2$.

Find two points $z_i^S \in \Sigma_i, i = 1, 2$, so that

$$I_w[U](z_1^S) = 0, \quad I_w[U](z_2^S) = \max_{y \in \Sigma_2} |I_w[U](y)| .$$

From (2.3), one can see that the intersecting point z^S of the two lines

$$\Pi_1(z_1^S) := \{y \mid a \cdot (y - z_1^S) = 0\} , \tag{2.4}$$

$$\Pi_2(z_2^S) := \{y \mid (y - z_2^S) \text{ is parallel to } a\} \tag{2.5}$$

is close to the center z of the inclusion D: $|z^S - z| = O(\delta^2)$.

Once one locates the inclusion, the factor $|D|(k-1)/(k+1)$ can be estimated. As it has been said before, this information is a mixture of the conductivity and the volume. A small inclusion with high conductivity and larger inclusion with lower conductivity can have the same polarization tensor.

EXAMPLE 2.1. As an example, we consider the two dimensional unit ball $\Omega = B(0, 1)$ with a homogeneous background and an inclusion $D = z + \delta B$, with $B = B(0, 1)$, $z = (0.4, -0.3)$ and $\delta = .2$. The contrast is given by $k = 2$. We choose $a = e_1$. The plots of the functions $I_w[U](z_i)$ for $z_i \in \Sigma_i$, $i = 1, 2$, are shown in Figure 2.2. The approximated center of the inclusion may be calculated as above, by looking at the zero of $I_w[U](z_1)$ and at the maximum of $|I_w[U](z_2)|$. In this case, we get $(z_1^S, z_2^S) = (0.4, -0.27)$, which is a very good approximation of the exact center z.

2.2.2. Detection of Multiple Inclusions: A MUSIC-Type Algorithm. Consider P well-separated inclusions $D_p = \delta B_p + z_p$ (these are a fixed distance apart), with conductivities k_p, $p = 1, \ldots, P$. Suppose for the sake of simplicity that all the domains B_p are disks. Let $y_l \in \mathbb{R}^2 \setminus \Omega$ for $l = 1, \ldots, n$ denote the source points. Set

$$U_{y_l} = w_{y_l} := -(1/2\pi) \log |x - y_l| \quad \text{for } x \in \Omega, \quad l = 1, \ldots, n .$$

The MUSIC-type location search algorithm for detecting multiple inclusions is as follows. For $n \in \mathbb{N}$ sufficiently large, define the response matrix $A = (A_{ll'})_{l,l'=1}^n$

by

$$A_{ll'} = I_{w_{y_l}}[U_{y_{l'}}] := \int_{\partial\Omega} (u - U_{y_{l'}})(x) \frac{\partial w_{y_l}}{\partial \nu}(x)\, d\sigma(x) \ .$$

Expansion (2.2) yields

$$A_{ll'} \approx -\sum_{p=1}^{P} \frac{2(k_p - 1)|D_p|}{k_p + 1} \nabla U_{y_{l'}}(z_p) \cdot \nabla U_{y_l}(z_p) \ .$$

For $j = 1, 2$, introduce

$$g^{(j)}(z^S) = \left(e_j \cdot \nabla U_{y_1}(z^S), \ldots, e_j \cdot \nabla U_{y_n}(z^S) \right)^T, \quad z^S \in \Omega \ ,$$

where $\{e_1, e_2\}$ is an orthonormal basis of $\mathbb{R}^2$.

LEMMA 2.2 (MUSIC characterization). *There exists $n_0 > dP$ such that for any $n > n_0$ the following characterization of the location of the inclusions in terms of the range of the matrix A holds:*

$$g^{(j)}(z^S) \in \text{Range}(A) \text{ for } j = 1, 2 \text{ iff } z^S \in \{z_1, \ldots, z_P\} \ . \tag{2.6}$$

The MUSIC-type algorithm to determine the locations of the inclusions is as follows. Let $\Pi_{\text{noise}} = I - \Pi$, where Π is the orthogonal projection onto the range of A. Given any point $z^S \in \Omega$, form the vector $g^{(j)}(z^S)$. The MUSIC characterization (2.6) says that the point z^S coincides with the location of an inclusion if and only if $\Pi_{\text{noise}}[g^{(j)}](z^S) = 0$, $j = 1, 2$. Thus one can form an image of the inclusions by plotting, at each point z^S, the cost function

$$\mathcal{I}_{\text{MU}}(z^S) = \frac{1}{\sqrt{||\Pi_{\text{noise}}[g^{(1)}](z^S)||^2 + ||\Pi_{\text{noise}}[g^{(2)}](z^S)||^2}} \ .$$

The resulting plot will have large peaks at the locations of the inclusions.

EXAMPLE 2.3. We now consider two circular inclusions in the two-dimensional unit ball $\Omega = B(0, 1)$, as shown in Figure 2.3a. We apply the above method and compute the imaging functional $\mathcal{I}_{\text{MU}}$. A delicate issue is the estimate of the range of A. This is done via the SVD decomposition of A, by keeping only the first L right singular vectors. The results are shown in Figures 2.3b, 2.3c and 2.3d for $L = 3$, $L = 4$ and $L = 20$, respectively. Since there are two inclusions and we are in two dimensions, the range of A should be well-approximated by $L = 4$ vectors. The images show what happens if the dimension of the range is not correctly estimated. Note that these images only indicate the locations of the inclusions, and not their contrast.

2.3. Direct Imaging Algorithms for the Helmholtz Equation

In this section, we design direct imaging functionals for small inclusions at a fixed frequency k_0. Consider the Helmholtz equation with the Neumann data g in the presence of the inclusion D and let U denote the background solution.

Let w be a smooth function such that $(\Delta + k_0^2)w = 0$ in Ω. The weighted boundary measurements $I_w[U]$ defined by

$$I_w[U] := \int_{\partial\Omega} (u - U)(x) \frac{\partial w}{\partial \nu}(x)\, d\sigma(x) \tag{2.7}$$

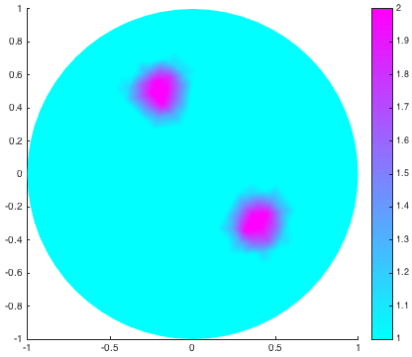

(A) The exact locations and contrasts of the inclusions.

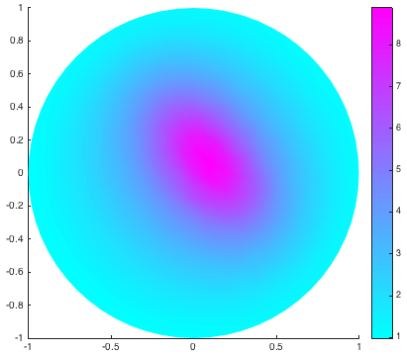

(B) The imaging functional $\mathcal{I}_{\text{MU}}$ with $L = 3$.

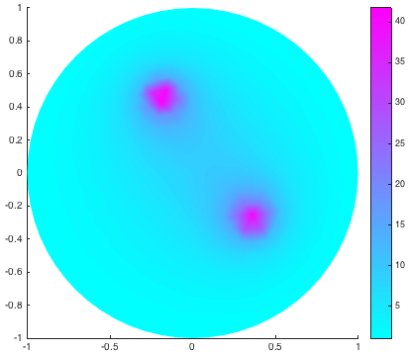

(C) The imaging functional $\mathcal{I}_{\text{MU}}$ with $L = 4$.

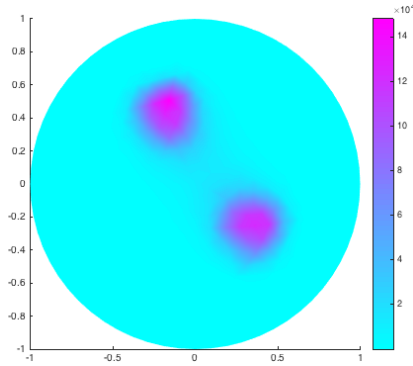

(D) The imaging functional $\mathcal{I}_{\text{MU}}$ with $L = 20$.

FIGURE 2.3. The imaging functional $\mathcal{I}_{\text{MU}}$ for conductivity imaging.

satisfies

$$
\begin{aligned}
I_w[U,\omega] &= -\delta^d\Big(\nabla U(z)\cdot M(\lambda,D)\nabla w(z) + k_0^2(\tfrac{\varepsilon_*}{\varepsilon_0}-1)|D|U(z)w(z)\Big) \\
&+ o(\delta^d)\,,
\end{aligned}
\tag{2.8}
$$

with λ given by $\frac{\mu_0+\mu_*}{2(\mu_0-\mu_*)}$.

We apply the course's derived asymptotic formulas for the Helmholtz equation and (2.8) for the purpose of identifying the location and certain properties of the inclusions.

Consider P well-separated inclusions $D_p = z_p + \delta B_p$, $p = 1,\dots,P$. The magnetic permeability and electric permittivity of D_p are denoted by μ_p and ε_p, respectively. Suppose that all the domains B_p are disks. In this case, we have

$$
I_w[U] \approx -\sum_{p=1}^{P} |D_p|\left(2\frac{\mu_p-\mu_0}{\mu_0+\mu_p}\nabla U(z)\cdot\nabla w(z) + k_0^2(\frac{\varepsilon_p}{\varepsilon_0}-1)U(z)w(z)\right)\,.
\tag{2.9}
$$

2.3.1. MUSIC-type Algorithm. Let $(\theta_1, \ldots, \theta_n)$ be n unit vectors in $\mathbb{R}^d$. For $\theta \in \{\theta_1, \ldots, \theta_n\}$, we assume that we are in possession of the boundary data u when the domain Ω is illuminated with the plane wave $U(x) = e^{ik_0\theta\cdot x}$. Taking the harmonic function $w(x) = e^{-ik_0\theta'\cdot x}$ for $\theta' \in \{\theta_1, \ldots, \theta_n\}$ and using (2.9) shows that the weighted boundary measurement is approximately equal to

$$I_w[U] \approx -\sum_{p=1}^{P} |D_p| k_0^2 \Big(2\frac{\mu_0 - \mu_p}{\mu_0 + \mu_p}\theta\cdot\theta' + \frac{\varepsilon_p}{\varepsilon_0} - 1\Big) e^{ik_0(\theta-\theta')\cdot z_p} .$$

Define the response matrix $A = (A_{ll'})_{l,l'=1}^n \in \mathbb{C}^{n\times n}$ by

$$A_{ll'} := I_{w_{l'}}[U_l, \omega] , \tag{2.10}$$

where $U_l(x) = e^{ik_0\theta_l\cdot x}, w_l(x) = e^{-ik_0\theta_l\cdot x}, l = 1, \ldots, n$. It is approximately given by

$$A_{ll'} \approx -\sum_{p=1}^{P} |D_p| k_0^2 \Big(2\frac{\mu_0 - \mu_p}{\mu_0 + \mu_p}\theta_l\cdot\theta_{l'} + \frac{\varepsilon_p}{\varepsilon_0} - 1\Big) e^{ik_0(\theta_l-\theta_{l'})\cdot z_p} , \tag{2.11}$$

for $l, l' = 1, \ldots, n$. Introduce the n-dimensional vector fields $g^{(j)}(z^S)$, for $z^S \in \Omega$ and $j = 1, \ldots, d+1$, by

$$g^{(j)}(z^S) = \frac{1}{\sqrt{n}}\big(e_j\cdot\theta_1 e^{ik_0\theta_1\cdot z^S}, \ldots, e_j\cdot\theta_n e^{ik_0\theta_n\cdot z^S}\big)^T, \quad j = 1, \ldots, d , \tag{2.12}$$

and

$$g^{(d+1)}(z^S) = \frac{1}{\sqrt{n}}\ \big(e^{ik_0\theta_1\cdot z^S}, \ldots, e^{ik_0\theta_n\cdot z^S}\big)^T , \tag{2.13}$$

where $\{e_1, \ldots, e_d\}$ is an orthonormal basis of $\mathbb{R}^d$. Let $g(z^S)$ be the $n \times d$ matrix whose columns are $g^{(1)}(z^S), \ldots, g^{(d)}(z^S)$. Then (2.11) can be written as

$$A \approx -n\sum_{p=1}^{P} |D_p| k_0^2 \Big(2\frac{\mu_0 - \mu_p}{\mu_0 + \mu_p} g(z_p)\overline{g(z_p)}^T + (\frac{\varepsilon_p}{\varepsilon_0} - 1) g^{(d+1)}(z_p)\overline{g^{(d+1)}(z_p)}^T\Big) . \tag{2.14}$$

Let $\Pi_{\text{noise}} = I - \Pi$, where Π is the orthogonal projection onto the range of A as before. The MUSIC-type imaging functional is defined by

$$\mathcal{I}_{\text{MU}}(z^S) := \Big(\sum_{j=1}^{d+1} \|\Pi_{\text{noise}}[g^{(j)}](z^S)\|^2\Big)^{-1/2}. \tag{2.15}$$

This functional has large peaks only at the locations of the inclusions.

2.3.2. Backpropagation-type Algorithms. Let $(\theta_1, \ldots, \theta_n)$ be n unit vectors in $\mathbb{R}^d$. Consider measurements with $U_l(x) = w_l(x) = e^{ik_0\theta_l\cdot x}$, $l = 1, \ldots, n$. The response now will be approximately given by

$$A_{ll'} \approx -\sum_{p=1}^{P} |D_p| k_0^2 \Big(2\frac{\mu_p - \mu_0}{\mu_0 + \mu_p}\theta_l\cdot\theta_{l'} + \frac{\varepsilon_p}{\varepsilon_0} - 1\Big) e^{ik_0(\theta_l+\theta_{l'})\cdot z_p} ,$$

and thus its diagonal will be

$$A_{ll} \approx -\sum_{p=1}^{P} |D_p| k_0^2 \Big(2\frac{\mu_p - \mu_0}{\mu_0 + \mu_p} + \frac{\varepsilon_p}{\varepsilon_0} - 1\Big) e^{i2k_0\theta_l\cdot z_p} ,$$

The backpropagation-type imaging algorithm makes use of this particular shape to extract the location of the inclusion, which is contained only in the exponential term. To do it so we consider the following backpropagation-type imaging functional at single frequency k_0

$$\mathcal{I}_{\mathrm{BP}}(z^S) := \frac{1}{n}\sum_{l=1}^{n} e^{-2ik_0\theta_l\cdot z^S} I_{w_l}[U_l]\ , \tag{2.16}$$

For sufficiently large n and equidistant θ_l, we have

$$\frac{1}{n}\sum_{l=1}^{n} e^{ik_0\theta_l\cdot x} \approx 4(\frac{\pi}{k_0})^{d-2}\,\Im m\left\{\Gamma_{k_0}(x,0)\right\} = \begin{cases} \mathrm{sinc}(k_0|x|) & \text{for } d=3\ , \\ J_0(k_0|x|) & \text{for } d=2\ , \end{cases} \tag{2.17}$$

where $\mathrm{sinc}(s) = \sin(s)/s$ is the sinc function and J_0 is the Bessel function of the first kind and of order zero.

Therefore, it follows that

$$\mathcal{I}_{\mathrm{BP}}(z^S,\omega) \approx -\sum_{p=1}^{P} |D_p| k_0^2 \Big(2\frac{\mu_p-\mu_0}{\mu_0+\mu_p} + (\frac{\varepsilon_p}{\varepsilon_0}-1)\Big) \times \begin{cases} \mathrm{sinc}(2k_0|z^S-z_p|) & \text{for } d=3, \\ J_0(2k_0|z^S-z_p|) & \text{for } d=2\ . \end{cases}$$

These imaging functional will have peaks at the location of the inclusions. Also, these formulas show that the resolution of the imaging functional is the standard diffraction limit. It is of the order of half the wavelength $\lambda = 2\pi/k_0$.

2.3.3. Kirchhoff Migration. Note that $\mathcal{I}_{\mathrm{BP}}$ uses only the diagonal terms of the response matrix A, we would like to use the whole matrix as it would give a more stable and precise imaging method. As in MUSIC, consider the response matrix given by $U_l(x) = e^{ik_0\theta_l\cdot x}, w_l(x) = e^{-ik_0\theta_l\cdot x}, l = 1,\dots,n$. Motivated by the rewriting of the response matrix given by 2.14, we define the Kirchhoff migration functional as:

$$\mathcal{I}_{\mathrm{KM}}(z^S,\omega) = \sum_{j=1}^{d+1} \overline{g^{(j)}(z^S)}\cdot A g^{(j)}(z^S)\ , \tag{2.18}$$

where $g^{(j)}$ are defined by (2.12) and (2.13). When developing this operation, one arrives to terms of the form

$$\sum_{j=1}^{d+1}\sum_{k=1}^{d+1} |g^{(j)}(x)\cdot g^{(k)}(z_p)|^2,$$

that given some approximate orthogonality of these vectors when location x do not match the location of the inclusion z_p; this property allows us to find the z_p.

2.3.4. Numerical simulations. For numerical simulations we consider a fixed frequency $k_0 = 12$, domain D the unitary disc, background constants $\mu_0 = \varepsilon_0 = 1$ and two disc inclusions: one electrical inclusion with $\varepsilon_* = 5$ and radius 0.1, and one magnetic inclusion with $\mu_* = 2$ with radius 0.15. See figure 2.4 to visualize the configuration.

The codes for backpropagation and Kirchhoff migration are straightforward from the exposed fomulae. MUSIC on the contrary is not straight forward to code, as it is based on studying the range of the response matrix; small perturbations of this matrix will result on a full rank one, thus there is a need to regularize it to reduce the rank. To this purpose it is safe to first decompose the matrix with an

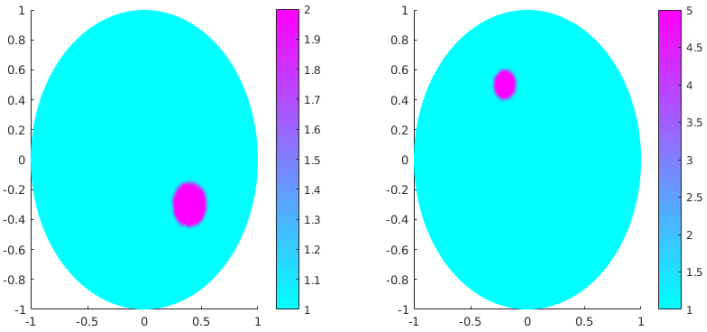

FIGURE 2.4. Considered domain for the Helmholtz equation. To the left the location of the electric inclusion, to the right hand side the location of the magnetic inclusion.

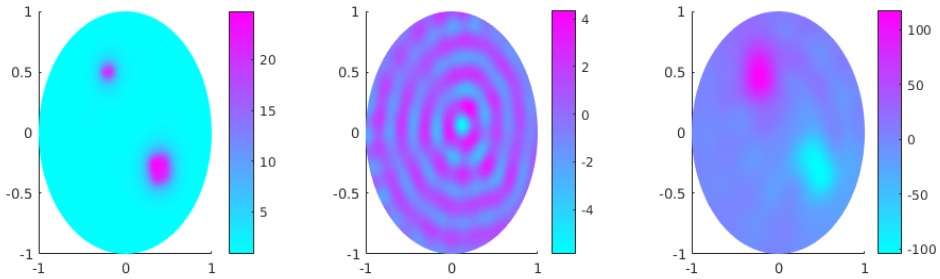

FIGURE 2.5. The inclusion location methods. From left to right hand side: MUSIC, Backpropagation and Kirchhoff migration.

SVD decomposition and discard the matrices with a small enough singular value; this smoothing process bounds the rank of the response matrix to any desired size.

MUSIC, backpropagation and Kirchhoff migration were tested for this setting, the results can be seen on figure 2.5.It can be seen that both Kirchhoff and MUSIC are accurate to locate the center of the inclusion, whereas backpropagation gives rather poor results, aiming to some inclusion located in between them.

Backpropagation seems to fail by numerical errors, and given that the method only considers the diagonal terms of the response matrix, it is expected to be sensitive to small perturbations as it uses a small amount of data. Kirchhoff migration locates accurately the inclusions and give as added information some intensity values that range to positive and negative, this information could be used successfully to obtain even more information about the inclusions, for instance if its of magnetic or electric nature. MUSIC algorithm also locates successfully the locations of the inclusions, but it does not give more information about them.

CHAPTER 3

Coupled-physics imaging

3.1. Photoacoustic Imaging

As seen in course, the problem photo-acoustic inverse problem is closely related to be able to obtain the location of sound sources at time $t = 0$ from measurements from the boundary. And we saw in Section 1.4, this is related to the inversion of the spherical means Radon transform operator (SmRt).

For the case of the unitary sphere $\mathcal{S}$, we have an explicit formula to invert the SmRt presented in subsection 1.4.2. This is filtered backprojection algorithm

$$\mathcal{R}^*\mathcal{B}\mathcal{R}[f],$$

where $\mathcal{R}$ is the SmRt operator, $\mathcal{B}$ is a filter operator and $\mathcal{R}^*$ is the adjoint of the SmRt. Although we have an exact inversion formula, it is ill-behaved when the measurements $\mathcal{R}[f]$ are not proper. For instance we could have a low amount of measurement on the boundary, that in practice means that the measurements were done with a scarse amount of tranducers; partial measurements, where we cannot access the information over the whole boundary of the target; or presence of noise in the measurements.

To approach these issues we look at another way of recovering the data from the measurements. Let g be the measurements of our inverse problem, and A be a model of the data, the inverse problem we are interested to solve is to find f such that $Af = g$. This problem could be ill-posed or simply there could not be any solutions. Thus we formulate it in a way that gives us a well-posed problem, for instance

$$\text{find } u \text{ such that minimizes } \frac{1}{2}||Au - g||^2_{L^2} - \lambda J(u), \tag{3.1}$$

where the first term $||Au - g||$ is a term that seeks to get a solution that, according to the model A, produces measurements close to the real ones; the second term $\lambda J(u)$ is a term where we can include some a priori information, acting as a regularization term.

This formulation is typical in Tikhonov regularization, where the idea is to impose stability of the inversion of an ill-posed problem. The standard choices are picking $J(\cdot)$ as $\frac{1}{2}||\cdot||^2_{L^2}$ or $\frac{1}{2}||\nabla \cdot ||^2_{L^2}$. These choices are advantageous as they give an easy minimization problem, but in the context of medical imaging, we would like to have solutions that give good images.

In the image denoising area, it is considered a good image one that satisfies both good spatial resolution and preserves edges. By considering $J(\cdot) = ||\cdot||^2_{L^2}$ there is not much gain in space regularity, and by choosing $J(\cdot) = ||\nabla \cdot ||^2_{L^2}$ we loose the edges. A popular choice of image denoising is to consider J as the total variation, since it gives both space regularity and preserves edges.

3.1.1. Total Variation. We might want something like $J(u) = ||\nabla u||_{L^1}$, that is clearly well defined for $u \in W^{1,1}$. But the problem is that the family of functions that have weak derivatives with finite L^1 norm cannot present discontinuities across hypersurfaces, thus are not proper if we want an edge preserving image from problem 3.1. The total variation extends this choice of $J(u)$ to non continuous functions.

In one dimension, the total variation is defined as

$$|u|_{TV([a,b])} = \sup_{P\in\mathcal{P}} \sum_{i=0}^{|P|-1} |u(x_{i+1}) - u(x_i)|, \quad x_i \in P,$$

where $\mathcal{P}$ is the family of partitions of the interval $[a, b]$. In more dimensions, the total variation is defined by duality. For $u \in L^1(\Omega), \Omega \subset \mathbb{R}^d$ we have

$$|u|_{TV(\Omega)} = \sup\left\{ \int_\Omega u(x)\mathrm{div}\varphi(x)dx : \ \varphi \in \mathcal{C}_c^1(\Omega, \mathbb{R}^d), \ ||\varphi||_{L^\infty} \leq 1 \right\}.$$

The total variation has some properties that are of interest for image denoising:

(1) If $u \in \mathcal{C}^1$, then $|u|_{TV(\Omega)} = ||\nabla u||_{L^1}$.
(2) The family of functions with finite total variation (the bounded variation functions) allows discontinuous functions across hypersurfaces.
(3) If E is a set with smooth $\mathcal{C}^{1,1}$ boundary, then
$$|\chi_E|_{TV} = |\partial E|.$$
This can be proved by using the total variation formula, pick any $\varphi \in K := \{\varphi \in \mathcal{C}_c^1, ||\varphi||_{L^\infty} \leq \infty\}$ then
$$\int_\Omega \chi_E(x)\mathrm{div}\varphi(x) = \int_{\partial E} \varphi \cdot \nu d\sigma,$$
where ν is the normal derivative. This integral can be maximized by choosing $\varphi = \nu$, which is possbile given the regularity of the E, by doing so we obtain
$$\int_\Omega \chi_E(x)\mathrm{div}\varphi(x) \leq \int_{\partial E} |\nu|^2 d\sigma = |\partial E|,$$
and we can conclude.
(4) The total variation is a convex operator. This stems from the fact that it can be written as the supremum of linear functions. Consider for $\varphi \in K$ the linear functions
$$L_\varphi : u \to \int_\Omega u(x)\mathrm{div}\varphi(x)dx,$$
hence by definition of the total variation, we have
$$|u|_{TV} = \sup_{\varphi\in K} L_\varphi(u).$$

The first property gives an idea of what it is penalizing, while the second property tells us that it allows discontinuous functions and hence, would give edge preserving images. The third property tells us that penalizing the total variation will also try to minimize the length of the boundaries, hence smoothing high frequencies on them. Finally the convexity property is the most important one for optimization, as it allows us to use a wide family of optimization techniques.

3.1.2. Optimization algorithms. The problem we seek to minimize is 3.1 with J as the total variation, basically it is the sum of two convex functions. For this will use the iterative shrinkage algorithm (ISTA), with a little step modification that gives a faster convergence speed (FISTA). The ISTA can be viewed as a split, gradient-descent, iterative scheme, we will review the main ideas behind it.

3.1.2.1. *Gradient descent.* Let f be a smooth function, then the gradient descent with step s is given by iterating

$$x^+ = x - s \cdot \nabla f(x).$$

3.1.2.2. *Proximal gradient descent.* The idea is to minimize a local quadratic approximation of f and replacing $\nabla^2 f(x)$ by I/s, this gives as update step

$$x^+ = \arg\min_z \tilde{f}_s(z, x) =: \arg\min_z f(x) + \nabla f(x)^t (z - x) + \frac{1}{2s}||z - x||_2^2.$$

At first glance it does not look like a good idea, but the main advantage of it is that it solves a minimization problem that is independent of f, as it only evaluates its value and derivative, and afterwards minimize a simple d dimensional quadratic function.

3.1.2.3. *Iterative shrinkage method (ISTA).* Consider $f = G + J$ the sum of two functions, where G is differentiable. The idea is to implement an splitting method: we minimize first one function and afterwards the other one, but there is some joint minimization as we will use the proximal gradient descent idea. The update step is given by

$$\begin{aligned} x^+ &= \arg\min_z \tilde{G}_s(z, x) + J(z) \\ &= \arg\min_z G(x) + \nabla G(x)^t (z - x) + \frac{1}{2s}||z - x||_2^2 \\ &= \arg\min_z + J(z) \frac{1}{2s}||z - (x - s\nabla G(x))||_2^2 + J(z) \end{aligned}$$

So written in another fashion, we define the proximal step

$$\text{prox}_s(x) = \arg\min_z \frac{1}{2s}||x - z||_2^2 + J(z),$$

and thus, the update step becomes

$$x^+ = \text{prox}_s(x - s\nabla G(x)).$$

The improvement obtained by this method is that now it is only needed to minimize J added to a quadratic function, in the particular case of the total variation we have an algorithm to obtain accurately the value of $\text{prox}_t(x)$.

Observe that for the particular case we want to deal with, being $G(x) = \frac{1}{2}||\mathcal{R}x - g||_2^2$ we have

$$\langle \nabla G(x), y \rangle = \langle \mathcal{R}x - g, \mathcal{R}y \rangle = \langle \mathcal{R}^* (\mathcal{R}x - g), y \rangle .$$

Thus we can easily compute the gradient $\nabla G(x) = \mathcal{R}^* (\mathcal{R}x - g)$.

3.1.2.4. *Fast iterative shrinkage method (FISTA).* This is a modification to the ISTA by Beck and Teboulle (2009) that speeds up the convergence speed of it. It adds an extra intermediate variable and a dynamic step size. The algorithm will be written for the specific problem we are dealing with.

$$\begin{aligned} &y_0 = 0,\ x_0 = 0,\ s_0 = 1 \\ &x_{k+1} = \text{prox}_{\gamma\tau}\left(y_k - \gamma\mathcal{R}^*\left(\mathcal{R}[x_k] - g\right)\right) \\ &s_{k+1} = \frac{1+\sqrt{1+4s_k^2}}{2} \\ &y_{k+1} = x_{k+1} + \frac{s_k - 1}{s_{k+1}}(x_{k+1} - x_k) \end{aligned}$$

3.1.2.5. *Minimization of the total variation.* To be able to compute the proximal operator in the case of the total variation, we need to solve

$$\min_u \frac{||u-g||_2^2}{2\lambda} + |u|_{TV}.$$

This minimization problem is treated by Chambelle's paper *And algorithm for total variation minimization and applications*. The key ingredient is to prove that the solution is given by

$$u = g - \pi_{\lambda\overline{K}}(g),$$

with K defined before as the set where we take the supremum for the total variation and $\pi_{\lambda K}$ the projection operator. To compute efficiently this projection, we have the following algorithm

$$\begin{aligned} &p_0 = 0 \in \Omega, \tau \in (0, 1/8) \\ &p_{n+1} = \frac{p_n + \tau\left(\nabla(\text{div}p_n - g/\lambda)\right)}{1 + \tau|\left(\nabla(\text{div}p_n - g/\lambda)\right)|} \\ &\lambda\text{div}(p_{\text{end}}) = \pi_{\lambda\overline{K}}(g) \end{aligned}$$

3.1.3. Numerical Simulation. Following the guidelines of the previous algorithms, we can implement the total variation regularization for reconstruction with incomplete data. Following the same example as the one given in figure 1.7 the obtained regularized reconstruction can be seen in 3.1. It can be observed a clear enhancement in the reconstruction, it is a more uniform object and at the same time the background inversion errors, where the strong negative values are found, are well reconstructed.

3.2. Using multiple frequencies in thermoacoustic tomography

3.2.1. Main results. Given a smooth bounded domain $\Omega \subseteq \mathbb{R}^d$, $d = 2, 3$, we consider the Dirichlet boundary value problem

$$\begin{cases} -\Delta u_\omega^i - (\omega^2\varepsilon + i\omega\sigma)\, u_\omega^i = 0 & \text{in } \Omega, \\ u_\omega^i = g_i & \text{on } \partial\Omega. \end{cases} \tag{3.2}$$

We assume that $\varepsilon, \sigma \in L^\infty(\Omega; \mathbb{R})$ and satisfy

$$\Lambda^{-1} \leq \varepsilon, \sigma \leq \Lambda \ \text{ almost everywhere in } \Omega \tag{3.3}$$

for some $\Lambda > 0$ and that $g_i \in C^{1,\alpha}(\overline{\Omega}; \mathbb{C})$ for some $\alpha \in (0, 1)$. For the derivation of this PDE we refer to §14 of the lecture notes.

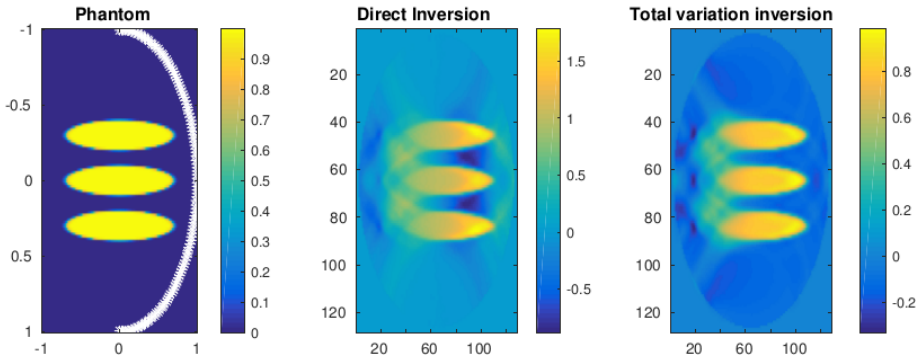

FIGURE 3.1. The object to reconstruct and the location of the transducers to the left, on the middle the reconstruction using the inverse formula. On the right hand side the reconstruction with the total variation regularization.

FIGURE 3.2. The domain $D = \{\omega \in \mathbb{C} : |\Im\omega| < \eta\}$ and the admissible set $\mathcal{A}$.

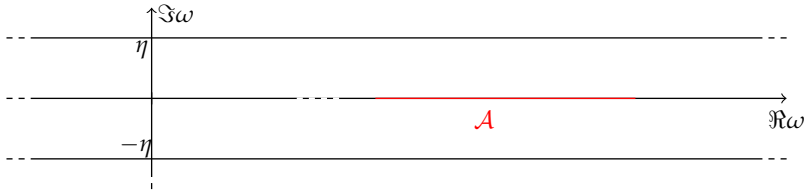

By classical elliptic theory we have the following existence and regularity result.

PROPOSITION 3.1. *There exists $\eta > 0$ depending on Ω and Λ only such that for $\omega \in B(0, M)$ with $|\Im\omega| \leq \eta$, $f \in L^\infty(\Omega;\mathbb{C})$, $F \in C^{0,\alpha}(\overline{\Omega};\mathbb{C}^3)$ and $g \in C^{1,\alpha}(\overline{\Omega};\mathbb{C})$ the problem*

$$\begin{cases} -\Delta u - (\omega^2\varepsilon + i\omega\sigma)\, u = \operatorname{div}(F) + f & \text{in } \Omega, \\ u = g & \text{on } \partial\Omega, \end{cases} \tag{3.4}$$

has a unique solution $u \in C^{1,\alpha}(\overline{\Omega};\mathbb{C})$ with

$$\|u\|_{C^{1,\alpha}(\overline{\Omega};\mathbb{C})} \leq C(\Omega, \Lambda, M) \left[\|g\|_{C^{1,\alpha}(\overline{\Omega};\mathbb{C})} + \|F\|_{C^{0,\alpha}(\overline{\Omega};\mathbb{C}^3)} + \|f\|_{L^\infty(\Omega;\mathbb{C})} \right]. \tag{3.5}$$

Let $\mathcal{A} = [K_{min}, K_{max}]$ represent the frequencies we have access to, for some $0 < K_{min} < K_{max}$. Set $D := \{\omega \in \mathbb{C} : |\Im\omega| < \eta\}$. Figure 3.2 represents the domain D and the admissible set of frequencies $\mathcal{A}$.

We introduce the particular class of sets of measurements we are interested in.

DEFINITION 3.2. A set of measurements $K \times \{g_1, \dots, g_{d+1}\}$ is *C-proper* if there exists an open cover of $\overline{\Omega}$

$$\overline{\Omega} = \bigcup_{\omega \in K} \Omega_\omega,$$

such that for any $\omega \in K$

$$|u^1_\omega(x)| \geq C, \qquad x \in \Omega_\omega, \tag{3.6a}$$

$$\left|\det \begin{bmatrix} u^1_\omega & \cdots & u^{d+1}_\omega \\ \nabla u^1_\omega & \cdots & \nabla u^{d+1}_\omega \end{bmatrix}\right| \geq C, \qquad x \in \Omega_\omega. \tag{3.6b}$$

Namely, a C-proper set gives a cover of $\overline{\Omega}$ into $\#K$ subdomains, such that the constraints given in (3.6) are satisfied in each subdomain for different frequencies. Once this is achieved, the exact reconstruction formula for thermoacoustic tomography discussed in the lecture notes may be applied in each subdomain for different values of the frequency, and reconstruct the unknown parameter everywhere.

We now describe how to choose the frequencies in the admissible set $\mathcal{A}$. Let $K^{(n)}$ be the uniform partition of $\mathcal{A}$ into $n-1$ intervals so that $\#K^{(n)} = n$, namely

$$K^{(n)} = \{\omega^{(n)}_1, \dots, \omega^{(n)}_n\}, \qquad \omega^{(n)}_i = K_{min} + \frac{(i-1)}{(n-1)}(K_{max} - K_{min}). \tag{3.7}$$

The main result of this section reads as follows.

THEOREM 3.3. *Assume that* (3.3) *holds true. There exist $C > 0$ and $n \in \mathbb{N}$ depending on Ω, Λ and $\mathcal{A}$ such that*

$$K^{(n)} \times \{1, x_1, \dots, x_d\}$$

is a C-proper set of measurements.

3.2.2. Quantitative unique continuation. The following result is a quantitative version of the unique continuation property for holomorphic functions of one complex variable.

LEMMA 3.4. *Take $0 < r < R_1$ and $0 < R_2$. Let g be a holomorphic function in the ellipse*

$$E = \{\omega \in \mathbb{C} : \frac{(\Re\omega)^2}{R_1^2} + \frac{(\Im\omega)^2}{R_2^2} < 1\}$$

such that $|g(0)| \geq C_0 > 0$ and $\sup_E |g| \leq D$. There exists $\omega \in [r, R_1)$ such that

$$|g(\omega)| \geq C$$

for some constant $C > 0$ depending only on R_1, R_2, r, D and C_0.

PROOF. Since $[r, (R_1 + r)/2] \subseteq [r, R_1)$, it is sufficient to show that there exists $C > 0$ depending on R_1, R_2, r, D and C_0 only such that

$$\max_{[r,(R_1+r)/2]} |g| \geq C.$$

By contradiction, suppose that there exists a sequence $(g_n)_n$ of holomorphic functions in E such that $\sup_E |g_n| \leq D$, $|g_n(0)| \geq C_0$ and $\max_{[r,(R_1+r)/2]} |g_n| \to 0$. Since $\sup_E |g_n| \leq D$, by standard complex analysis, up to a subsequence $g_n \to g_\infty$ for some g_∞ holomorphic in E. As $\max_{[r,(R_1+r)/2]} |g_n| \to 0$, we obtain $g_\infty = 0$ on $[r, (R_1 + r)/2]$, whence $g_\infty = 0$, which contradicts $|g_\infty(0)| \geq C_0$. □

3.2.3. Proof of Theorem 3.3. We now prove Theorem 3.3. For simplicity, we shall say that a positive constant depends on a priori data if it depends only on Ω, Λ and $\mathcal{A}$.

We first show that the map $\omega \in D \mapsto u^i_\omega \in C^\kappa$ is holomorphic. This will be one of the basic tools of the proof of Theorem 3.3.

PROPOSITION 3.5. *Under the assumptions of Theorem 3.3, the map*

$$D \longrightarrow C^1(\overline{\Omega};\mathbb{C}), \quad \omega \longmapsto u^i_\omega$$

is holomorphic.

PROOF. Fix $\omega_0 \in D$: we are going to show that $f\colon \omega \in D \mapsto u^i_\omega \in C^1(\overline{\Omega};\mathbb{C})$ is holomorphic in ω_0. Let $\omega \in D$. A direct calculation shows that $v(\omega) = (f(\omega) - f(\omega_0))/(\omega - \omega_0)$ solves

$$\begin{cases} -\Delta v_\omega - (\omega_0^2\varepsilon + \mathrm{i}\omega_0\sigma)\, v_\omega = ((\omega+\omega_0)\varepsilon + \mathrm{i}\sigma) f(\omega) & \text{in } \Omega, \\ v_\omega = 0 \qquad \text{on } \partial\Omega. \end{cases}$$

By Proposition 3.1, we have that $v(\omega) \to w$ in the norm of $C^1(\overline{\Omega};\mathbb{C})$ as $\omega \to \omega_0$, where w is the unique solution of

$$\begin{cases} -\Delta w - (\omega_0^2\varepsilon + \mathrm{i}\omega_0\sigma)\, w = (2\omega_0\varepsilon + \mathrm{i}\sigma) f(\omega_0) & \text{in } \Omega, \\ w = 0 \qquad \text{on } \partial\Omega. \end{cases}$$

This shows that

$$\lim_{\omega\to\omega_0} \frac{f(\omega) - f(\omega_0)}{\omega - \omega_0} \in C^1(\overline{\Omega};\mathbb{C}),$$

namely the map f is holomorphic in ω_0. □

Define for $j = 1, 2$ the maps $\theta^j\colon D \to C(\overline{\Omega};\mathbb{C})$ given by

$$\theta^1(\omega) = u^1_\omega, \qquad \theta^2(\omega) = \det \begin{bmatrix} u^1_\omega & \cdots & u^{d+1}_\omega \\ \nabla u^1_\omega & \cdots & \nabla u^{d+1}_\omega \end{bmatrix}$$

As a consequence of the previous result and of the fact that compositions of holomorphic maps are holomorphic, the maps θ^j are holomorphic.

We next study some a priori bounds on θ^j and $\partial_\omega\theta^j$, which immediately follow from Proposition 3.1.

LEMMA 3.6. *There exists $C > 0$ depending on a priori data such that for every $j = 1, 2$ and $\omega \in B(0, M) \cap D$ we have*

(1) $\left\|\theta^j_\omega\right\|_{C(\overline{\Omega};\mathbb{C})} \le C$;
(2) $\left\|\partial_\omega\theta^j_\omega\right\|_{C(\overline{\Omega};\mathbb{C})} \le C$.

The next lemma is the last step needed for the proof of Theorem 3.3.

LEMMA 3.7. *For every $x \in \Omega$ there exists $\omega_x \in \mathcal{A}$ such that*

$$\left|\theta^j_{\omega_x}(x)\right| \ge C, \qquad j = 1, \dots, r$$

for some $C > 0$ depending on a priori data.

PROOF. Several positive constants depending on a priori data will be denoted by C.

Take $x \in \Omega$ and define

$$g_x(\omega) = \theta^1_\omega(x)\theta^2_\omega(x), \quad \omega \in D.$$

Since the maps θ^j are holomorphic, the map g_x is holomorphic in D and by Lemma 3.6, part (1), $\max_{B(0,M)\cap D}|g_x| \le C$. Moreover, $|g_x(0)| = 1$, since $u^1_0 \equiv 1$ and $u^i_0 \equiv x_{i-1}$ for $i = 2, \dots, d+1$ (which follow from the fact that 1 and x_{i-1} solve the Laplace equation). Therefore, by Lemma 3.4 with $r = K_{min}$, $R_1 = K_{max}$, and $R_2 = \eta$ there exists $\omega_x \in \mathcal{A}$ such that $|g_x(\omega_x)| \ge C$. The result now follows from Lemma 3.6, part (1). □

We are now ready to prove Theorem 3.3.

PROOF OF THEOREM 3.3. Different positive constants depending on a priori data will be denoted by C or Z.

In view of Lemma 3.7, for every $x \in \Omega$ there exists $\omega_x \in \mathcal{A}$ such that

$$|\theta^j_{\omega_x}(x)| \ge C, \qquad j = 1, 2.$$

Thus, by Lemma 3.6, part (2), there exists $Z > 0$ such that

$$|\theta^j_\omega(x)| \ge C, \qquad \omega \in [\omega_x - Z, \omega_x + Z] \cap \mathcal{A},\ j = 1, 2. \tag{3.8}$$

Recall that $\mathcal{A} = [K_{min}, K_{max}]$ and that $\omega^{(n)}_i = K_{min} + \frac{(i-1)}{(n-1)}(K_{max} - K_{min})$. It is trivial to see that there exists $P = P(Z, |\mathcal{A}|) \in \mathbb{N}$ such that

$$\mathcal{A} \subseteq \bigcup_{p=1}^{P} I_p, \qquad I_p = [K_{min} + (p-1)Z, K_{min} + pZ]. \tag{3.9}$$

Choose now $n \in \mathbb{N}$ big enough so that for every $p = 1, \dots, P$ there exists $i_p = 1, \dots, n$ such that $\omega(p) := \omega^{(n)}_{i_p} \in I_p$. Note that n depends on Z and $|\mathcal{A}|$ only.

Take now $x \in \overline{\Omega}$. Since $|[\omega_x - Z, \omega_x + Z]| = 2Z$ and $|I_p| = Z$, in view of (3.9) there exists $p_x = 1, \dots, P$ such that $I_{p_x} \subseteq [\omega_x - Z, \omega_x + Z]$. Therefore $\omega(p_x) \in [\omega_x - Z, \omega_x + Z] \cap \mathcal{A}$, whence by (3.8) there holds $|\theta^j_{\omega(p_x)}(x)| \ge C$ for all $j = 1, 2$. Recalling the definition of θ^j this implies

$$|u^1_{\omega(p_x)}(x)| \ge C, \qquad |\det \begin{bmatrix} u^1_{\omega(p_x)} & \cdots & u^{d+1}_{\omega(p_x)} \\ \nabla u^1_{\omega(p_x)} & \cdots & \nabla u^{d+1}_{\omega(p_x)} \end{bmatrix}(x)| \ge C. \tag{3.10}$$

Define now

$$\Omega_\omega = \{x \in \overline{\Omega} : |u^1_\omega(x)| > C/2,\ |\det \begin{bmatrix} u^1_\omega & \cdots & u^{d+1}_\omega \\ \nabla u^1_\omega & \cdots & \nabla u^{d+1}_\omega \end{bmatrix}(x)| > C/2\}.$$

By (3.10) this gives an open cover $\overline{\Omega} = \cup_{\omega \in K^{(n)}} \Omega_\omega$, since $\omega(p_x) \in K^{(n)}$. As a consequence, $K^{(n)} \times \{1, x_1, \dots, x_d\}$ is C-proper (Definition 3.2). The theorem is proved. □

3.3. Ultrasonically Induced Lorentz Force Imaging

Let a physical object to be imaged occupy a three-dimensional domain Ω with a smooth boundary $\partial\Omega$. Assume that this body is placed in a constant magnetic field B in the direction e_3 where $\{e_1, e_2, e_3\}$ denotes the standard orthonormal basis of $\mathbb{R}^3$. We are interested in recovering the electrical conductivity of this body $\sigma \in L^\infty(\Omega)$ with the known lower and upper bounds:

$$0 < \underline{\sigma} \leq \sigma \leq \overline{\sigma} < \infty\,.$$

An acoustic transducer sends a short acoustic pulse from $y \in \mathbb{R}^3$ in the direction $\xi \in S$, with S being the unit sphere, such that $\xi \cdot e_3 = 0$. This pulse generates the velocity field $v(x,t)\xi$.

3.3.1. The Ionic Model of Conductivity. We describe here the electrical behavior of the medium as an electrolytic tissue composed of ions capable of motion in an aqueous tissue. We consider k types of ions in the medium with charges of q_i, $i \in \{1,\dots,k\}$. The corresponding volumetric density n_i is assumed to be constant. Neutrality in the medium is described as

$$\sum_i q_i n_i = 0\,. \tag{3.11}$$

The Kohlrausch law defines the conductivity of such a medium as a linear combination of the ionic concentrations

$$\sigma = e^+ \sum_i \mu_i q_i n_i, \tag{3.12}$$

where e^+ is the elementary charge, and the coefficients μ_i denote the ionic mobility of each ion i.

3.3.2. Ion Deviation by Lorentz Force. We embed the medium in a constant magnetic field B with direction e_3, and perturb it mechanically using the short, focused, ultrasonic pulses v defined above. The motion of the charged particle i inside the medium is deviated by the Lorentz force

$$F_i = q_i v\xi \times B\,. \tag{3.13}$$

This force accelerates the ion in the orthogonal direction $\tau = \xi \times e_3$. Then, almost immediately, the ion reaches a constant speed given by,

$$v_{\tau,i} = \mu_i |B| v$$

at the first order, where μ_i are coefficients depending on the ion. Finally, the ion i has a total velocity

$$v_i = v\xi + \mu_i |B| v\tau\,.$$

The current density generated by the displacement of charges can be described as follows:

$$j_S = \sum_i n_i q_i v_i = \left(\sum_i n_i q_i\right) v\xi + \left(\sum_i n_i \mu_i q_i\right) |B| v\tau\,.$$

Using the neutrality condition (3.11) and the definition of σ in (3.12), we get the following simple formula for j_S:

$$j_S = \frac{1}{e^+}|B|\sigma v\tau\,. \tag{3.14}$$

This electrolytic description of the tissue characterizes the interaction between the ultrasonic pulse and the magnetic field through a small deviation of the charged particles embedded in the tissue. This deviation generates a current density j_S orthogonal to ξ and to B, locally supported inside the domain. At a fixed time t, j_S is supported in the support of $x \mapsto v(x,t)$. This current is proportional to σ, and is the source of the current that we measure on the electrodes placed at $\partial\Omega$. In the next section, a formal link is substantiated between j_S and the measured current I.

3.3.3. Internal Electrical Potential. Because the characteristic time of the acoustic propagation is very long compared with the electromagnetic wave propagation characteristic time, we can adopt the electrostatic frame. Consequently, the total current j in Ω at a fixed time t can be formulated as

$$j = j_S + \sigma\nabla u\,, \tag{3.15}$$

where u is the electrical potential. It satisfies

$$\nabla\cdot(j_S + \sigma\nabla u) = \nabla\cdot j = 0\,. \tag{3.16}$$

Let Γ_1 and Γ_2 be portions of the boundary $\partial\Omega$ where two planner electrodes are placed. Denote $\Gamma_0 = \partial\Omega \setminus (\Gamma_1 \cup \Gamma_2)$.

As we measure the current between the two electrodes Γ_1 and Γ_2, the electrical potential is the same on both electrodes, and can be fixed to zero without loss of generality. Further, it is assumed that no current can leave from Γ_0. The potential u can then be defined as the unique solution in $W^{1,2}(\Omega)$ of the elliptic system

$$\begin{cases} -\nabla\cdot(\sigma\nabla u) = \nabla\cdot j_S & \text{in } \Omega\,, \\ u = 0 & \text{on } \Gamma_1 \cup \Gamma_2\,, \\ \partial_\nu u = 0 & \text{on } \Gamma_0\,. \end{cases} \tag{3.17}$$

Where ∂_ν denotes the normal derivative. Note that the source term j_S depends on the time $t > 0$, the position of the acoustic transducer $y \in \mathbb{R}^3$, and the direction $\xi \in S$. The electrical potential u also depends on these variables.

The measurable intensity I is the current flow through the electrodes. Integrating (3.17) by parts gives

$$\int_{\Gamma_1} \sigma\partial_\nu u + \int_{\Gamma_2} \sigma\partial_\nu u = 0\,,$$

which is the expression of current flow conservation. We define the intensity I by

$$I = \int_{\Gamma_2} \sigma\partial_\nu u\,. \tag{3.18}$$

3.3.4. Virtual Potential. In order to link I to σ, we introduce a virtual potential $U \in W^{1,2}(\Omega)$ defined as the unique solution of

$$\begin{cases} -\nabla\cdot(\sigma\nabla U) = 0 & \text{in } \Omega\,, \\ U = 0 & \text{on } \Gamma_1\,, \\ U = 1 & \text{on } \Gamma_2\,, \\ \partial_\nu U = 0 & \text{on } \Gamma_0\,. \end{cases} \tag{3.19}$$

Then we multiply (3.17) by U and integrate by parts. Assuming that the support of v does not intersect the electrodes Γ_1 and Γ_2, we obtain

$$-\int_\Omega \sigma\nabla u\cdot\nabla U+\int_{\Gamma_2}\sigma\partial_\nu u=\int_\Omega j_S\cdot\nabla U\,.$$

From the property of U in (3.19) and the definition of I in (3.18), the above identity becomes

$$I=\int_\Omega j_S\cdot\nabla U\,.$$

The above identity links the measured intensity I to an internal information of σ using the expression of j_S in (3.14):

$$I=\frac{|B|}{e^+}\int_\Omega v(x,t)\sigma(x)\nabla U(x)dx\cdot\tau\,.$$

v depends on y, ξ, and t, so does I. We define the measurement function as

$$M_{y,\xi}(z)=\int_\Omega v(x,z/c)\sigma(x)\nabla U(x)dx\cdot\tau(\xi) \tag{3.20}$$

for any $y\in\mathbb{R}^3$, $\xi\in S$ and $z>0$.

Now we simplify the problem by assuming the displacement field $v(x,z/c)$ on direction ξ can be considered as concentrated as a delta function, hence we can approximately obtain $\sigma(x)\nabla U(x)\cdot\tau(\xi)$ as information. Under the hypothesis that $\forall x\in\Omega$ we can send at least two pulses with direction $\xi_1,\xi_2\in\mathcal{S}$ such that $\xi_1\times\xi_2\neq 0$, then we can get as information $\sigma(x)\nabla U(x)\forall x\in\Omega$. Our inverse problem then reduces to be able to recover σ out of the non linear data $\sigma\nabla U$.

3.3.5. Recovering the Conductivity by Optimal Control. In this section we assume that, according to the previous one, we are in the situation where we know a good approximation of the virtual current $D:=\sigma\nabla U$ in the sense of $L^2(\Omega)$. The objective here is to provide efficient methods for separating σ from D.

For $a<b$, let us denote by $L^\infty_{a,b}(\Omega):=\{f\in L^\infty(\Omega)\ :\ a<f<b\}$ and define the operator $\mathcal{F}:L^\infty_{\underline{\sigma},\overline{\sigma}}(\Omega)\longrightarrow W^{1,2}(\Omega)$ by

$$\mathcal{F}[\sigma]=U:\begin{cases}\nabla\cdot(\sigma\nabla U)=0 & \text{in }\Omega\,,\\ U=0 & \text{on }\Gamma_1\,,\\ U=1 & \text{on }\Gamma_2\,,\\ \partial_\nu U=0 & \text{on }\Gamma_0\,.\end{cases} \tag{3.21}$$

The following lemma holds.

LEMMA 3.8. *Let $d\mathcal{F}$ be the Fréchet derivative of $\mathcal{F}$. For any $\sigma\in L^\infty_{\underline{\sigma},\overline{\sigma}}(\Omega)$ and $h\in L^\infty(\Omega)$ such that $\sigma+h\in L^\infty_{\underline{\sigma},\overline{\sigma}}(\Omega)$ we have*

$$d\mathcal{F}[\sigma](h)=v:\begin{cases}\nabla\cdot(\sigma\nabla v)=-\nabla\cdot(h\nabla\mathcal{F}[\sigma]) & \text{in }\Omega\,,\\ v=0 & \text{on }\Gamma_1\cup\Gamma_2\,,\\ \partial_\nu v=0 & \text{on }\Gamma_0\,.\end{cases} \tag{3.22}$$

PROOF. Let us denote by $w = \mathcal{F}[\sigma+h] - \mathcal{F}[\sigma] - v$. This function is in $W^{1,2}(\Omega)$ and satisfies the equation

$$\nabla \cdot (\sigma \nabla w) = -\nabla \cdot (h \nabla (\mathcal{F}[\sigma+h] - \mathcal{F}[\sigma]))$$

with the same boundary conditions as v. We have the elliptic global control:

$$\|\nabla w\|_{L^2(\Omega)} \leq \frac{1}{\underline{\sigma}} \|h\|_{L^\infty(\Omega)} \|\nabla(\mathcal{F}[\sigma+h] - \mathcal{F}[\sigma])\|_{L^2(\Omega)} .$$

Since

$$\nabla \cdot (\sigma \nabla (\mathcal{F}[\sigma+h] - \mathcal{F}[\sigma])) = -\nabla \cdot (h \nabla \mathcal{F}[\sigma+h]) ,$$

we can also control $\mathcal{F}[\sigma+h] - \mathcal{F}[\sigma]$ with

$$\|\nabla(\mathcal{F}[\sigma+h] - \mathcal{F}[\sigma])\|_{L^2(\Omega)} \leq \frac{1}{\sqrt{\underline{\sigma}}} \|h\|_{L^\infty(\Omega)} \|\nabla \mathcal{F}[\sigma+h]\|_{L^2(\Omega)} .$$

Then, there is a positive constant C depending only on Ω such that

$$\|\nabla \mathcal{F}[\sigma+h]\|_{L^2(\Omega)} \leq C \sqrt{\frac{\overline{\sigma}}{\underline{\sigma}}} .$$

Finally, we obtain

$$\|\nabla w\|_{L^2(\Omega)} \leq C \frac{\sqrt{\overline{\sigma}}}{\underline{\sigma}^2} \|h\|^2_{L^\infty(\Omega)} ,$$

and the proof is complete. □ □

We look for the minimizer of the functional

$$J[\sigma] = \frac{1}{2} \int_\Omega |\sigma \nabla \mathcal{F}[\sigma] - D|^2 . \tag{3.23}$$

In order to do so, we compute its gradient. The following lemma holds.

LEMMA 3.9. *For any $\sigma \in L^\infty_{\underline{\sigma},\overline{\sigma}}(\Omega)$ and $h \in L^\infty(\Omega)$ such that $\sigma + h \in L^\infty_{\underline{\sigma},\overline{\sigma}}(\Omega)$,*

$$dJ[\sigma](h) = -\int_\Omega h \Big((\sigma \nabla \mathcal{F}[\sigma] - D - \nabla p) \cdot \nabla \mathcal{F}[\sigma] \Big) ,$$

where p is defined as the solution to the adjoint problem:

$$\begin{cases} \nabla \cdot (\sigma \nabla p) = \nabla \cdot (\sigma^2 \nabla \mathcal{F}[\sigma] - \sigma D) & \text{in } \Omega , \\ p = 0 & \text{on } \Gamma_1 \cup \Gamma_2 , \\ \partial_\nu p = 0 & \text{on } \Gamma_0 . \end{cases} \tag{3.24}$$

PROOF. As $\mathcal{F}$ is Fréchet differentiable, so is J. For $\sigma \in L^\infty_{\underline{\sigma},\overline{\sigma}}(\Omega)$ and $h \in L^\infty(\Omega)$ such that $\sigma + h \in L^\infty_{\underline{\sigma},\overline{\sigma}}(\Omega)$, we have

$$dJ[\sigma](h) = \int_\Omega (\sigma \nabla \mathcal{F}[\sigma] - D) x (h \nabla \mathcal{F}[\sigma] + \sigma \nabla d\mathcal{F}[\sigma](h)) .$$

Now, multiplying (3.24) by $d\mathcal{F}[\sigma](h)$, we get

$$\int_\Omega \sigma \nabla p \cdot \nabla d\mathcal{F}[\sigma](h) = \int_\Omega (\sigma^2 \nabla \mathcal{F}[\sigma] - \sigma D) \cdot \nabla d\mathcal{F}[\sigma](h) .$$

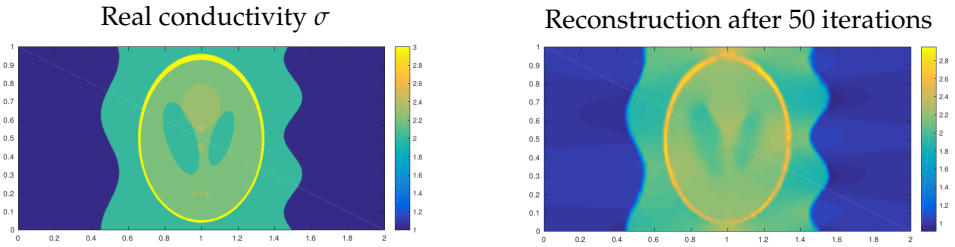

FIGURE 3.3. Objective function and its respective reconstruction with the gradient descent method.

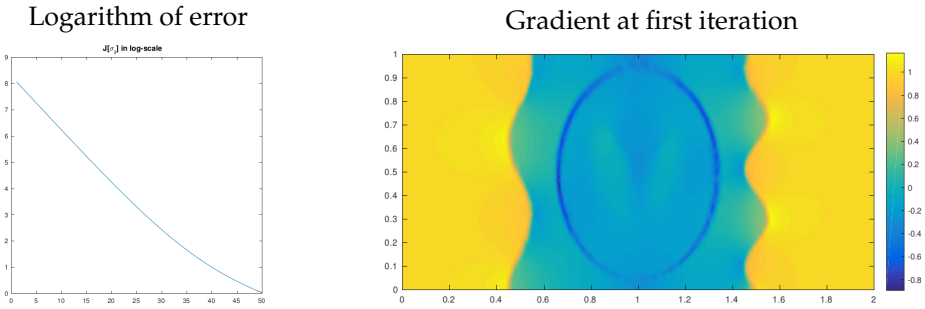

FIGURE 3.4. On the left we can see how the error decreases fast for each iteration. On the right we can see the first gradient, representing how the reconstruction converges at each step. This behavior is similar at each iteration.

On the other hand, multiplying (3.22) by p we arrive at

$$\int_\Omega \sigma \nabla p \cdot \nabla d\mathcal{F}[\sigma](h) = -\int_\Omega h \nabla \mathcal{F}[\sigma] \cdot \nabla p \,,$$

and therefore,

$$dJ[\sigma](h) = \int_\Omega h(\sigma \nabla \mathcal{F}[\sigma] - D - \nabla p) \cdot \nabla \mathcal{F}[\sigma] \,,$$

which completes the proof. □

Lemma 3.9 allows us to implement a numerical gradient descent method in order to find σ.

3.3.6. Numerical Implementation. The gradient descent method is implemented to reconstruct the value of σ out of data representing the value $\sigma \nabla \mathcal{F}[\sigma]$. In figure 3.3 we can see the real data and the obtained reconstruction with 50 iterations, the initial guess is constant equal to 2. In figure 3.4 we can see how the log-error $\log J[\sigma]$ evolves at each iteration and the shape of the derivative at time 0.

Overall, the method gives accurate reconstructions and is stable to noise. As it is natural, there is smoothing of the boundaries as we are minimizing the L^2 error.

3.4. Acousto-electromagnetic tomography

3.4.1. Introduction. This section focuses on the technique called acousto electromagnetic tomography. Spherical ultrasonic waves are sent from sources around the domain under investigation. The pressure variations create a displacement in the tissue, thereby modifying the electrical properties. Microwave boundary measurements are taken in the unperturbed and in the perturbed situation (see Figure 3.5). In a first step, as in Ultrasound-Modulated Optical Tomography (see the lecture notes) the cross-correlation of all the boundary values, after the inversion of a spherical mean Radon transform, gives the internal data of the form

$$|u_\omega(x)|^2 \nabla q(x),$$

where q is the spatially varying electric permittivity of the body $\Omega \subset \mathbb{R}^d$ for $d = 2, 3$, $\omega > 0$ is the frequency and u_ω satisfies the Helmholtz equation with Robin boundary conditions

$$\begin{cases} \Delta u_\omega + \omega^2 q u_\omega = 0 \text{ in } \Omega, \\ \frac{\partial u_\omega}{\partial \nu} - i\omega u_\omega = -i\omega\varphi \text{ on } \partial\Omega. \end{cases} \tag{3.25}$$

(In fact, only the gradient part ψ_ω of $|u_\omega|^2 \nabla q = \nabla \psi_\omega + \text{curl}\Phi$ is measured.) The second step of this hybrid methodology consists in recovering q from the knowledge of ψ_ω.

Denoting the measured datum by ψ^*_ω, we minimize the energy functional

$$J_\omega(q) = \frac{1}{2} \int_\Omega |\psi_\omega(q) - \psi^*_\omega|^2 dx$$

with a gradient descent method. In this case, this is equivalent to a Landweber iteration scheme. As explained in the lecture notes, the convergence of such algorithm is guaranteed provided that $\|D\psi_\omega[q](\rho)\| \geq C \|\rho\|$. This condition represents the uniqueness and stability for the linearized inverse problem $D\psi_\omega[q](\rho) \mapsto \rho$. In general, the kernel of $\rho \mapsto D\psi_\omega[q](\rho)$ may well be non-trivial.

In order to obtain an injective problem, we use a multiple frequency approach. If the boundary condition φ is suitably chosen (e.g. $\varphi = 1$), the kernels of the operators $\rho \mapsto D\psi_\omega[q](\rho)$ "move" as ω changes, and by choosing a finite number of frequencies K in a fixed range, determined a priori, it is possible to show that the intersection becomes empty. In particular, there holds $\sum_{\omega \in K} \|D\psi_\omega[q](\rho)\| \geq C \|\rho\|$ and the convergence of an optimal control algorithm for the functional $J = \sum_{\omega \in K} J_\omega$ follows (see Theorem 3.10). The idea is the same as the one used in Section 3.2, and extended here to an infinite-dimensional setting. Indeed, now we want to avoid kernels of operators instead of zeros of functions.

This section is structured as follows. §3.4.2 describes the physical model and the proposed optimization approach. In §3.4.3 we prove the convergence of the multi-frequency Landweber scheme. Some numerical simulations are discussed in §3.4.4.

3.4.2. Acousto-Electromagnetic Tomography. In this section we recall the coupled physics inverse problem of the Acousto-Electromagnetic Tomography.

3.4.2.1. *Physical Model.* We now briefly describe how to measure the internal data in the hybrid problem under consideration. The reader is referred to the part of lecture notes discussing the Ultrasound-Modulated Optical Tomography.

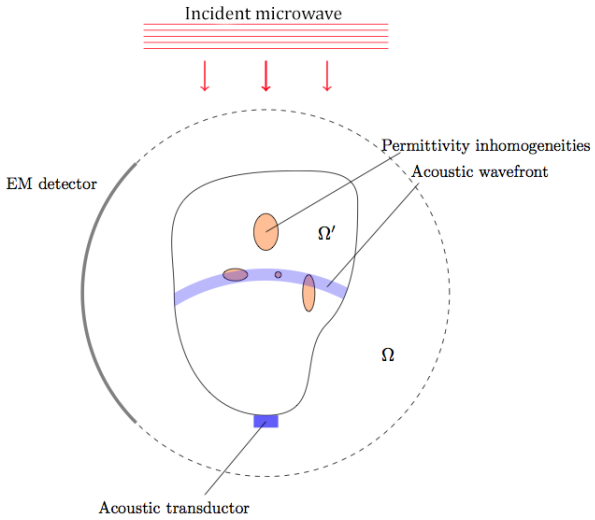

FIGURE 3.5. The acousto-electromagnetic tomography experiment.

Let $\Omega \subset \mathbb{R}^d$ be a bounded and smooth domain, for $d = 2$ or $d = 3$ and $q \in L^\infty(\Omega;\mathbb{R}) \cap H^1(\Omega;\mathbb{R})$ be the electric permittivity of the medium. We assume that q is known and constant near the boundary $\partial\Omega$, namely $q = 1$ in $\Omega \setminus \Omega'$, for some $\Omega' \Subset \Omega$. More precisely, suppose that $q \in Q$, where for some $\Lambda > 0$

(3.26)
$$Q := \{q \in H^1(\Omega;\mathbb{R}) : \Lambda^{-1} \leq q \leq \Lambda \text{ in } \Omega,\ \|q\|_{H^1(\Omega)} \leq \Lambda \text{ and } q = 1 \text{ in } \Omega \setminus \Omega'\}.$$

We model electromagnetic propagation in Ω at frequency $\omega \in \mathcal{A} = [K_{min}, K_{max}] \subset \mathbb{R}_+$ by (3.25). The boundary value problem model allows us to consider arbitrary q beyond the Born approximation, and so it is used here instead of the free propagation model. Problem (3.25) admits a unique solution $u_\omega \in H^1(\Omega;\mathbb{C})$ for a fixed boundary condition $\varphi \in H^1(\Omega;\mathbb{C})$ (see Lemma 3.12).

Let us discuss how microwaves are combined with acoustic waves. A short acoustic wave creates a displacement field v in Ω (whose support is the blue area in Figure 3.5), which we suppose continuous and bijective. Then, the permittivity distribution q becomes q_v defined by

$$q_v(x + v(x)) = q(x), \qquad x \in \Omega,$$

and the complex amplitude u_ω^v of the electric wave in the perturbed medium satisfies

$$\Delta u_\omega^v + \omega^2 q_v u_\omega^v = 0 \text{ in } \Omega. \tag{3.27}$$

Using (3.25) and (3.27), for v small enough we obtain the cross-correlation formula

$$\int_{\partial\Omega} \left(\frac{\partial u_\omega}{\partial n}\overline{u_\omega^v} - \frac{\partial \overline{u_\omega^v}}{\partial n} u_\omega\right) d\sigma = \omega^2 \int_\Omega (q_v - q) u_\omega \overline{u_\omega^v}\, dx \approx \omega^2 \int_\Omega |u_\omega|^2 \nabla q \cdot v\, dx,$$

By boundary measurements, the left hand side of this equality is known. Thus, we have measurements of the form

$$\int_\Omega |u_\omega|^2 \nabla q \cdot v \, dx,$$

for all perturbations v. As shown in the lecture notes, choosing radial displacements v allows to recover the gradient part of $|u_\omega|^2\nabla q$ by using the inversion for the spherical mean Radon transform. Namely, writing the Helmholtz decomposition of $|u_\omega|^2\nabla q$

$$|u_\omega|^2\nabla q = \nabla\psi_\omega + \mathrm{curl}\Phi_\omega,$$

for $\psi_\omega \in H_0^1(\Omega;\mathbb{R})$ and $\Phi_\omega \in H^1(\Omega;\mathbb{R}^{2d-3})$, the potential ψ_ω can be measured. Moreover, ψ_ω is the unique solution to

$$\begin{cases} \Delta\psi_\omega = \mathrm{div}(|u_\omega|^2\nabla q) & \text{in } \Omega, \\ \psi_\omega = 0 & \text{on } \partial\Omega. \end{cases} \tag{3.28}$$

In this part, we assume that the inversion of the spherical mean Radon transform has been performed and that we have access to ψ_ω. In the following, we shall deal with the second step of this hybrid imaging problem: recovering the map q from the knowledge of ψ_ω.

3.4.2.2. *The Landweber Iteration.* Let q^* be the real permittivity with corresponding measurements ψ_ω^*. Let $K \subset \mathcal{A}$ be a finite set of admissible frequencies for which we have the measurements ψ_ω^*, $\omega \in K$. The set K will be determined later. Let us denote the error map by

$$F_\omega \colon Q \to H_0^1(\Omega;\mathbb{R}), \qquad q \mapsto \psi_\omega(q) - \psi_\omega^*, \tag{3.29}$$

where $\psi_\omega(q)$ is the unique solution to (3.28), and $H_0^1(\Omega;\mathbb{R}) = \{u \in H^1(\Omega;\mathbb{R}) : u = 0 \text{ on } \partial\Omega\}$.

A natural approach to recover the real conductivity is to minimize the discrepancy functional J defined as

$$J(q) = \frac{1}{2}\sum_{\omega\in K}\int_\Omega |F_\omega(q)|^2 dx, \qquad q \in Q. \tag{3.30}$$

The gradient descent method can be employed to minimize J. At each iteration we compute

$$q_{n+1} = T\left(q_n - hDJ[q_n]\right),$$

where $h > 0$ is the step size and $T\colon H^1(\Omega;\mathbb{R}) \to Q$ is the Hilbert projection onto the convex closed set Q, which guarantees that at each iteration q_n belongs to the admissible set Q. Since $DJ[q] = \sum_\omega DF_\omega[q]^*(F_\omega(q))$, this algorithm is equivalent to the Landweber scheme given by

$$q_{n+1} = T\Big(q_n - h\sum_{\omega\in K} DF_\omega(q_n)^*(F_\omega(q_n))\Big). \tag{3.31}$$

(For the Fréchet differentiability of the map F_ω, see Lemma 3.14.)

The main result of this section states that the Landweber scheme defined above converges to the real unknown q^*, provided that K is suitably chosen and that h and $\|q_0 - q^*\|_{H^1(\Omega)}$ are small enough. The most natural choice for the set of frequencies K is as a uniform sample of $\mathcal{A}$, namely let

$$K^{(m)} = \{\omega_1^{(m)}, \dots, \omega_m^{(m)}\}, \qquad \omega_i^{(m)} = K_{min} + \frac{(i-1)}{(m-1)}(K_{max} - K_{min}).$$

THEOREM 3.10. *Set $\varphi = 1$. There exist $C > 0$ and $m \in \mathbb{N}^*$ depending only on Ω, Λ and $\mathcal{A}$ such that for any $q \in Q$ and $\rho \in H^1_0(\Omega;\mathbb{R})$*

$$\sum_{\omega \in K^{(m)}} \|DF_\omega[q](\rho)\|_{H^1(\Omega;\mathbb{R})} \geq C \|\rho\|_{H^1(\Omega;\mathbb{R})}. \tag{3.32}$$

As a consequence, the sequence defined in (3.31) converges to q^* provided that h and $\|q_0 - q^*\|_{H^1(\Omega)}$ are small enough.

The proof of this theorem is presented in §3.4.3. In view of what explained in the lecture notes, the convergence of the Landweber iteration follows from the Lipschitz continuity of F_ω and from inequality (3.32). The Lipschitz continuity of F_ω is a simple consequence of the elliptic theory.

On the other hand, the lower bound given in (3.32) is non-trivial, since it represents the uniqueness and stability of the multi-frequency linearized inverse problem

$$(DF_\omega[q](\rho))_{\omega \in K^{(m)}} \longmapsto \rho.$$

As it has been discussed in the Introduction, the kernels of the operators $\rho \mapsto DF_\omega[q](\rho)$ "move" as ω changes. More precisely, the intersection of the kernels corresponding to the a priori determined finite set of frequencies $K^{(m)}$ is empty. Moreover, the argument automatically gives an a priori constant C in (3.32).

The multi-frequency method is based on the analytic dependence of the problem with respect to the frequency ω, and on the fact that in $\omega = 0$ the problem is well posed. Indeed, when $\omega \to 0$ it is easy to see that $u_\omega \to 1$ in (3.25), so that $u_0 = 1$. Thus, looking at (3.28), the measurement datum ψ_0 is nothing else than q^* (up to a constant). Therefore, q^* could be easily determined when $\omega = 0$ since q^* is known on the boundary $\partial\Omega$. As we show in the following section, the analyticity of the problem with respect to ω allows to "transfer" this property to the desired range of frequencies $\mathcal{A}$.

3.4.3. Convergence of the Landweber Iteration. In order to use the well-posedness of the problem in $\omega = 0$ we shall need the following result on quantitative unique continuation for vector-valued holomorphic functions. It is an analogue of Lemma 3.4 for the infinite-dimensional setting.

LEMMA 3.11. *Let V be a complex Banach space, $\mathcal{A} = [K_{min}, K_{max}] \subset \mathbb{R}_+$, $C_0, D > 0$ and $g\colon B(0, K_{max}) \to V$ be holomorphic such that $\|g(0)\| \geq C_0$ and*

$$\sup_{\omega \in B(0,K_{max})} \|g(\omega)\| \leq D.$$

Then there exists $\omega \in \mathcal{A}$ such that

$$\|g(\omega)\| \geq C$$

for some $C > 0$ depending only on $\mathcal{A}$, C_0 and D.

PROOF. By contradiction, assume that there exists a sequence of holomorphic functions $g_n\colon B(0, K_{max}) \to V$ such that $\|g_n(0)\| \geq C_0$, $\sup_{\omega \in B(0,K_{max})} \|g_n(\omega)\| \leq D$ and $\max_{\omega \in \mathcal{A}} \|g_n(\omega)\| \to 0$. By Hahn Banach theorem, for any n there exists $T_n \in V'$ such that $\|T_n\| \leq 1$ and $T_n(g_n(0)) = \|g_n(0)\|$. Set $f_n := T_n \circ g_n\colon B(0, K_{max}) \to \mathbb{C}$. Thus (f_n) is a family of complex-valued uniformly bounded holomorphic functions, since

$$|f_n(\omega)| \leq \|T_n\| \, \|g_n(\omega)\| \leq D, \qquad \omega \in B(0, K_{max}).$$

As a consequence, by standard complex analysis, there exists a holomorphic function $f\colon B(0,K_{max}) \to \mathbb{C}$ such that $f_n \to f$ uniformly. We readily observe that for any $\omega \in \mathcal{A}$ there holds

$$|f(\omega)| = \lim_n |f_n(\omega)| \leq \lim_n \|T_n\| \, \|g_n(\omega)\| = 0,$$

since $\max_{\omega\in\mathcal{A}} \|g_n(\omega)\| \to 0$. By the unique continuation theorem $f(0) = 0$. On the other hand, as $T_n(g_n(0)) = \|g_n(0)\|$,

$$f(0) = \lim_n f_n(0) = \lim \|g_n(0)\| \geq C_0 > 0,$$

which yields a contradiction. □

In view of (3.32), we need to study the Fréchet differentiability of the map F_ω and characterize its derivative. Before doing this, we study the well-posedness of (3.25) with $q \in Q$. The result is classical, and the proof is left to the reader.

LEMMA 3.12. *Let $\Omega \subset \mathbb{R}^d$ be a bounded and smooth domain for $d = 2, 3$, $\omega \in B(0,K_{max})$ and $q \in Q$. For any $f \in L^2(\Omega;\mathbb{C})$ and $\varphi \in H^1(\Omega;\mathbb{C})$ the problem*

$$\begin{cases} \Delta u + \omega^2 q u = \omega f & \text{in } \Omega, \\ \frac{\partial u}{\partial \nu} - i\omega u = -i\omega\varphi & \text{on } \partial\Omega, \end{cases} \tag{3.33}$$

augmented with the condition

$$\int_{\partial\Omega} u \, d\sigma = \int_{\partial\Omega} \varphi \, d\sigma - i \int_\Omega f \, dx \tag{3.34}$$

if $\omega = 0$ admits a unique solution $u \in H^2(\Omega;\mathbb{C})$. Moreover

$$\|u\|_{H^2(\Omega;\mathbb{C})} \leq C\big(\|f\|_{L^2(\Omega;\mathbb{C})} + \|\varphi\|_{H^1(\Omega;\mathbb{C})}\big)$$

for some $C > 0$ depending only on Ω, Λ and K_{max}.

Since for $\omega = 0$ the solution to (3.33) is unique up to a constant, condition (3.34) is needed to have uniqueness. Even though it may seem mysterious, this condition is natural in order to ensure continuity of u with respect to ω. Indeed an integration by parts gives

$$\omega \int_\Omega f \, dx = \int_{\partial\Omega} \frac{\partial u}{\partial \nu} \, d\sigma + \omega^2 \int_\Omega q u \, dx = i\omega \int_{\partial\Omega} (u - \varphi) \, d\sigma + \omega^2 \int_\Omega q u \, dx,$$

whence for $\omega \neq 0$ we obtain

$$\int_{\partial\Omega} u \, d\sigma = \int_{\partial\Omega} \varphi \, d\sigma - i \int_\Omega f \, dx + \omega i \int_\Omega q u \, dx,$$

and so for $\omega = 0$ we are left with (3.34). The above condition is a consequence of (3.33) for $\omega \neq 0$, but needs to be added in the case $\omega = 0$ to guarantee uniqueness.

Let us go back to (3.25). Fix $\varphi \in H^1(\Omega;\mathbb{C})$ and $\omega \in B(0,K_{max})$. By Lemma 3.12 the problem

$$\begin{cases} \Delta u_\omega + \omega^2 q u_\omega = 0 \text{ in } \Omega, \\ \frac{\partial u_\omega}{\partial n} - i\omega u_\omega = -i\omega\varphi \text{ on } \partial\Omega, \end{cases} \tag{3.35}$$

together with condition

$$\int_{\partial\Omega} u_\omega \, d\sigma = \int_{\partial\Omega} \varphi \, d\sigma + \omega i \int_\Omega q u_\omega \, dx \tag{3.36}$$

admits a unique solution $u_\omega \in H^2(\Omega;\mathbb{C})$ such that

$$\|u_\omega\|_{H^2(\Omega;\mathbb{C})} \leq C \|\varphi\|_{H^1(\Omega;\mathbb{C})} \tag{3.37}$$

for some $C > 0$ depending only on Ω, Λ and K_{max}. As above, (3.36) guarantees uniqueness and continuity in $\omega = 0$ and is implicit in (3.35) if $\omega \neq 0$.

Next, we study the dependence of u_ω on ω.

LEMMA 3.13. *Let $\Omega \subset \mathbb{R}^d$ be a bounded and smooth domain for $d = 2, 3$, $q \in Q$ and $\varphi \in H^1(\Omega;\mathbb{C})$. The map*

$$\mathcal{F}(q)\colon B(0, K_{max}) \subset \mathbb{C} \longrightarrow H^2(\Omega;\mathbb{C}), \qquad \omega \longmapsto u_\omega$$

is holomorphic. Moreover, the derivative $\partial_\omega u_\omega \in H^2(\Omega;\mathbb{C})$ is the unique solution to

$$\begin{cases} \Delta \partial_\omega u_\omega + \omega^2 q \partial_\omega u_\omega = -2\omega q u_\omega \text{ in } \Omega, \\ \frac{\partial(\partial_\omega u_\omega)}{\partial \nu} - i\omega \partial_\omega u_\omega = i u_\omega - i\varphi \text{ on } \partial\Omega, \end{cases} \tag{3.38}$$

together with condition

$$\int_{\partial\Omega} \partial_\omega u_\omega \, d\sigma = \omega i \int_\Omega q \partial_\omega u_\omega \, dx + i \int_\Omega q u_\omega \, dx, \tag{3.39}$$

and satisfies

$$\|\partial_\omega u_\omega\|_{H^2(\Omega;\mathbb{C})} \leq C \|\varphi\|_{H^1(\Omega;\mathbb{C})}$$

for some $C > 0$ depending only on Ω, Λ and K_{max}.

PROOF. The proof of this result is completely analogous to the one given in Proposition 3.5 in a similar situation. Here only a sketch will be presented.

Fix $\omega \in B(0, K_{max})$: we shall prove that $\mathcal{F}(q)$ is holomorphic in ω and that the derivative is $\partial_\omega u_\omega$, i.e., the unique solution to (3.38)-(3.39). For $h \in \mathbb{C}$ let $v_h = (u_{\omega+h} - u_\omega)/h$. We need to prove that $v_h \to \partial_\omega u_\omega$ in $H^2(\Omega)$ as $h \to 0$. Suppose first $\omega \neq 0$. A direct calculation shows that

$$\begin{cases} \Delta v_h + \omega^2 q v_h = -2\omega q u_{\omega+h} - hq u_{\omega+h} \text{ in } \Omega, \\ \frac{\partial v_h}{\partial \nu} - i\omega v_h = i(u_{\omega+h} - \varphi) \text{ on } \partial\Omega. \end{cases}$$

Arguing as in Lemma 3.12, we obtain $u_{\omega+h} \to u_\omega$ as $h \to 0$ in $H^2(\Omega)$, whence $v_h \to \partial_\omega u_\omega$ in $H^2(\Omega)$, as desired.

When $\omega = 0$, the above system must be augmented with the condition

$$\int_{\partial\Omega} v_h \, d\sigma = i \int_\Omega q u_0 \, dx,$$

which is a simple consequence of (3.36), and the result follows. □

We now study the Fréchet differentiability of the map F_ω defined in (3.29). The proof of this result is close to the ones presented during the course, and the details are left to the reader.

LEMMA 3.14. *Let $\Omega \subset \mathbb{R}^d$ be a bounded and smooth domain for $d = 2, 3$, $q \in Q$, $\omega \in B(0, K_{max})$ and $\varphi \in H^1(\Omega;\mathbb{C})$. The map F_ω is Fréchet differentiable and for $\rho \in H_0^1(\Omega;\mathbb{R})$, the derivative $\xi_\omega(\rho) := DF_\omega[q](\rho)$ is the unique solution to the problem*

$$\begin{cases} \Delta \xi_\omega(\rho) = \operatorname{div}\left(|u_\omega|^2 \nabla\rho + (\overline{u}_\omega v_\omega(\rho) + u_\omega \overline{v}_\omega(\rho))\nabla q\right) \text{ in } \Omega, \\ \xi_\omega(\rho) = 0 \text{ on } \partial\Omega, \end{cases}$$

where $v_\omega(\rho) \in H^2(\Omega;\mathbb{C})$ is the unique solution to

$$\begin{cases} \Delta v_\omega(\rho) + \omega^2 q v_\omega(\rho) = -\omega^2 \rho\, u_\omega \text{ in } \Omega, \\ \frac{\partial v_\omega(\rho)}{\partial \nu} - i\omega v_\omega(\rho) = 0 \text{ on } \partial\Omega, \end{cases} \tag{3.40}$$

together with $\int_{\partial\Omega} v_0(\rho)\, d\sigma = 0$ if $\omega = 0$. In particular, F_ω is Lipschitz continuous, namely

$$\|\xi_\omega(\rho)\|_{H^1(\Omega;\mathbb{R})} \leq C(\Omega, \Lambda, K_{max}, \|\varphi\|_{H^1(\Omega;\mathbb{C})})\, \|\rho\|_{H^1(\Omega;\mathbb{R})}\,.$$

The main step in the proof of Theorem 3.10 is inequality (3.32), which we now prove. The argument in the proof clarifies the multi-frequency method illustrated in the previous section. The proof is structured as the proof of Theorem 3.3.

PROPOSITION 3.15. *Set $\varphi = 1$. There exist $C > 0$ and $m \in \mathbb{N}^*$ depending on Ω, Λ and $\mathcal{A}$ such that for any $q \in Q$ and $\rho \in H_0^1(\Omega;\mathbb{R})$*

$$\sum_{\omega \in K^{(m)}} \|DF_\omega[q](\rho)\|_{H^1(\Omega;\mathbb{R})} \geq C\, \|\rho\|_{H^1(\Omega;\mathbb{R})}.$$

PROOF. In the proof, several positive constants depending only on Ω, Λ and $\mathcal{A}$ will be denoted by C or Z.

Fix $q \in Q$. For $\rho \in H_0^1(\Omega;\mathbb{R})$ such that $\|\rho\|_{H^1(\Omega;\mathbb{R})} = 1$ define the map

$$g_\rho(\omega) = \operatorname{div}\left(u_\omega \overline{u}_{\overline{\omega}} \nabla\rho + (\overline{u}_{\overline{\omega}} v_\omega(\rho) + u_\omega \overline{v}_{\overline{\omega}}(\rho))\nabla q\right), \qquad \omega \in B(0, K_{max}).$$

Hence $g_\rho\colon B(0,K_{max}) \to H^{-1}(\Omega;\mathbb{C})$ is holomorphic[1]. We shall apply Lemma 3.11 to g_ρ, and so we now verify the hypotheses.

Since $\varphi = 1$, by (3.35)-(3.36) we have $u_0 = 1$ and by (3.40) we have $v_0(\rho) = 0$, whence $g_\rho(0) = \operatorname{div}(\nabla\rho)$. Since $\rho = 0$ on $\partial\Omega$ there holds

$$\left\|g_\rho(0)\right\|_{H^{-1}(\Omega;\mathbb{C})} = \|\operatorname{div}(\nabla\rho)\|_{H^{-1}(\Omega;\mathbb{C})} \geq C\, \|\nabla\rho\|_{L^2(\Omega)} \geq C > 0,$$

since $\|\rho\|_{H^1(\Omega;\mathbb{R})} = 1$. For $\omega \in B(0,K_{max})$ we readily derive

$$\begin{aligned} &\left\|g_\rho(\omega)\right\|_{H^{-1}(\Omega;\mathbb{C})} \leq C\, \|u_\omega \overline{u}_{\overline{\omega}} \nabla\rho + (\overline{u}_{\overline{\omega}} v_\omega(\rho) + u_\omega \overline{v}_{\overline{\omega}}(\rho))\nabla q\|_{L^2(\Omega)} \\ &\leq C\left(\|u_\omega\|_{L^\infty}\|u_{\overline{\omega}}\|_{L^\infty}\|\nabla\rho\|_{L^2} + (\|u_{\overline{\omega}}\|_{L^\infty}\|v_\omega(\rho)\|_{L^\infty} + \|u_\omega\|_{L^\infty}\|v_{\overline{\omega}}(\rho)\|_{L^\infty})\|\nabla q\|_{L^2}\right) \\ &\leq C\left(\|\rho\|_{H^1(\Omega)} + \|q\|_{H^1(\Omega)}\right) \\ &\leq C, \end{aligned}$$

where the third inequality follows from (3.37), Lemma 3.12 applied to $v_\omega(\rho)$ and the Sobolev embedding $H^2 \hookrightarrow L^\infty$. Therefore, by Lemma 3.11 there exists $\omega_\rho \in \mathcal{A}$ such that

$$\left\|g_\rho(\omega_\rho)\right\|_{H^{-1}(\Omega;\mathbb{C})} \geq C. \tag{3.41}$$

---

[1] Since, the map $F \in L^2(\Omega;\mathbb{C}^3) \mapsto \operatorname{div}(F) \in H^{-1}(\Omega;\mathbb{C})$ is linear and continuous, the holomorphicity of g_ρ follows from the holomorphicity of

$$\tilde{g}_\rho\colon B(0,K_{max}) \to L^2(\Omega;\mathbb{C}^3), \qquad \omega \mapsto u_\omega \overline{u}_{\overline{\omega}} \nabla\rho + (\overline{u}_{\overline{\omega}} v_\omega(\rho) + u_\omega \overline{v}_{\overline{\omega}}(\rho))\nabla q.$$

The fact that $\tilde{g}_\rho$ is holomorphic follows from the holomorphicity of $\omega \mapsto u_\omega$ (Lemma 3.13) and of $\omega \mapsto v_\omega$ (which follows as for u_ω), the elementary fact that products of holomorphic functions is holomorphic and the property that $\omega \mapsto \overline{f}(\overline{\omega})$ is holomorphic if $\omega \mapsto f(\omega)$ is holomorphic.

Consider now for $\omega \in B(0, K_{max})$

$$g'_\rho(\omega) = \operatorname{div}\Big((u'_\omega \overline{u}_{\overline{\omega}} + u_\omega \overline{u'}_{\overline{\omega}})\nabla\rho + (\overline{u'}_{\overline{\omega}} v_\omega(\rho) + \overline{u}_{\overline{\omega}} v'_\omega(\rho) + u'_\omega \overline{v}_{\overline{\omega}}(\rho) + u_\omega \overline{v'}_{\overline{\omega}}(\rho))\nabla q\Big)$$

where for simplicity the partial derivative ∂_ω is replaced by $'$. Arguing as before, and using Lemma 3.13 we obtain

$$\left\|g'_\rho(\omega)\right\|_{H^{-1}(\Omega;\mathbb{C})} \leq C, \qquad \omega \in B(0, K_{max}).$$

As a consequence, by (3.41) we obtain

$$\left\|g_\rho(\omega)\right\|_{H^{-1}(\Omega;\mathbb{C})} \geq C, \qquad \omega \in [\omega_\rho - Z, \omega_\rho + Z] \cap \mathcal{A}. \tag{3.42}$$

Since $\mathcal{A} = [K_{min}, K_{max}]$ there exists $P = P(Z, \mathcal{A}) \in \mathbb{N}$ such that

$$\mathcal{A} \subseteq \bigcup_{p=1}^{P} I_p, \qquad I_p = [K_{min} + (p-1)Z, K_{min} + pZ]. \tag{3.43}$$

Choose now $m \in \mathbb{N}^*$ big enough so that for every $p = 1, \dots, P$ there exists $i_p = 1, \dots, m$ such that $\omega(p) := \omega_{i_p}^{(m)} \in I_p$ (recall that $\omega_i^{(m)} = K_{min} + \frac{(i-1)}{(m-1)}(K_{max} - K_{min})$). Note that m depends only on Z and $|\mathcal{A}|$.

Since $\left|[\omega_\rho - Z, \omega_\rho + Z]\right| = 2Z$ and $\left|I_p\right| = Z$, in view of (3.43) there exists $p_\rho = 1, \dots, P$ such that $I_{p_\rho} \subseteq [\omega_\rho - Z, \omega_\rho + Z]$. Therefore $\omega(p_\rho) \in [\omega_\rho - Z, \omega_\rho + Z] \cap \mathcal{A}$, whence by (3.42) there holds $\left\|g_\rho(\omega(p_\rho))\right\|_{H^{-1}(\Omega;\mathbb{C})} \geq C$. Since $\omega(p_\rho) \in \mathbb{R}$ this implies

$$\left\|\operatorname{div}\Big(|u_{\omega(p_\rho)}|^2\nabla\rho + (\overline{u}_{\omega(p_\rho)} v_\omega(\rho) + u_\omega \overline{v}_{\omega(p_\rho)}(\rho))\nabla q\Big)\right\|_{H^{-1}(\Omega;\mathbb{C})} \geq C,$$

which by Lemma 3.14 yields $\left\|\operatorname{div}(\nabla \xi_{\omega(p_\rho)}(\rho))\right\|_{H^{-1}(\Omega;\mathbb{C})} = \left\|\Delta \xi_{\omega(p_\rho)}(\rho)\right\|_{H^{-1}(\Omega;\mathbb{C})} \geq C$. By the continuity of the map $F \in L^2(\Omega;\mathbb{C}^3) \mapsto \operatorname{div}(F) \in H^{-1}(\Omega;\mathbb{C})$, this implies $\left\|\nabla \xi_{\omega(p_\rho)}(\rho)\right\|_{L^2(\Omega;\mathbb{C}^3)} \geq C$. Hence, since $\xi_{\omega(p_\rho)}(\rho) = 0$ on $\partial\Omega$, by Poincaré's inequality there holds $\left\|\xi_{\omega(p_\rho)}(\rho)\right\|_{H^1(\Omega)} \geq C$. Thus, since $\omega(p_\rho) \in K^{(m)}$

$$\sum_{\omega \in K^{(m)}} \|\xi_\omega(\rho)\|_{H^1(\Omega)} \geq C.$$

We have proved this inequality only for $\rho \in H_0^1(\Omega;\mathbb{R})$ with unitary norm. By using the linearity of $\xi_\omega(\rho)$ with respect to ρ we immediately obtain

$$\sum_{\omega \in K^{(m)}} \|\xi_\omega(\rho)\|_{H^1(\Omega)} \geq C \|\rho\|_{H^1(\Omega)}, \qquad \rho \in H_0^1(\Omega;\mathbb{R}),$$

as desired. □

We are now ready to prove Theorem 3.10.

PROOF OF THEOREM 3.10. Inequality (3.32) follows from Proposition 3.15. Moreover, F_ω is Lipschitz continuous by Lemma 3.14. Therefore, the convergence of the Landweber iteration is a consequence of the results in the lecture notes, provided that $\|q_0 - q^*\|_{H^1(\Omega)}$ and h are small enough. □

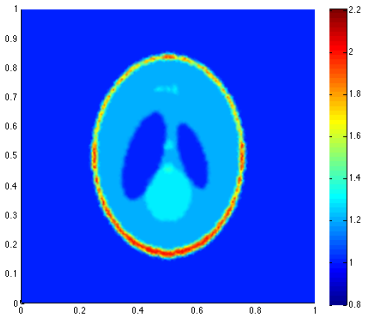

FIGURE 3.6. The true permittivity distribution q^*.

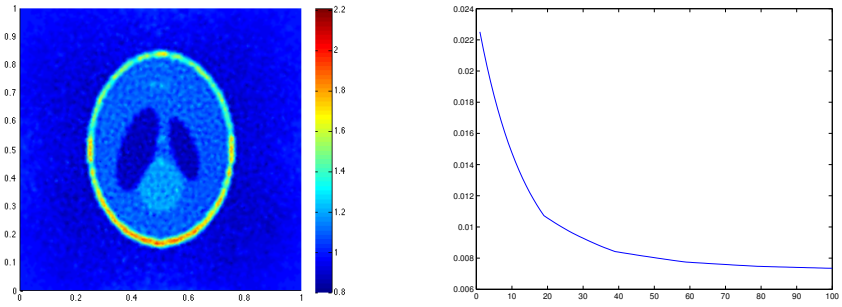

(A) Reconstructed distribution after 100 iterations.

(B) Relative error depending on the number of iterations.

FIGURE 3.7. Reconstruction of q for the set of frequencies $K = \{3\}$.

3.4.4. Numerical Results. In this section we present some numerical results. Let Ω be the unit square $[0,1] \times [0,1]$. We set the mesh size to be 0.01. A phantom image is used for the true permittivity distribution q^* (see Figure 3.6). According to Theorem 3.10 we set the Robin boundary condition to be a constant function $\varphi = 1$. Let K be the set of frequencies for which we have measurements ψ^*_ω, $\omega \in K$. As discussed in § 3.4.2.2, we minimize the functional J in (3.30) with the Landweber iteration scheme given in (3.31). The initial guess is $q_0 = 1$.

We start with the imaging problem at a single frequency. In Figure 3.7 we display the findings for the case $K = \{3\}$. Figure 3.7a shows the reconstructed distribution after 100 iterations. Figure 3.7b shows the relative error as a function of the number of iterations. This suggests the convergence of the iterative algorithm, even though the algorithm is proved to be convergent only in the multi-frequency case. It is possible that for small frequencies ω (with respect to the domain size) we are still in the coercive case, i.e. the kernel R_ω of $\rho \mapsto DF_\omega[q](\rho)$ is trivial and a single frequency is sufficient.

However, this does not work at higher frequencies (with respect to the domain size). Figure 3.8 shows some reconstructed maps for $\omega = 10$, $\omega = 15$ and $\omega = 20$,

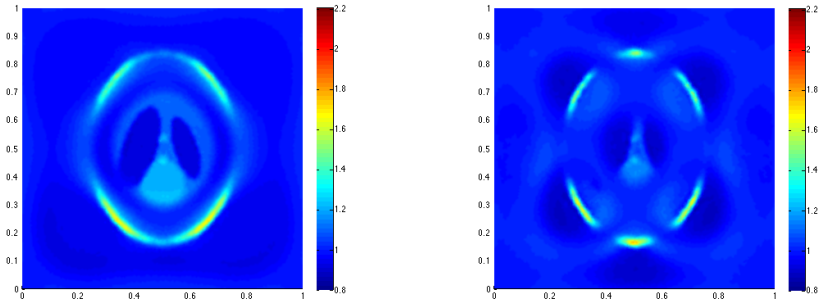

(A) $K = \{10\}$ (B) $K = \{15\}$

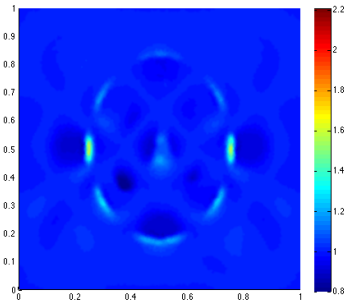

(C) $K = \{20\}$

FIGURE 3.8. Reconstruction of q for higher frequencies.

which suggest that the algorithm may not converge numerically for high frequencies. In each case, there are areas that remain invisible. This may be an indication that $R_\omega \neq \{0\}$ for these values of the frequency.

The invisible areas in Figure 3.8 are different for different frequencies, and so combining these measurements may give a satisfactory reconstruction. More precisely, according to Theorem 3.10, by using multiple frequencies it is possible to make the problem injective, namely $\cap_\omega R_\omega = \{0\}$, since the kernels R_ω change as ω varies. Figure 3.9 shows the results for the case $K = \{10, 15, 20\}$. (According to the notation introduced in Section 3.4.2, this choice of frequencies corresponds to $\mathcal{A} = [10, 20]$ and $m = 3$.) These findings suggest the convergence of the multi-frequency Landweber iteration, even though it was not convergent in each single-frequency case. Since we chose higher frequencies, the convergence is slower.

3.5. Full-Field Optical Coherence Elastography

3.5.1. Introduction. In this section, we provide a mathematical analysis of and a numerical framework for full-field optical coherence elastography, which has unique features including micron-scale resolution, real-time processing, and

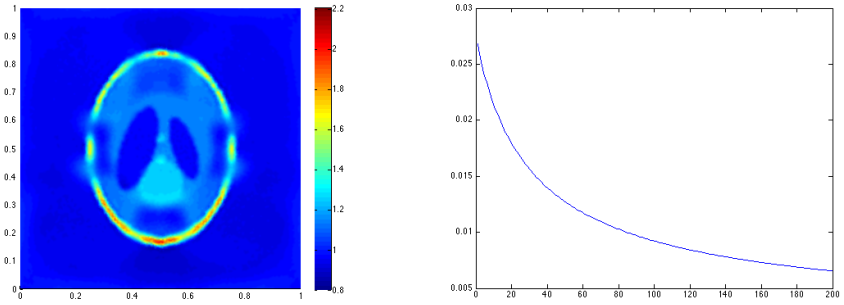

(A) Reconstructed distribution after 200 iterations.

(B) Relative error depending on the number of iterations.

FIGURE 3.9. Reconstruction of q for $K = \{10, 15, 20\}$.

non-invasive imaging. We present an algorithm for transforming volumetric optical images before and after the mechanical solicitation of a sample with sub-cellular resolution into quantitative shear modulus distributions.

Optical Coherence tomography (OCT) is a non-invasive and a non-ionizing imaging technique that produces high-resolution images of biological tissues. It performs optical slicing in the sample, to allow three-dimensional reconstructions of internal structures. Conventional optical coherence time-domain and frequency-domain tomographies require transverse scanning of the illumination spot in one or two directions to obtain cross-sectional or en face images, respectively.

Full-field OCT allows OCT to be performed without transverse scanning; the tomographic images are obtained by combining interferometric images acquired in parallel using an image sensor. Both the transverse and the axial resolutions are of the order of 1μm.

The idea is to register a volumetric optical image before and after mechanical solicitation of the sample. Based on the assumption that the density of the optical scatterers is advected by the deformation, the displacement map can be first estimated. Then, using a quasi-incompressible model for the tissue elasticity, the shear modulus distribution can be reconstructed from the estimated displacement map.

The OCT elastography is able to perform displacement measurements with sub-cellular resolution. It enables a more precise characterization of tissues than that achieved using ultrasound or magnetic resonance elastography; therefore, it provides a more accurate assessment of microscale variations of elastic properties. A map of mechanical properties added as a supplementary contrast mechanism to morphological images could aid diagnosis. The technique costs less than other elastography techniques.

In all of the aforementioned techniques, transforming the OCT images before and after the application of a load into quantitative maps of the shear modulus is a challenging problem.

In this section we present a mathematical and numerical framework for the OCT-elastography experiment. Using the set of images before and after mechanical solicitation we design a novel method to reconstruct the shear modulus distribution inside the sample.

To mathematically formulate the problem, let $\Omega_0 \subset \mathbb{R}^d, d = 2, 3$, and let ε_0 be the known piecewise smooth optical image of the medium, and μ be its shear modulus. In this chapter we consider heterogeneous (unknown) shear modulus distributions. The medium is solicited mechanically. Since compression modulus of biological media is four order of magnitude larger than the shear modulus, it can be shown that the displacement map u obeys the linearized equations of incompressible fluids or the Stokes system. The model problem is then the following Stokes system in a heteregeneous medium which reads:

$$\begin{cases} \nabla \cdot \left(\mu(\nabla u + \nabla u^T) \right) + \nabla p = 0 & \text{in } \Omega_0, \\ \nabla \cdot u = 0 & \text{in } \Omega_0, \\ u = f & \text{on } \partial\Omega_0, \end{cases} \tag{3.44}$$

where superposed the real-valued vector f satisfies the compatibility condition $\int_{\partial\Omega_0} f \cdot \nu = 0$ with ν being the outward normal at $\partial\Omega_0$.

Throughout this section, we assume that $\mu \in \mathcal{C}^{0,1}(\overline{\Omega}_0)$ and $f \in \mathcal{C}^2(\partial\Omega_0)^d$. It is known that (3.44) has a unique solution $u \in \mathcal{C}^1(\overline{\Omega_0})^d$. Moreover, there exists a positive constant C depending only on μ and Ω_0 such that

$$||u||_{\mathcal{C}^1(\overline{\Omega_0})^d} \leq C||f||_{\mathcal{C}^2(\partial\Omega_0)^d}.$$

Using a second OCT scan, one has access to the optical image of the deformed medium $\varepsilon_u(\widetilde{x})$, $\forall\ \widetilde{x} \in \Omega_u$, where Ω_u is defined by

$$\Omega_u = \{x + u(x),\ x \in \Omega_0\}.$$

The new optical image is linked to the original one by

$$\varepsilon(x) = \varepsilon_u\left(x + u(x)\right), \quad \forall\ x \in \Omega_0. \tag{3.45}$$

The goal is to reconstruct the shear modulus map μ on Ω_0 from the functions ε and ε_u. As it will be seen, in two dimensions if the direction of $\dfrac{\nabla\varepsilon}{|\nabla\varepsilon|}$ is not constant in a neighborhood of x, then the displacement field u at x can be approximately reconstructed. In three dimensions, one shall assume that the vectors $\dfrac{\nabla\varepsilon(y)}{|\nabla\varepsilon(y)|}$ are not coplanar for y a neighborhood of x. Hence, the reconstructed value of $u(x)$ serves as an initial guess for the minimization of the discrepancy between computed and measured changes in the optical image. Then, with a minimization scheme we can retrieve the shear modulus map from the reconstructed displacements. Note that reconstructing the displacement field from $\varepsilon - \varepsilon_u$ is a registration problem and its linearization is an optical flow problem. It is also worth mentioning that the approach developed in this section applies to other speckle imaging modalities.

3.5.2. Displacement Field Measurements.

3.5.2.1. *First-Order Approximation.* Let $\Omega \Subset (\Omega_0 \cap \Omega_u)$ be a smooth simply connected domain. On Ω, we have

$$\begin{aligned} \varepsilon_u = &\quad \varepsilon \circ (\mathbb{I} + u)^{-1} \\ \varepsilon = &\quad \varepsilon_u \circ (\mathbb{I} + u)\ , \end{aligned}$$

where $\mathbb{I}$ is the $d \times d$ identity matrix.

PROPOSITION 3.16. *Let $\varepsilon \in \mathrm{BV}(\Omega)$, the bounded variation functions, and let $u \in \mathcal{C}^1(\overline{\Omega})^d$ be such that $\|u\|_{\mathcal{C}^1(\overline{\Omega})^d} < 1$. Then, for any $\psi \in \mathcal{C}_0^1(\Omega)$, we have*

$$\left| \int_\Omega (\varepsilon - \varepsilon_u)\, \psi - \int_\Omega \psi u \cdot \nabla \varepsilon \right| \leq C \|u\|_{\mathcal{C}^0(\overline{\Omega})^d} \|u\|_{\mathcal{C}^1(\overline{\Omega})^d} \|\psi\|_{\mathcal{C}_0^1(\Omega)} |\varepsilon|_{\mathrm{TV}(\Omega)}\,, \tag{3.46}$$

where the constant C is independent of ψ and $|\ |_{\mathrm{TV}(\Omega)}$ denotes the total variation semi-norm. Estimate (3.46) yields that $\dfrac{\varepsilon_u - \varepsilon + u \cdot D\varepsilon}{\|u\|_{\mathcal{C}^0(\overline{\Omega})^d}}$ weakly converges to 0 in $\mathcal{C}_0^1(\Omega)$ when $\|u\|_{\mathcal{C}^1(\overline{\Omega})^d}$ goes to 0.

PROOF. For each $t \in [0,1]$, define φ_t by $\varphi_t^{-1}(x) = x + tu(x)$. Let $\eta > 0$ be a small parameter, and $\varepsilon^{(\eta)}$ be a smooth function such that $\|\varepsilon - \varepsilon^{(\eta)}\|_{L^1(\Omega)} \to 0$, and $|\varepsilon^{(\eta)}|_{\mathrm{TV}(\Omega)} \to |\varepsilon|_{\mathrm{TV}(\Omega)}$ as $\eta \to 0$. Analogously, we define $\varepsilon_u^{(\eta)}$ to be the smooth approximation of ε_u given by

$$\varepsilon_u^{(\eta)}(x) = \varepsilon^{(\eta)} \circ \varphi_1(x)\,.$$

From

$$\varepsilon_u^{(\eta)}(x) - \varepsilon^{(\eta)}(x) = \left(\varepsilon^{(\eta)} \circ \varphi_1\right)(x) - \left(\varepsilon^{(\eta)} \circ \varphi_0\right)(x), \quad \forall\, x \in \Omega\,,$$

we have

$$\varepsilon_u^{(\eta)}(x) - \varepsilon^{(\eta)}(x) = \int_0^1 \nabla \varepsilon^{(\eta)}(\varphi_t(x)) \cdot \partial_t \varphi_t(x) dt, \quad \forall\, x \in \Omega\,.$$

Therefore, for $\psi \in \mathcal{C}_0^\infty(\Omega)$ with $\mathcal{C}_0^\infty(\Omega)$ being the set of compactly supported $\mathcal{C}^\infty$ functions,

$$\int_\Omega \left[\varepsilon_u^{(\eta)}(x) - \varepsilon^{(\eta)}(x) + \nabla \varepsilon^{(\eta)}(x) \cdot u(x)\right] \psi(x) dx = \tag{3.47}$$

$$\int_\Omega \left[\int_0^1 \nabla \varepsilon^{(\eta)}(\varphi_t(x)) \cdot \partial_t \varphi_t(x) dt\right] \psi(x) dx + \int_\Omega \nabla \varepsilon^{(\eta)}(x) \cdot u(x) \psi(x) dx, \quad \forall\, x \in \Omega\,.$$

By a change of variables in the first integral and using the fact that

$$\partial_t \varphi_t(x) = -\partial_x \varphi_t(x) \partial_t \varphi_t^{-1}(y)|_{y=\varphi_t(x)},$$

we get, for all $x \in \Omega$,

$$\begin{aligned} &\int_0^1 \left[\int_\Omega \nabla \varepsilon^{(\eta)}(\varphi_t(x)) \cdot \partial_t \varphi_t(x) \psi(x) dx\right] dt = \\ &- \int_0^1 \int_\Omega \nabla \varepsilon^{(\eta)}(y) \cdot \left[\partial_x \varphi_t(\varphi_t^{-1}(y)) \partial_t \varphi_t^{-1}(y)\right] |\det \partial_x \varphi_t^{-1}(y)| \psi\left(\varphi_t^{-1}(y)\right) dy dt\,. \end{aligned}$$

Here, det denotes the determinant of a matrix. Since

$$\forall\ (y,t) \in \Omega \times [0,1], \quad \partial_t \varphi_t^{-1}(y) = u(y),$$
$$\partial_y \varphi_t^{-1}(y) = \mathbb{I} + t\nabla u(y),$$

and

$$\partial_x \varphi_t(\varphi_t^{-1}(y)) \partial_y \varphi_t^{-1}(y) = \mathbb{I}\,,$$

we can write

$$\int_0^1 \int_\Omega \left[\nabla \varepsilon^{(\eta)}(\varphi_t(x)) \cdot \partial_t \varphi_t(x) \psi(x) dx\right] dt =$$
$$-\int_0^1 \int_\Omega \nabla \varepsilon^{(\eta)}(y) \cdot \left[\left(\mathbb{I} + t\nabla u(y)\right)^{-1} u(y)\right] |\det \mathbb{I} + t\nabla u(y)| \psi\left(\varphi_t^{-1}(y)\right) dy dt\,,$$

and hence,

$$\int_\Omega \left[\varepsilon_u^{(\eta)}(x) - \varepsilon^{(\eta)}(x) + \nabla \varepsilon^{(\eta)}(x) \cdot u(x)\right] \psi(x) dx = \tag{3.48}$$
$$\int_0^1 \int_\Omega \nabla \varepsilon^{(\eta)}(x) \cdot u(x) \left[\psi(x) - \psi\left(\varphi_t^{-1}(x)\right)\right] dx dt$$
$$+ \int_0^1 \int_\Omega \nabla \varepsilon^{(\eta)}(x) \cdot \left(\left[\left(\mathbb{I} + t\nabla u(x)\right)^{-1} |\det \mathbb{I} + t\nabla u(x)| - \mathbb{I}\right] u(x)\right) \psi\left(\varphi_t^{-1}(x)\right) dx dt\,.$$

The first term in the right-hand side of (3.48) can be estimated as follows:

$$\left|\int_0^1 \int_\Omega \nabla \varepsilon^{(\eta)}(x) \cdot u(x) \left[\psi(x) - \psi\left(\varphi_t^{-1}(x)\right)\right] dx dt\right| \leq \|u\|^2_{\mathcal{C}^0(\overline{\Omega})^d} \|\nabla \varepsilon^{(\eta)}\|_{L^1(\Omega)^d} \|\nabla \psi\|_{\mathcal{C}^0(\Omega)^d}\,.$$

Let tr denote the trace of a matrix. Using the fact that

$$\left(\mathbb{I} + t\nabla u\right)^{-1} = \sum_{i=0} (-1)^i \left(t\nabla u\right)^i\,,$$

which follows from $||u||_{\mathcal{C}^1(\Omega)^d} < 1$, and

$$\det\ (\mathbb{I} + t\nabla u) = \begin{cases} 1 - \operatorname{tr} t\nabla u + \det t\nabla u & \text{if } d = 2\,, \\ 1 + \operatorname{tr} t\nabla u - \dfrac{1}{2}\left[(\operatorname{tr} t\nabla u)^2 - \operatorname{tr}\ (t\nabla u)^2\right] + \det t\nabla u & \text{if } d = 3\,, \end{cases}$$

we get

$$\int_0^1 \int_\Omega \nabla \varepsilon^{(\eta)}(x) \cdot u(x) \left[\left(\mathbb{I} + t\nabla u(x)\right)^{-1} |\det \mathbb{I} + t\nabla u(x)| - \mathbb{I}\right] \psi\left(\varphi_t^{-1}(x)\right) dx dt$$
$$\leq \|u\|_{\mathcal{C}^0(\overline{\Omega})^d} \|u\|_{\mathcal{C}^1(\overline{\Omega})^d} \|\nabla \varepsilon^{(\eta)}\|_{L^1(\Omega)^d} \|\psi\|_{\mathcal{C}^0(\Omega)}\,,$$

which is the desired estimate for the second term in the right-hand side of (3.48).

Now, we can deduce the final result by density when $\eta \to 0$. Since $u \in \mathcal{C}^1(\Omega)^d$ and $\psi \in \mathcal{C}_0^1(\Omega)$, we can write

$$\int_\Omega \psi u \cdot \nabla \varepsilon^{(\eta)} = -\int_\Omega \nabla \cdot (\psi u) \varepsilon^{(\eta)}.$$

Since $\|\varepsilon^{(\eta)} - \varepsilon\|_{L^1(\Omega)} \to 0$, we have

$$\int_\Omega \nabla \cdot (\psi u) \varepsilon^{(\eta)} \to \int_\Omega \nabla \cdot (\psi u) \varepsilon\,.$$

As $|\varepsilon^{(\eta)}|_{\mathrm{TV}(\Omega)} \to |\varepsilon|_{\mathrm{TV}(\Omega)}$, we arrive at (3.46) and the proof of the proposition is complete. □

3.5.2.2. *Local Recovery Via Linearization.* For simplicity we will assume ε is smooth, thus differentiable. The data consists of ε and ε_u on Ω. In order to reconstruct u, we can use the first order approximation of $\varepsilon - \varepsilon_u$:

$$\varepsilon - \varepsilon_u \approx u \cdot \nabla \varepsilon,$$

given by Proposition 3.16. We will denote the measurement data $\varepsilon - \varepsilon_u$ as $D(x), x \in \Omega$.

Let w be a mollifier supported on $[-1, 1]$. For any $\delta > 0$, we define

$$w_\delta = \frac{1}{\delta^d} w\left(\frac{\cdot}{\delta}\right),$$

and introduce

$$u_\delta(x) = \int_\Omega u(y) w_\delta(|x-y|) dy.$$

Since u is smooth, for any $x \in \Omega$, $u_\delta(x)$ is a good approximation of u on the ball with center x and radius δ.

We want to find an approximate value for u_δ from the optical measurements and use it as an initial guess in an optimization procedure. For doing so, we introduce the functional $J_x : \mathbb{R}^d \longrightarrow \mathbb{R}$ given by

$$u \longmapsto J_x(u) = \int_\Omega |\nabla \varepsilon(y) \cdot u - D(y)|^2 w_\delta(|x-y|) dy\,,$$

and look for minimizers of J_x in $\mathbb{R}^d$. The gradient of J_x can be explicitly computed as follows:

$$\nabla J_x(u) = 2 \int_\Omega \left(\nabla \varepsilon(y) \cdot u - D(y)\right) \nabla \varepsilon(y) w_\delta(|x-y|) dy\,.$$

J_x is a quadratic functional and we have

$$\nabla J_x(u) = 0 \tag{3.49}$$

if and only if

$$\left(\int_\Omega w_\delta(|x-y|) \nabla \varepsilon(y) \nabla \varepsilon^T(y) dy\right) u = \int_{x+\delta B} D(y) w_\delta(|x-y|) \nabla \varepsilon(y) dy\,, \tag{3.50}$$

where B is the ball with center 0 and radius 1.

If the matrix $\displaystyle\int_\Omega w_\delta(|x-y|) \nabla \varepsilon(y) \nabla \varepsilon^T(y)$ is invertible, then the minimizer is given by

$$u^{=} \left(\int_\Omega w_\delta(|x-y|) \nabla \varepsilon(y) \nabla \varepsilon^T(y) dy\right)^{-1} \int_{x+\delta B} D(y) w_\delta(|x-y|) \nabla \varepsilon(y) dy\,. \tag{3.51}$$

The following proposition gives a sufficient condition for the invertibilty of the matrix $\displaystyle\int_\Omega w_\delta(|x-y|) \nabla \varepsilon(y) \nabla \varepsilon^T(y)$.

PROPOSITION 3.17. *Suppose that ε has no jumps and $d = 2$. Assume $x + \delta B \subset \Omega$. Then, if there is an positive measure set contained in $\nabla\varepsilon$ in $\{y \,:\, w_\delta(|y-x|) \neq 0\}$ where all vectors are not collinear, then the matrix*

$$\int_\Omega w_\delta(|x-y|)\nabla\varepsilon(y)\nabla\varepsilon^T(y)dy$$

is invertible.

PROOF. Writing

$$\forall\, y \in x + \delta B, \quad \nabla\varepsilon(y) = u(y)e_1 + v(y)e_2,$$

where $\{e_1, e_2\}$ is the cannonical basis of $\mathbb{R}^2$, it follows that

$$\nabla\varepsilon\nabla\varepsilon^T(y) = u^2(y)e_1e_1^T + v^2(y)e_2e_2^T + u(y)v(y)\left(e_1e_2^T + e_2e_1^T\right), \quad \forall\, y \in x + \delta B\,.$$

Computing the convolution with respect to w_δ, we get

$$\int_\Omega w_\delta(|y-y|)\nabla\varepsilon(y)\nabla\varepsilon^T(y)dy = \left(\int_\Omega u^2(y)w_\delta(|y-x|)dy\right)e_1e_1^T$$
$$+\left(\int_\Omega v^2(y)w_\delta(|y-x|)dy\right)e_2e_2^T + \left(\int_\Omega u(y)v(y)w_\delta^T(|y-x|)dy\right)\left(e_1e_2^T + e_2e_1^T\right).$$

Using the determinant, this matrix is not invertible if and only if

$$\left(\int_\Omega u^2(y)w_\delta(|y-x|)dy\right)\left(\int_\Omega v^2(y)w_\delta(|y-x|)dy\right) = \left(\int_\Omega u(y)v(y)w_\delta(|y-x|)dy\right)^2,$$

which is exactly the equality case in weighted Cauchy-Schwarz inequality. So, if there exist a positive measure set where u is not proportional to v, it is equivalent to not have all vectors in the set collinear , and hence the matrix is invertible. □

REMARK 3.18. Assuming that $\nabla\varepsilon(y) \neq 0$ for $y \in x + \delta B \subset \Omega$, Proposition 3.17 gives that the direction of $\dfrac{\nabla\varepsilon}{|\nabla\varepsilon|}$ in not constant in $x + \delta B \subset \Omega$ if and only if

$$\int_{x+\delta B} \nabla\varepsilon(y)\nabla\varepsilon^T(y)dy \quad \text{is invertible.}$$

Hence, under the above condition on ε in the neighborhood $x + \delta B$, the displacement field u at x can be approximately reconstructed.

REMARK 3.19. By exactly the same arguments as those in two dimensions, one can prove that in the three-dimensional case, if all vectors $\nabla\varepsilon$ in $\{y \,:\, w_\delta(|y-x|) \neq 0\}$ are not coplanar, then the matrix

$$\int_\Omega w_\delta(|x-y|)\nabla\varepsilon(y)\nabla\varepsilon^T(y)dy$$

is invertible.

On the other hand, in the case where ε is piecewise smooth, one can first detect the surface of jumps of ε using for example an edge detection algorithm and then apply the proposed local algorithm in order to have a good approximation of u in the domains where ε is smooth.

3.5.2.3. *Minimization of the Discrepancy Functional.* This step was omitted, as it required subdifferential calculus and various steps. The main idea is the one used already in many lectures, that corresponds to minimize the discrepancy functional using (3.51) as first guess. With the reconstructed displacement map we now seek to reconstruct the shear modulus.

3.5.3. Reconstruction of the Shear Modulus. The problem is now to recover the function μ the reconstructed internal data u. We introduce the operator $\mathcal{F}$

$$u = \mathcal{F}[\mu] = \begin{cases} \nabla \cdot \Big(\mu(\nabla u + \nabla u^T)\Big) + \nabla p = 0 & \text{in } \Omega_0\,, \\ \nabla \cdot u = 0 & \text{in } \Omega_0\,, \\ u = f & \text{on } \partial\Omega_0\,, \end{cases}$$

and minimize the function $\mathcal{K}$ given by

$$\begin{aligned} \mathcal{C}^{0,1}(\overline{\Omega_0}) &\longrightarrow \mathbb{R} \\ \mu &\longmapsto \mathcal{K}[\mu] = \int_\Omega |\mathcal{F}[\mu] - u|^2\, dx\,. \end{aligned}$$

$\mathcal{K}$ is Fréchet differentiable and its gradient can be explicitly computed. Let v be the solution of

$$\begin{cases} \nabla \cdot \Big(\mu(\nabla v + \nabla v^T)\Big) + \nabla q = (\mathcal{F}[\mu] - u) & \text{in } \Omega_0\,, \\ \nabla \cdot v = 0 & \text{in } \Omega_0\,, \\ v = 0 & \text{on } \partial\Omega_0\,. \end{cases}$$

Then,

$$\nabla\mathcal{K}(\mu)[h] = \int_{\Omega_0} h(\nabla v + \nabla v^T) : (\nabla u + \nabla u^T)\, dx\,.$$

A gradient descent method can be applied in order to reconstruct μ from u.

3.5.4. Numerical Illustrations. We take $\Omega = [0,1]^2$ and discretize it on a 300×300 grid, and generate a random Gaussian process to model the optical image ε of the medium as shown in Figure 3.10. Given a shear modulus μ map on Ω; see Figure 3.14 (left), we solve (3.44) on Ω via a finite element method compute the displacement field u. We then compute the displaced optical image ε_u by using a spline interpolation approach and proceed to recover the shear modulus from the data ε and ε_u on the grid by the method described in this chapter.

Using (3.51), we first compute the initial guess u_δ for the displacement field as the least-square solution to minimization of J_x. Figure 3.11 shows the kernel w_δ used to compute u_δ. As one can see δ needs to be large enough so the matrix $w_\delta \star \left(\nabla\varepsilon\nabla\varepsilon^T\right)$ is invertible at each point x, which is basically saying that δ must be bigger than the correlation length of ε. Figure 3.12 shows the conditioning of the matrix $w_\delta \star \left(\nabla\varepsilon\nabla\varepsilon^T\right)$. Figure 3.13 shows the true displacement u^*, the result of the first order approximation (*i.e.*, the initial guess) u_δ and then the result of the optimization process using a gradient descent method to minimize the discrepancy functional I.

Once the displacement inside the domain is reconstructed, we can recover the shear modulus μ, as shown in Figure 3.14. We reconstruct μ by minimizing the functional $\mathcal{K}$ and using a gradient descent-type method. Note that gradient of $\mathcal{K}$ is computed with the adjoint state method, described previously. As it can be

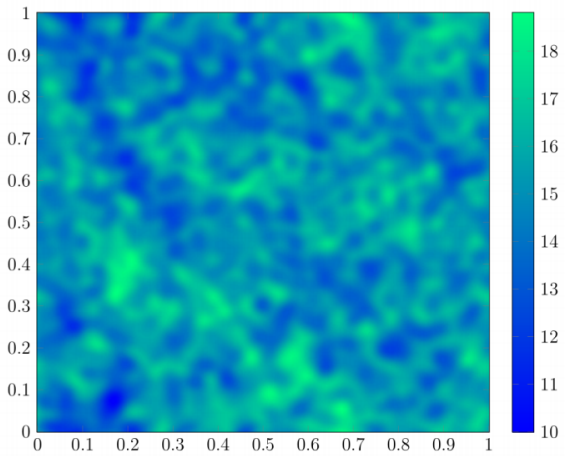

FIGURE 3.10. Optical image ε of the medium.

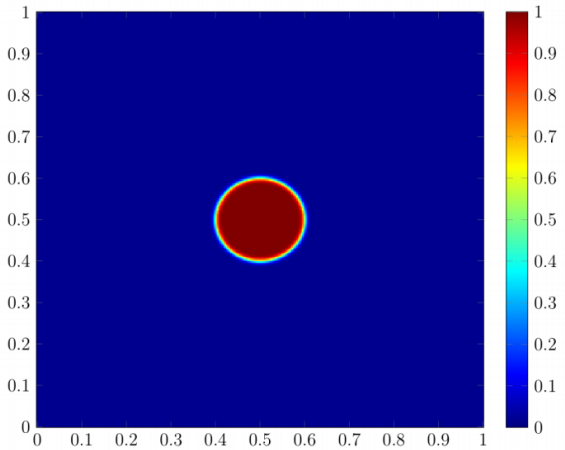

FIGURE 3.11. Averaging kernel w_δ.

seen in Figure 3.14, the reconstruction is very accurate but not so perfect on the boundaries of Ω, which is due to the poor estimation of u on $\partial\Omega$.

3.5.5. Concluding Remarks. In this chapter, we developed a novel algorithm which gives access not only to stiffness quantitative information of biological tissues but also opens the way to other contrasts such as mechanical anisotropy. In the heart, the muscle fibers have anisotropic mechanical properties. It would be very interesting to detect a change in fiber orientation using OCT elastographic tomography.

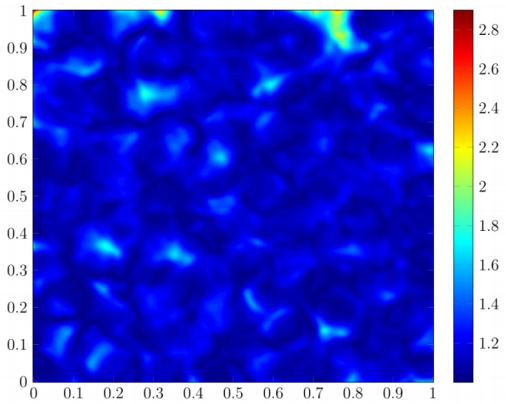

FIGURE 3.12. Conditioning of the matrix $w_\delta \star \nabla\varepsilon\nabla\varepsilon^T$.

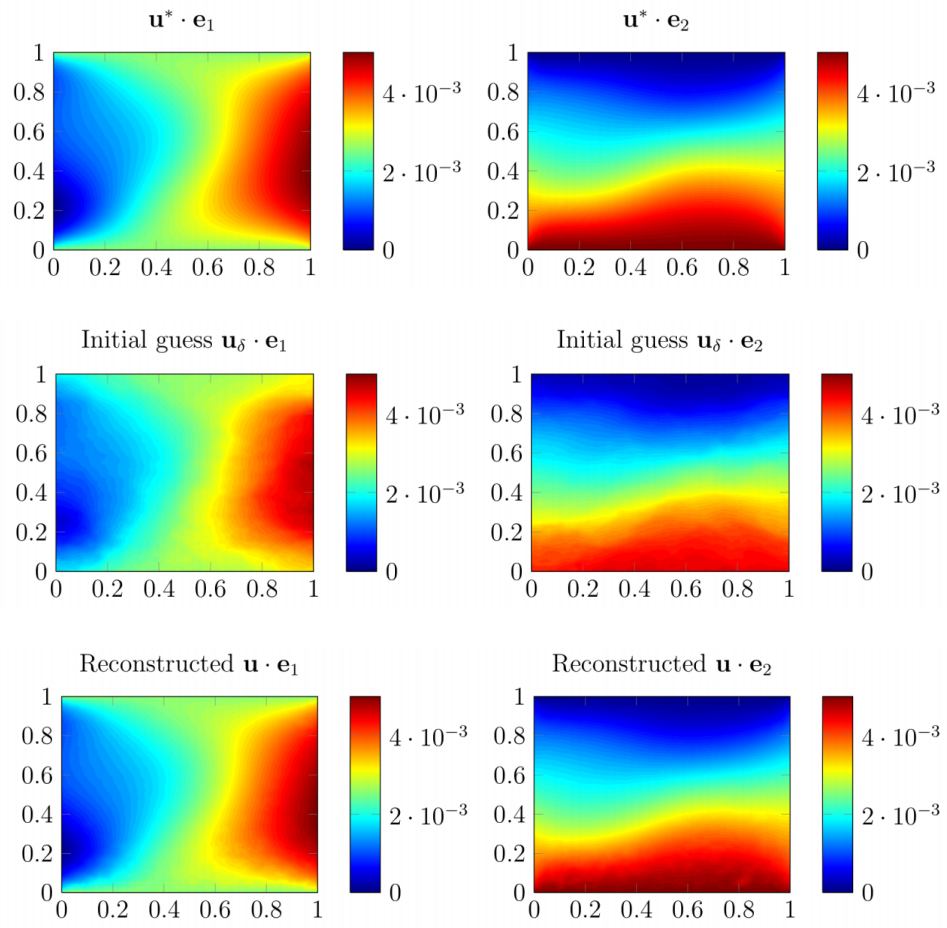

FIGURE 3.13. Displacement field and its reconstruction.

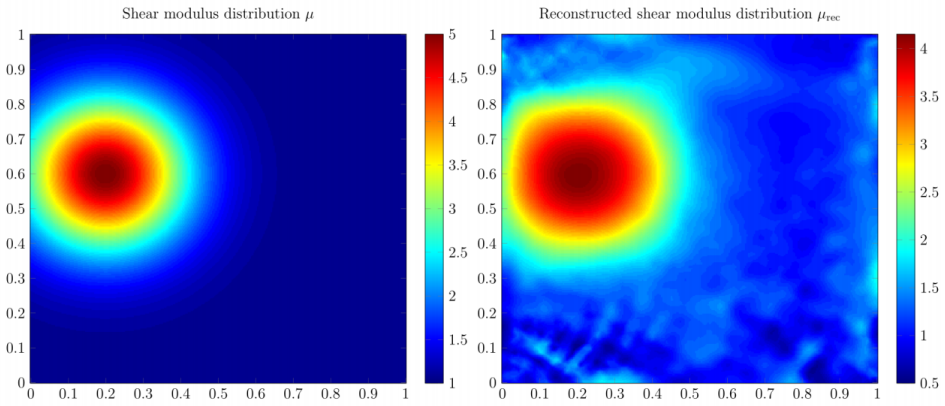

FIGURE 3.14. Shear modulus reconstruction.

CHAPTER 4

Effective Electrical Tissue Properties and Nanoparticle Imaging

4.1. Effective Electrical Tissue Properties

4.1.1. Introduction. This chapter aims at analytically exhibiting the fundamental mechanisms underlying the fact that effective biological tissue electrical properties and their frequency dependence reflect the tissue composition and physiology. For doing so, a homogenization theory is derived to describe the effective admittivity of cell suspensions. A formula is reported for dilute cases that gives the frequency-dependent effective admittivity with respect to the membrane polarization. Different microstructures are shown to be distinguishable via spectroscopic measurements of the overall admittivity using the spectral properties of the membrane polarization. The Debye relaxation times associated with the membrane polarization tensor are shown to be able to give the microscopic structure of the medium. A natural measure of the admittivity anisotropy is introduced and its dependence on the frequency of applied current is derived. A Maxwell-Wagner-Fricke formula is given for concentric circular cells.

The electric behavior of biological tissue under the influence of an electric field at frequency ω can be characterized by its frequency-dependent effective admittivity $k_{ef} := \sigma_{ef}(\omega) + i\omega\varepsilon_{ef}(\omega)$, where σ_{ef} and ε_{ef} are respectively its effective conductivity and permittivity. Electrical impedance spectroscopy assesses the frequency dependence of the effective admittivity by measuring it across a range of frequencies from a few Hz to hundreds of MHz. Effective admittivity of biological tissues and its frequency dependence vary with tissue composition, membrane characteristics, intra-and extra-cellular fluids and other factors. Hence, the admittance spectroscopy provides information about the microscopic structure of the medium and physiological and pathological conditions of the tissue.

In this chapter, we consider a periodic suspension of identical cells of arbitrary shape. We apply at the boundary of the medium an electric field of frequency ω. The medium outside the cells has an admittivity of $k_0 := \sigma_0 + i\omega\varepsilon_0$. Each cell is composed of an isotropic homogeneous core of admittivity k_0 and a thin membrane of constant thickness δ and admittivity $k_m := \sigma_m + i\omega\varepsilon_m$. The thickness δ is considered to be very small relative to the typical cell size and the membrane is considered very resistive, *i.e.*, $\sigma_m \ll \sigma_0$. In this context, the potential in the medium passes an effective discontinuity over the cell boundary; the jump is proportional to its normal derivative with a coefficient of the effective thickness, given by $\delta k_0 / k_m$. The normal derivative of the potential is continuous across the cell boundaries.

We use homogenization techniques with asymptotic expansions to derive a homogenized problem and to define an effective admittivity of the medium. We

prove a rigorous convergence of the original problem to the homogenized problem via two-scale convergence. For dilute cell suspensions, we use layer potential techniques to expand the effective admittivity in terms of cell volume fraction. Through the effective thickness, $\delta\, k_0/k_m$, the first-order term in this expansion can be expressed in terms of a membrane polarization tensor, M, that depends on the operating frequency ω. We retrieve the Maxwell-Wagner-Fricke formula for concentric circular-shaped cells.

The imaginary part of M is positive for δ small enough. Its two eigenvalues are maximal for frequencies $1/\tau_i, i = 1, 2$, of order of a few MHz with physically plausible parameters values. This dispersion phenomenon well known by the biologists is referred to as the β-dispersion. The associated characteristic times τ_i correspond to Debye relaxation times. Given this, we show that different microscopic organizations of the medium can be distinguished via $\tau_i, i = 1, 2$, alone. The relaxation times τ_i are computed numerically for different configurations: one circular or elliptic cell, two or three cells in close proximity. The obtained results illustrate the viability of imaging cell suspensions using the spectral properties of the membrane polarization. The Debye relaxation times are shown to be able to give the microscopic structure of the medium.

The chapter is organized as follows. Section 4.1.2 introduces the problem settings and state our main results. In section 4.1.3 we consider the problem of determining the effective property of a suspension of cells when the volume fraction goes to zero. In section 4.1.4 we provide numerical examples that support our findings. A few concluding remarks are given in the last section. For simplicity, we only treat the two-dimensional case.

4.1.2. Problem Settings and Main Results. The aim of this section is to introduce the problem settings and state the main results of this chapter.

4.1.2.1. *Periodic Domain.* We consider the probe domain Ω to be a bounded open set of $\mathbb{R}^2$ of class $\mathcal{C}^2$. The domain contains a periodic array of cells whose size is controlled by ε. Let C be a $\mathcal{C}^{2,\eta}$ domain being contained in the unit square $Y = [0,1]^2$, see Figure 4.1. Here, $0 < \eta < 1$ and C represents a reference cell. We divide the domain Ω periodically in each direction in identical squares $(Y_{\varepsilon,n})_n$ of size ε, where

$$Y_{\varepsilon,n} = \varepsilon n + \varepsilon Y\,.$$

Here, $n \in N_\varepsilon := \left\{ n \in \mathbb{Z}^2 : Y_{\varepsilon,n} \cap \Omega \neq \emptyset \right\}$.

We consider that a cell $C_{\varepsilon,n}$ lives in each small square $Y_{\varepsilon,n}$. As shown in Figure 4.4, all cells are identical, up to a translation and scaling of size ε, to the reference cell C:

$$\forall n \in N_\varepsilon, \quad C_{\varepsilon,n} = \varepsilon n + \varepsilon\, C\,.$$

So are their boundaries $(\Gamma_{\varepsilon,n})_{n\in N_\varepsilon}$ to the boundary Γ of C:

$$\forall n \in N_\varepsilon, \quad \Gamma_{\varepsilon,n} = \varepsilon n + \varepsilon\, \Gamma\,.$$

Let us also assume that all the cells are strictly contained in Ω, that is for every $n \in N_\varepsilon$, the boundary $\Gamma_{\varepsilon,n}$ of the cell $C_{\varepsilon,n}$ does not intersect the boundary $\partial\Omega$:

$$\partial\Omega \cap \Big(\bigcup_{n\in N_\varepsilon} \Gamma_{\varepsilon,n} \Big) = \emptyset.$$

4.1.2.2. *Electrical Model of the Cell.* In this section we consider the reference cell C immersed in a domain D. We apply a sinusoidal electrical current $g \in L^2_0(\partial D)$ with angular frequency ω at the boundary of D.

The medium outside the cell, $D \setminus \overline{C}$, is a homogeneous isotropic medium with admittivity $k_0 := \sigma_0 + i\omega\varepsilon_0$. The cell C is composed of an isotropic homogeneous core of admittivity k_0 and a thin membrane of constant thickness δ with admittivity $k_m := \sigma_m + i\omega\varepsilon_m$. We make the following assumptions :

$$\sigma_0 > 0, \sigma_m > 0, \varepsilon_0 > 0, \varepsilon_m \geq 0\,.$$

If we apply a sinusoidal current $g(x)\sin(\omega t)$ on the boundary ∂D in the low frequency range below 10 MHz, the resulting complex-valued time harmonic potential $\check{u}$ is governed by

$$\begin{cases} \nabla \cdot (k_0 + (k_m - k_0)\chi(\Gamma^\delta))\nabla \check{u}) = 0 & \text{in } D\,, \\ k_0 \dfrac{\partial \check{u}}{\partial \nu} = g & \text{on } \partial D\,, \end{cases}$$

where $\Gamma^\delta := \{x \in C \ : \ \mathrm{dist}(x, \Gamma) < \delta\}$ and $\chi(\Gamma^\delta)$ is the characteristic function of the set Γ^δ.

The membrane thickness δ is considered to be very small compared to the typical size ρ of the cell, *i.e.*, $\delta/\rho \ll 1$. According to the transmission condition, the normal component of the current density $k_0 \dfrac{\partial \check{u}}{\partial \nu}$ can be approximately regarded as continuous across the thin membrane Γ.

We set $\beta := \dfrac{\delta}{k_m}$. Since the membrane is very resistive, *i.e.*, $\sigma_m/\sigma_0 \ll 1$, the potential $\check{u}$ in D undergoes a jump across the cell membrane Γ, which can be approximated at first order by $\beta k_0 \dfrac{\partial \check{u}}{\partial \nu}$.

More precisely, we approximate $\check{u}$ by u defined as the solution of the following equations:

$$\text{(4.1)} \qquad \begin{cases} \nabla \cdot k_0 \nabla u = 0 & \text{in } D \setminus \overline{C}\,, \\ \nabla \cdot k_m \nabla u = 0 & \text{in } C\,, \\ k_0 \dfrac{\partial u}{\partial \nu}\Big|_+ = k_m \dfrac{\partial u}{\partial \nu}\Big|_- & \text{on } \Gamma\,, \\ u|_+ - u|_- - \beta k_m \dfrac{\partial u}{\partial \nu} = 0 & \text{on } \Gamma\,, \\ k_0 \dfrac{\partial u}{\partial \nu}\Big|_{\partial D} = g, \quad \displaystyle\int_{\partial D} g(x) ds(x) = 0, \quad \int_{D\setminus\overline{C}} u(x)dx = 0\,. \end{cases}$$

Equation (4.1) is the starting point of our analysis.

For any open set B in $\mathbb{R}^2$, we denote $\widetilde{W}^{1,2}(B)$ the Sobolev space $W^{1,2}(B)/\mathbb{C}$, which can be represented as

$$\widetilde{W}^{1,2}(B) = \left\{ u \in W^{1,2}(B) : \int_B u(x)dx = 0 \right\}.$$

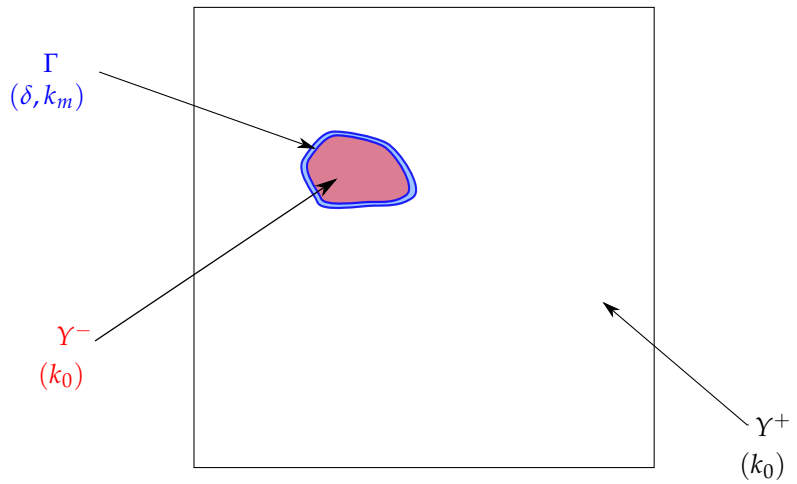

FIGURE 4.1. *Schematic illustration of a unit period Y.*

Let $D^+ = D \setminus \overline{C}$ and $D^- = C$. The following result holds.

LEMMA 4.1. *There exists a unique solution* $u := (u^+, u^-)$ *in* $\widetilde{W}^{1,2}(D^+) \times W^{1,2}(D^-)$ *to (4.1).*

PROOF. To prove the well-posedness of (4.1) we introduce the following Hilbert space: $V := \widetilde{W}^{1,2}(D^+) \times W^{1,2}(D^-)$ equipped with the following natural norm for our problem:

$$\|u\|_V = \|\nabla u^+\|_{L^2(D^+)} + \|\nabla u^-\|_{L^2(D^-)} + \|u^+ - u^-\|_{L^2(\Gamma)}, \qquad \forall u \in V\,.$$

We write the variational formulation of (4.1) as follows:

Find $u \in V$ such that for all $v := (v^+, v^-) \in V$:

$$\begin{cases} \displaystyle\int_{D^+} k_0 \nabla u^+(x) \cdot \nabla \overline{v}^-(x)\, dx + \int_{D^-} k_0 \nabla u^+(x) \cdot \nabla \overline{v}^-(x)\, dx \\ \qquad\qquad + \dfrac{1}{\beta k_0} \displaystyle\int_\Gamma (u^+ - u^-)\overline{(v^+ - v^-)}\, d\sigma(x) = \frac{1}{k_0} \int_{\partial D} g \overline{v}\, d\sigma(x)\,. \end{cases}$$

Since $\Re(k_0) = \sigma_0 > 0$ and $\Re(\dfrac{1}{\beta k_0}) = \dfrac{\sigma_m \sigma_0 + \varepsilon_m \varepsilon_0}{\delta |k_0|} > 0$, we can apply Lax-Milgram theory to obtain existence and uniqueness of a solution to problem (4.1). □

We conclude this subsection with a few numerical simulations to illustrate the typical profile of the potential u. We consider an elliptic domain D in which lives an elliptic cell. We choose to virtually apply at the boundary of D an electrical current $g = e^{i30r}$.

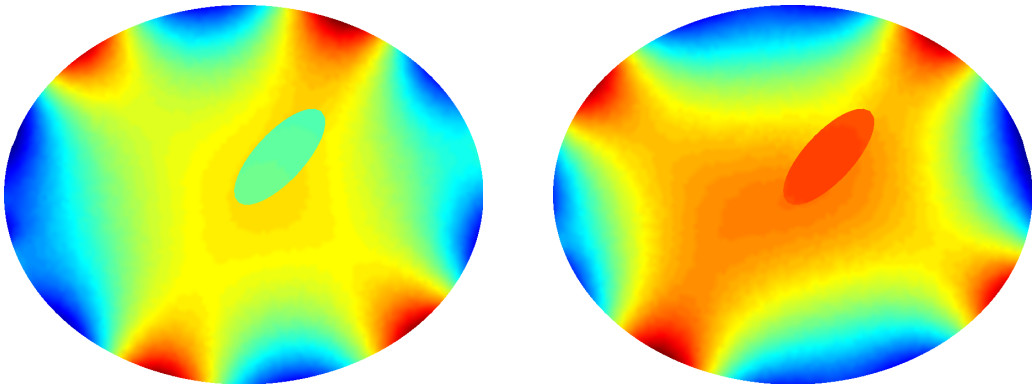

FIGURE 4.2. *Real and imaginary parts of the potential u outside and inside the cell.*

We use for the different parameters the following realistic values:

- the typical size of eukaryotes cells: $\rho \simeq 10 - 100\ \mu$m;
- the ratio between the membrane thickness and the size of the cell: $\delta/\rho = 0.7 \cdot 10^{-3}$;
- the conductivity of the medium and the cell: $\sigma_0 = 0.5\ \text{S.m}^{-1}$;
- the membrane conductivity: $\sigma_m = 10^{-8}\ \text{S.m}^{-1}$;
- the permittivity of the medium and the cell: $\varepsilon_0 = 90 \times 8.85 \cdot 10^{-12}\ \text{F.m}^{-1}$;
- the membrane permittivity: $\varepsilon_m = 3.5 \times 8.85 \cdot 10^{-12}\ \text{F.m}^{-1}$;
- the frequency: $\omega = 10^6$ Hz.

Note that the assumptions of our model $\delta \ll \rho$ and $\sigma_m \ll \sigma_0$ are verified.

The real and imaginary parts of u outside and inside the cell are represented in Figure 4.2.

We can observe that the potential jumps across the cell membrane. We plot the outside and inside gradient vector fields; see Figure 4.3.

4.1.2.3. *Governing Equation.* We denote by Ω_ε^+ the medium outside the cells and Ω_ε^- the medium inside the cells:

$$\Omega_\varepsilon^+ = \Omega \cap \Big(\bigcup_{n \in N_\varepsilon} Y_{\varepsilon,n} \setminus \overline{C_{\varepsilon,n}} \Big), \quad \Omega_\varepsilon^- = \bigcup_{n \in N_\varepsilon} C_{\varepsilon,n}\,.$$

Set $\Gamma_\varepsilon := \bigcup_{n \in N_\varepsilon} \Gamma_{\varepsilon,n}$. By definition, the boundaries $\partial\Omega_\varepsilon^+$ and $\partial\Omega_\varepsilon^-$ of respectively Ω_ε^+ and Ω_ε^- satisfy:

$$\partial\Omega_\varepsilon^+ = \partial\Omega \cup \Gamma_\varepsilon, \quad \partial\Omega_\varepsilon^- = \Gamma_\varepsilon\,.$$

We apply a sinusoidal current $g(x)\sin(\omega t)$ at $x \in \partial\Omega$, where $g \in L_0^2(\partial\Omega)$. The induced time-harmonic potential u_ε in Ω satisfies:

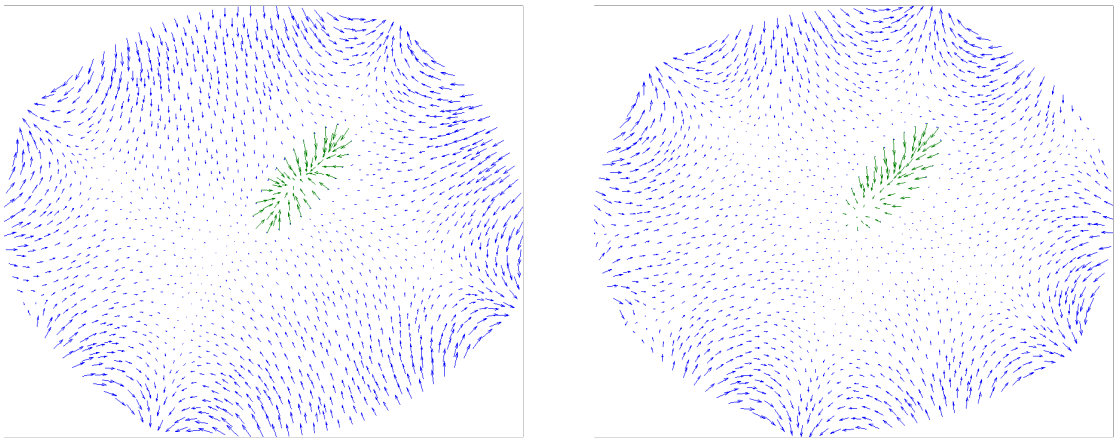

FIGURE 4.3. *Gradient vector fields of the real and imaginary parts of u.*

$$
\left\{
\begin{array}{ll}
\nabla \cdot k_0 \nabla u_\varepsilon^+ = 0 & \text{in } \Omega_\varepsilon^+ , \\
\nabla \cdot k_m \nabla u_\varepsilon^- = 0 & \text{in } \Omega_\varepsilon^- , \\
k_0 \dfrac{\partial u_\varepsilon^+}{\partial \nu} = k_m \dfrac{\partial u_\varepsilon^-}{\partial \nu} & \text{on } \Gamma_\varepsilon , \\
u_\varepsilon^+ - u_\varepsilon^- - \varepsilon \beta k_m \dfrac{\partial u_\varepsilon^+}{\partial \nu} = 0 & \text{on } \Gamma_\varepsilon , \\
k_0 \dfrac{\partial u_\varepsilon^+}{\partial \nu}\Big|_{\partial\Omega} = g, \quad \displaystyle\int_{\partial\Omega} g(x) ds(x) = 0, & \displaystyle\int_{\Omega_\varepsilon^+} u_\varepsilon^+(x) dx = 0 ,
\end{array}
\right. \tag{4.2}
$$

where $u_\varepsilon = \begin{cases} u_\varepsilon^+ & \text{in } \Omega_\varepsilon^+, \\ u_\varepsilon^- & \text{in } \Omega_\varepsilon^-. \end{cases}$

Note that the previously introduced constant β, *i.e.*, the ratio between the thickness of the membrane of C and its admittivity, becomes $\varepsilon\beta$. Because the cells $(C_{\varepsilon,n})_{n\in N_\varepsilon}$ are in squares of size ε, the thickness of their membranes is given by $\varepsilon\delta$ and consequently, a factor ε appears.

4.1.2.4. *Main Results.* We set $Y^+ := Y \setminus \overline{C}$ and $Y^- := C$ and assume that $\text{dist}(Y^-, \partial Y) = O(1)$. We write the solution u_ε as

$$
\forall x \in \Omega \;\; u_\varepsilon(x) = u_0(x) + \varepsilon u_1(x, \frac{x}{\varepsilon}) + o(\varepsilon) \tag{4.3}
$$

with

$$
y \longmapsto u_1(x,y)\, Y\text{-periodic and } u_1(x,y) = \begin{cases} u_1^+(x,y) \text{ in } \Omega \times Y^+ , \\ u_1^-(x,y) \text{ in } \Omega \times Y^- . \end{cases}
$$

Recall the definition of two-scale convergence and a few results of this theory.

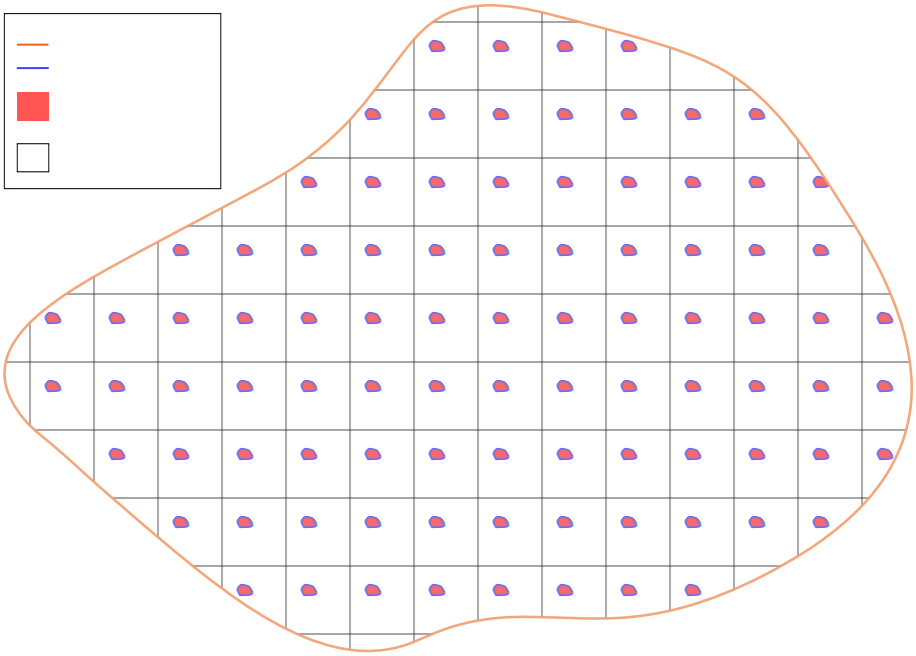

FIGURE 4.4. *Schematic illustration of the periodic medium* Ω.

DEFINITION 4.2. A sequence of functions u_ε in $L^2(\Omega)$ is said to *two-scale converge* to a limit u_0 belonging to $L^2(\Omega \times Y)$ if, for any function ψ in $L^2(\Omega, C_\sharp(Y))$, we have

$$\lim_{\varepsilon \to 0} \int_\Omega u_\varepsilon(x) \psi(x, \frac{x}{\varepsilon}) dx = \int_\Omega \int_Y u_0(x,y) \psi(x,y) dx dy \,.$$

This notion of two-scale convergence makes sense because of the next compactness theorem.

THEOREM 4.3. *From each bounded sequence* u_ε *in* $L^2(\Omega)$, *we can extract a subsequence, and there exists a limit* $u_0 \in L^2(\Omega \times Y)$ *such that this subsequence two-scale converges to* u_0.

The following result holds.

THEOREM 4.4. (i) *The solution* u_ε *to* (4.2) *two-scale converges to* u_0 *and* $\nabla u_\varepsilon(x)$ *two-scale converges to* $\nabla u_0(x) + \chi(Y^+)(y) \nabla_y u_1^+(x,y) + \chi(Y^-)(y) \nabla_y u_1^-(x,y)$, *where* $\chi(Y^\pm)$ *are the characteristic functions of* $Y^\pm$.

(ii) *The function* u_0 *in* (4.3) *is the solution in* $\tilde{W}^{1,2}(\Omega)$ *to the following homogenized problem:*

$$\begin{cases} \nabla \cdot K^* \nabla u_0(x) = 0 & \text{in } \Omega \,, \\ \nu \cdot K^* \nabla u_0 = g & \text{on } \partial\Omega \,, \end{cases} \tag{4.4}$$

where K^*, the effective admittivity of the medium, is given by

$$\forall (i,j) \in \{1,2\}^2, \qquad K^*_{ij} = k_0 \left(\delta_{ij} + \int_Y (\chi(Y^+)\nabla w_i^+ + \chi(Y^-)\nabla w_i^-) \cdot e_j \right), \tag{4.5}$$

and the function $(w_i)_{i=1,2}$ are the solutions of the following cell problems:

$$\begin{cases} \nabla \cdot k_0 \nabla (w_i^+(y) + y_i) = 0 & \text{in } Y^+, \\ \nabla \cdot k_0 \nabla (w_i^-(y) + y_i) = 0 & \text{in } Y^-, \\ k_0 \dfrac{\partial}{\partial \nu}(w_i^+(y) + y_i) = k_0 \dfrac{\partial}{\partial \nu}(w_i^-(y) + y_i) & \text{on } \Gamma, \\ w_i^+ - w_i^- - \beta k_0 \dfrac{\partial}{\partial \nu}(w_i^+(y) + y_i) = 0 & \text{on } \Gamma, \\ y \longmapsto w_i(y) \ Y\text{-periodic}. \end{cases} \tag{4.6}$$

(iii) *Moreover, u_1 can be written as*

$$\forall (x,y) \in \Omega \times Y, \ \ u_1(x,y) = \sum_{i=1}^{2} \frac{\partial u_0}{\partial x_i}(x) w_i(y). \tag{4.7}$$

We define the integral operator $\mathcal{L}_\Gamma : \mathcal{C}^{2,\eta}(\Gamma) \to \mathcal{C}^{1,\eta}(\Gamma)$, with $0 < \eta < 1$ by

$$\mathcal{L}_\Gamma[\varphi](x) = \frac{1}{2\pi} \int_\Gamma \frac{\partial^2 \log|x-y|}{\partial \nu(x) \partial \nu(y)} \varphi(y) ds(y), \quad x \in \Gamma. \tag{4.8}$$

$\mathcal{L}_\Gamma$ is the normal derivative of the double layer potential on $\Gamma = \partial Y^-$.

Since $\mathcal{L}_\Gamma$ is positive, one can prove that the operator $I + \alpha \mathcal{L}_\Gamma : \mathcal{C}^{2,\eta}(\Gamma) \to \mathcal{C}^{1,\eta}(\Gamma)$ is a bounded operator and has a bounded inverse provided that $\Re\, \alpha > 0$.

As the fraction f of the volume occupied by the cells goes to zero, we derive an expansion of the effective admittivity for arbitrary shaped cells in terms of the volume fraction. We refer to the suspension, as periodic dilute. The following theorem holds.

THEOREM 4.5. *The effective admittivity of a periodic dilute suspension admits the following asymptotic expansion:*

$$K^* = k_0 \left(I + fM \left(I - \frac{f}{2} M \right)^{-1} \right) + o(f^2), \tag{4.9}$$

where $\rho = \sqrt{|Y^-|}$, $f = \rho^2$,

$$M = \left(M_{ij} = \beta k_0 \int_{\rho^{-1}\Gamma} \nu_j \psi_i^*(y) ds(y) \right)_{(i,j) \in \{1,2\}^2}, \tag{4.10}$$

and ψ_i^* is defined by

$$\psi_i^* = -\left(I + \beta k_0 \mathcal{L}_{\rho^{-1}\Gamma} \right)^{-1} [\nu_i]. \tag{4.11}$$

Note that $\rho^{-1}\Gamma$ is the rescaled membrane and therefore, M is independent of ρ.

4.1.3. Effective Admittivity for a Dilute Suspension. In general, the effective admittivity given by formula (4.5) can not be computed exactly except for a few configurations. In this section, we consider the problem of determining the effective property of a suspension of cells when the volume fraction $|Y^-|$ goes to zero. In other words, the cells have much less volume than the medium surrounding them. This kind of suspension is called dilute. Many approximations for the effective properties of composites are based on the solution for dilute suspension.

4.1.3.1. *Case of Concentric Circular-Shaped Cells: the Maxwell-Wagner-Fricke Formula.* We consider in this section that the cells are disks of radius r_0. $\rho^{-1}\Gamma$ becomes a circle of radius r_0.

For all $f \in L^2((0,2\pi))$, we introduce the Fourier coefficients:

$$\forall m \in \mathbb{Z}, \quad \hat{f}(m) = \frac{1}{2\pi}\int_0^{2\pi} f(\theta)e^{-im\theta}d\theta\,,$$

and have then for all $\theta \in (0,2\pi)$:

$$f(\theta) = \sum_{m=-\infty}^{\infty} \hat{f}(m)e^{im\theta}\,.$$

For $f \in \mathcal{C}^{2,\eta}(\rho^{-1}\Gamma)$, we obtain after a few computations:

$$\forall \theta \in]0,2\pi[, \quad (I+\beta k_0 \mathcal{L}_{\rho^{-1}\Gamma})^{-1}[f](\theta) = \sum_{m\in\mathbb{Z}\setminus\{0\}} \left(1+\beta k_0 \frac{|m|}{2r_0}\right)^{-1} \hat{f}(m)\, e^{im\theta}\,.$$

For $p = 1,2$, $\psi_p^* = -(I+\beta k_0 \mathcal{L}_{\rho^{-1}\Gamma})^{-1}[\nu_p]$ then have the following expression:

$$\forall \theta \in (0,2\pi), \quad \psi_p^* = -\left(1+\frac{\beta k_0}{2r_0}\right)^{-1}\nu_p\,.$$

Consequently, we get for $(p,q) \in \{1,2\}^2$:

$$M_{pq} = -\delta_{pq}\frac{\beta k_0 \pi r_0}{1+\dfrac{\beta k_0}{2r_0}}\,,$$

and hence,

$$\Im M_{pq} = \delta_{pq}\frac{\pi r_0 \delta\omega(\varepsilon_m\sigma_0 - \varepsilon_0\sigma_m)}{(\sigma_m+\sigma_0\dfrac{\delta}{2r_0})^2 + \omega^2(\varepsilon_m+\varepsilon_0\dfrac{\delta}{2r_0})^2}\,. \tag{4.12}$$

Formula (4.12) is the two-dimensional version of the Maxwell-Wagner-Fricke formula, which gives the effective admittivity of a dilute suspension of spherical cells covered by a thin membrane.

An explicit formula for the case of elliptic cells can be derived by using the spectrum of the integral operator $\mathcal{L}_{\rho^{-1}\Gamma}$, which can be identified by standard Fourier methods.

4.1.3.2. *Debye Relaxation Times.* From (4.12), it follows that the imaginary part of the membrane polarization attains its maximum with respect to the frequency at

$$\frac{1}{\tau} = \frac{\sigma_m+\sigma_0\dfrac{\delta}{2r_0}}{\varepsilon_m+\varepsilon_0\dfrac{\delta}{2r_0}}\,.$$

This dispersion phenomenon due to the membrane polarization is well known and referred to as the β-dispersion. The associated characteristic time τ corresponds to a Debye relaxation time.

For arbitrary-shaped cells, we define the first and second Debye relaxation times, $\tau_i, i = 1, 2$, by

$$\frac{1}{\tau_i} := \arg\max_{\omega} |\lambda_i(\omega)|, \tag{4.13}$$

where $\lambda_1 \leq \lambda_2$ are the eigenvalues of the imaginary part of the membrane polarization tensor $M(\omega)$. Note that if the cell is of circular shape, $\lambda_1 = \lambda_2$.

As it will be shown later, the Debye relaxation times can be used for identifying the microstructure.

4.1.3.3. *Properties of the Membrane Polarization Tensor and the Debye Relaxation Times.* In this subsection, we derive important properties of the membrane polarization tensor and the Debye relaxation times defined respectively by (4.10) and (4.13). In particular, we prove that the Debye relaxation times are invariant with respect to translation, scaling, and rotation of the cell.

First, since the kernel of $\mathcal{L}_{\rho^{-1}\Gamma}$ is invariant with respect to translation, it follows that $M(C, \beta k_0)$ is invariant with respect to translation of the cell C.

Next, from the scaling properties of the kernel of $\mathcal{L}_{\rho^{-1}\Gamma}$ we have

$$M(sC, \beta k_0) = s^2 M(C, \frac{\beta k_0}{s})$$

for any scaling parameter $s > 0$.

Finally, we have

$$M(\mathcal{R}C, \beta k_0) = \mathcal{R} M(C, \beta k_0) \mathcal{R}^T \quad \text{for any rotation } \mathcal{R}\,,$$

where T denotes the transpose.

Therefore, the Debye relaxation times are translation and rotation invariant. Moreover, for scaling, we have

$$\tau_i(hC, \beta k_0) = \tau_i(C, \frac{\beta k_0}{h}), \qquad i = 1, 2, \quad h > 0.$$

Since β is proportional to the thickness of the cell membrane, β/h is nothing else than the real rescaled coefficient β for the cell C. The Debye relaxation times (τ_i) are therefore invariant by scaling.

Since $\mathcal{L}_{\rho^{-1}\Gamma}$ is self-adjoint, it follows that M is symmetric. Finally, we show positivity of the imaginary part of the matrix M for δ small enough.

We consider that the cell contour Γ can be parametrized by polar coordinates. We have, up to $O(\delta^3)$,

$$M + \beta \rho^{-1} |\Gamma| = -\beta^2 \int_{\rho^{-1}\Gamma} n \mathcal{L}_{\rho^{-1}\Gamma}[n]\, ds\,, \tag{4.14}$$

where again we have assumed that $\sigma_0 = 1$ and $\varepsilon_0 = 0$.

Recall that

$$\beta = \frac{\delta \sigma_m}{\sigma_m^2 + \omega^2 \varepsilon_m^2} - i \frac{\delta \omega \varepsilon_m}{\sigma_m^2 + \omega^2 \varepsilon_m^2}\,.$$

Hence, the positivity of $\mathcal{L}_{\rho^{-1}\Gamma}$ yields

$$\Im M \geq \frac{\delta\omega\varepsilon_m}{2\rho(\sigma_m^2+\omega^2\varepsilon_m^2)}|\Gamma|I$$

for δ small enough, where I is the identity matrix.

Finally, by using (4.14) one can see that the eigenvalues of $\Im M$ have one maximum each with respect to the frequency. Let $l_i, i = 1,2, l_1 \geq l_2$, be the eigenvalues of $\int_{\rho^{-1}\Gamma} n\mathcal{L}_{\rho^{-1}\Gamma}[n]ds$. We have

$$\lambda_i = \frac{\delta\omega\varepsilon_m}{\rho(\sigma_m^2+\omega^2\varepsilon_m^2)}|\Gamma| - \frac{2\delta^2\omega\varepsilon_m\sigma_m}{(\sigma_m^2+\omega^2\varepsilon_m^2)^2}l_i, \quad i=1,2\,. \tag{4.15}$$

Therefore, τ_i is the inverse of the positive root of the following polynomial in ω:

$$-\varepsilon_m^4|\Gamma|\omega^4 + 6\delta\varepsilon_m^2\sigma_m l_i\rho\omega^2 + \sigma_m^4|\Gamma|\,.$$

4.1.3.4. *Anisotropy Measure.* Anisotropic electrical properties can be found in biological tissues such as muscles and nerves. In this subsection, based on formula (4.9), we introduce a natural measure of the conductivity anisotropy and derive its dependence on the frequency of applied current. Assessment of electrical anisotropy of muscle may have useful clinical application. Because neuromuscular diseases produce substantial pathological changes, the anisotropic pattern of the muscle is likely to be highly disturbed. Neuromuscular diseases could lead to a reduction in anisotropy for a range of frequencies as the muscle fibers are replaced by isotropic tissue.

Let $\lambda_1 \leq \lambda_2$ be the eigenvalues of the imaginary part of the membrane polarization tensor $M(\omega)$. The function

$$\omega \mapsto \frac{\lambda_1(\omega)}{\lambda_2(\omega)}$$

can be used as a measure of the anisotropy of the conductivity of a dilute suspension. Assume $\varepsilon_0 = 0$. As frequency ω increases, the factor βk_0 decreases. Therefore, for large ω, using the expansions in (4.15) we obtain that

$$\frac{\lambda_1(\omega)}{\lambda_2(\omega)} = 1 + (l_1 - l_2)\frac{2\delta\sigma_m\rho}{(\sigma_m^2+\omega^2\varepsilon_m^2)|\Gamma|} + O(\delta^2)\,, \tag{4.16}$$

where $l_1 \leq l_2$ are the eigenvalues of $\int_{\rho^{-1}\Gamma} n\mathcal{L}_{\rho^{-1}\Gamma}[n]ds$.

Formula (4.16) shows that as the frequency increases, the conductivity anisotropy decreases. The anisotropic information can not be captured for

$$\omega \gg \frac{1}{\varepsilon_m}((l_1 - l_2)\frac{2\delta\sigma_m\rho}{|\Gamma|} - \sigma_m^2)^{1/2}\,.$$

4.1.4. Numerical Simulations. We present in this section some numerical simulations to illustrate the fact that the Debye relaxation times are characteristics of the microstructure of the tissue.

We take realistic values for our parameters, which are the same as those used in Subsection 4.1.2.2 and let the frequency $\omega \in [10^4, 10^9]$ Hz.

We first want to retrieve the invariant properties of the Debye relaxation times. We consider (Figure 4.5) an elliptic cell (in green) that we translate (to obtain the red one), rotate (to obtain the purple one) and scale (to obtain the dark blue one).

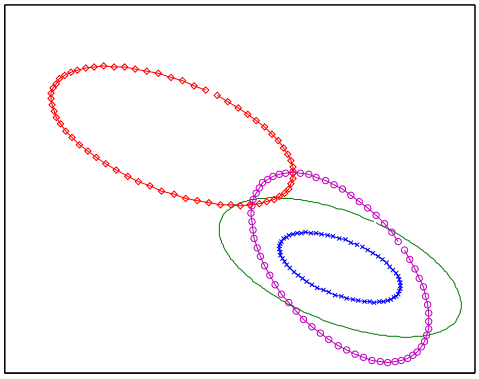

FIGURE 4.5. *An ellipse translated, rotated and scaled.*

We compute the membrane polarization tensor, its imaginary part, and the associated eigenvalues which are plotted as a function of the frequency (Figure 4.6). The frequency is here represented on a logarithmic scale. One can see that for the two eigenvalues the maximum of the curves occurs at the same frequency, and hence that the Debye relaxation times are identical for the four elliptic cells. Note that the red and green curves are even superposed; this comes from the fact that M is invariant by translation.

Next, we are interested in the effect of the shape of the cell on the Debye relaxation times. We consider for this purpose, (Figure 4.7) a circular cell (in green), an elliptic cell (in red) and a very elongated elliptic cell (in blue). We compute similarly as in the preceding case, the polarization tensors associated to the three cells, take their imaginary part and plot the two eigenvalues of these imaginary parts with respect to the frequency. As shown in Figure 4.8, the maxima occur at different frequencies for the first and second eigenvalues. Hence, we can distinguish with the Debye relaxation times between these three shapes.

These simulations prove that the Debye relaxation times are characteristics of the shape and organization of the cells. For a given tissue, the idea is to obtain by spectroscopy the frequency dependence spectrum of its effective admittivity. One then has access to the membrane polarization tensor and the spectra of the eigenvalues of its imaginary part. One compares the associated Debye relaxation times to the known ones of healthy and cancerous tissues at different levels. Then one would be able to know using statical tools with which probability the imaged tissue is cancerous and at which level.

4.2. Plasmonic Nanoparticle Imaging

Plasmon resonant nanoparticles have unique capabilities of enhancing the brightness of light and confining strong electromagnetic fields. A thriving interest for optical studies of plasmon resonant nanoparticles is due to their recently proposed use as labels in molecular biology. New types of cancer diagnostic nanoparticles are constantly being developed. Nanoparticles are also being used in thermotherapy as nanometric heat-generators that can be activated remotely by external electromagnetic fields.

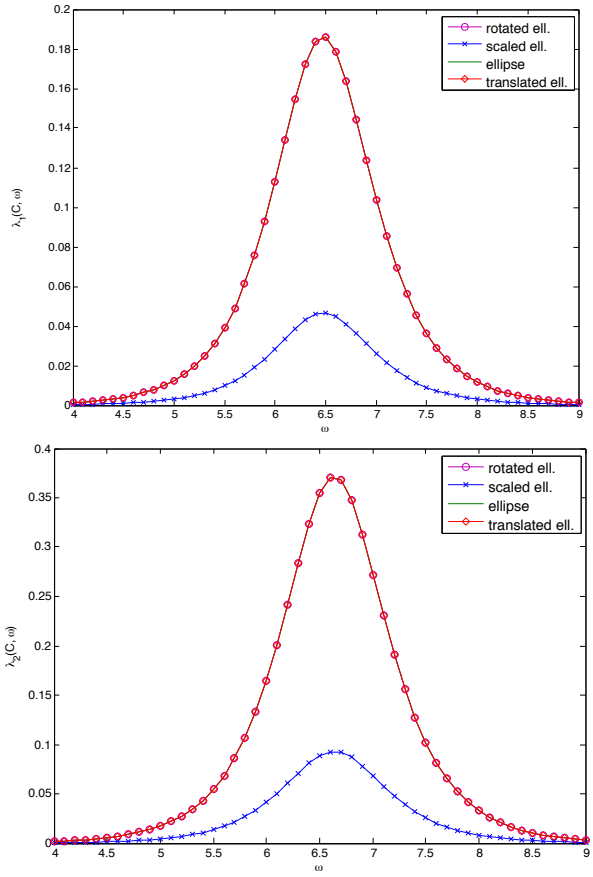

FIGURE 4.6. *Frequency dependence of the eigenvalues of $\Im M$ for the* 4 *ellipses in Figure 4.5.*

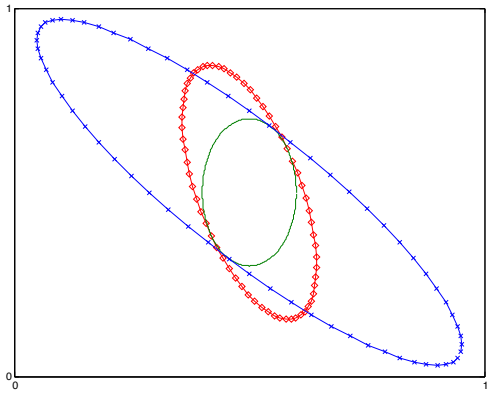

FIGURE 4.7. *A circle, an ellipse and a very elongated ellipse.*

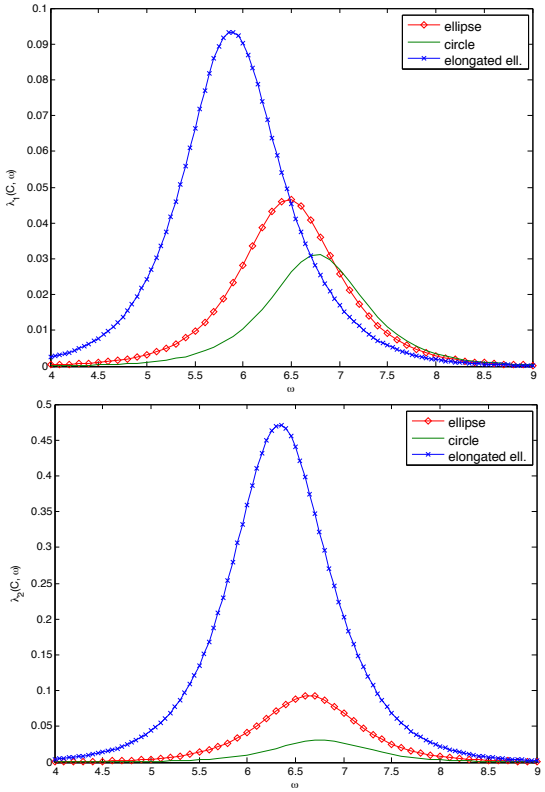

FIGURE 4.8. *Frequency dependence of the eigenvalues of* $\Im M$ *for the* 3 *different cell shapes in Figure 4.7.*

This section is devoted to the mathematical modeling of plasmonic nanoparticles. Its aim is twofold: (i) to mathematically define the notion of plasmonic resonance and to analyze the shift and broadening of the plasmon resonance with changes in size and shape of the nanoparticles and (ii) to study the scattering and absorption enhancements by plasmon resonant nanoparticles and express them in terms of the polarization tensor of the nanoparticle. Optimal bounds on the enhancement factors are also derived. For simplicity, the Helmholtz equation is used to model electromagnetic wave propagation.

According to the quasi-static approximation for small particles, the surface plasmon resonance peak occurs when the particle's polarizability is maximized. Plasmon resonances in nanoparticles can be treated at the quasi-static limit as an eigenvalue problem for the Neumann-Poincaré integral operator, which leads to direct calculation of resonance values of permittivity and optimal design of nanoparticles that resonate at specified frequencies. At this limit, they are size-independent. However, as the particle size increases, they are determined from scattering and absorption blow up and become size-dependent. We precisely quantify the scattering absorption enhancements in plasmonic nanoparticles. We derive new bounds on the enhancement factors given the volume and electromagnetic parameters of the nanoparticles. At the quasi-static limit, we prove that

the averages over the orientation of scattering and extinction cross-sections of a randomly oriented nanoparticle are given in terms of the imaginary part of the polarization tensor. Moreover, we show that the polarization tensor blows up at plasmonic resonances and derive bounds for the absorption and scattering cross-sections. We also prove the blow-up of the first-order scattering coefficients at plasmonic resonances.

4.2.1. Problem Formulation and Some Basic Results. We consider the scattering problem of a time-harmonic wave incident on a plasmonic nanoparticle. For simplicity, we use the Helmholtz equation instead of the full Maxwell equations. The homogeneous medium is characterized by electric permittivity ε_m and magnetic permeability μ_m, while the particle occupying a bounded and simply connected domain $D \Subset \mathbb{R}^3$ of class $\mathcal{C}^{1,\alpha}$ for some $0 < \alpha < 1$ is characterized by electric permittivity ε_c and magnetic permeability μ_c, both of which may depend on the frequency. Assume that $\Re\varepsilon_c < 0, \Im\varepsilon_c > 0, \Re\mu_c < 0, \Im\mu_c > 0$ and define

$$k_m = \omega\sqrt{\varepsilon_m\mu_m}, \quad k_c = \omega\sqrt{\varepsilon_c\mu_c}\,,$$

and

$$\varepsilon_D = \varepsilon_m\chi(\mathbb{R}^3\backslash\bar{D}) + \varepsilon_c\chi(\bar{D}), \quad \mu_D = \varepsilon_m\chi(\mathbb{R}^3\backslash\bar{D}) + \varepsilon_c\chi(D)\,,$$

where χ denotes the characteristic function. Let $u^i(x) = e^{ik_m d\cdot x}$ be the incident wave. Here, ω is the frequency and d is the unit incidence direction. Throughout this paper, we assume that ε_m and μ_m are real and strictly positive and that $\Re k_c < 0$ and $\Im k_c > 0$.

Using dimensionless quantities, we assume that the following set of conditions holds.

CONDITION 4.2.1.1. We assume that the numbers $\varepsilon_m, \mu_m, \varepsilon_c, \mu_c$ are dimensionless and are of order one. We also assume that the particle has size of order one and ω is dimensionless and is of order $o(1)$.

It is worth emphasizing that in the original dimensional variables ω refers to the ratio between the size of the particle and the wavelength. Moreover, the operating frequency varies in a small range and hence, the material parameters ε_c and μ_c can be assumed independent of the frequency.

The scattering problem can be modeled by the following Helmholtz equation

$$\begin{cases} \nabla\cdot\dfrac{1}{\mu_D}\nabla u + \omega^2\varepsilon_D u = 0 \quad \text{in } \mathbb{R}^3\backslash\partial D\,, \\ u_+ - u_- = 0 \quad \text{on } \partial D\,, \\ \dfrac{1}{\mu_m}\dfrac{\partial u}{\partial\nu}\Big|_+ - \dfrac{1}{\mu_c}\dfrac{\partial u}{\partial\nu}\Big|_- = 0 \quad \text{on } \partial D\,, \\ u^s := u - u^i \ \text{ satisfies the Sommerfeld radiation condition.} \end{cases} \tag{4.17}$$

Here, $\partial/\partial\nu$ denotes the normal derivative and the Sommerfeld radiation condition can be expressed in three dimensions as follows:

$$\left|\frac{\partial u}{\partial|x|} - ik_m u\right| \le C|x|^{-2}$$

as $|x| \to +\infty$ for some constant C independent of x.

4.2.2. Scattering and Absorption Enhancements.

4.2.2.1. *Preeliminaries.* To compute the scattering and absorption effects on a plasmonic nanoparticle, we need some definitions and results. For a vector field $U = \mathrm{Re}(u(x)e^{-i\omega t})$, the averaged value of the energy flux vector is

$$\begin{aligned} f(x,t) &= -2\frac{\partial U}{\partial t}\nabla_x U \\ &= -(i\omega)\left(-u(x)e^{ß\omega t} + \overline{u(x)}e^{i\omega t}\right)\left(-\nabla u(x)e^{ß\omega t} + \nabla\overline{u(x)}e^{i\omega t}\right) \\ &= (-i\omega)\left(-u\nabla\overline{u} + \overline{u}\nabla u - u\nabla u e^{-2i\omega t} + \overline{u}\nabla\overline{u}e^{2i\omega t}\right) \end{aligned}$$

And taking the average in time, for a long enough time relative to the wavelength of the incident wave, we obtain

$$F(x) = -i\omega\left(\overline{u(x)}\nabla u(x) - u(x)\nabla\overline{u(x)}\right)$$

Consider the outward flow of energy through the sphere ∂B_R of radius R and center the origin

$$\mathcal{W} = \int_{\partial B} F(x)\cdot\nu(x)d\sigma(x)$$

The total field, decomposed in the incident and scattering parts $u = u^i + u^s$, let us decompose the outward flow in three parts : $\mathcal{W} = \mathcal{W}^i + \mathcal{W}^s + \mathcal{W}'$, where

$$\begin{aligned} \mathcal{W}^i &= -i\omega\int_{\partial B_R}\left(\overline{u}^i(x)\nabla u^i(x) - u^i(x)\nabla\overline{u}^i(x)\right)\cdot\nu(x)d\sigma(x), \\ \mathcal{W}^s &= -i\omega\int_{\partial B_R}(\overline{u}^s(x)\nabla u^s(x) - u^s(x)\nabla\overline{u}^s(x))\cdot\nu(x)d\sigma(x), \\ \mathcal{W}' &= -i\omega\int_{\partial B_R}\left(\overline{u}^i\nabla u^s - u^s\nabla\overline{u}^i - u^i\nabla\overline{u}^s + \overline{u}^s\nabla u^i\right)\cdot\nu(x)d\sigma(x). \end{aligned}$$

Notice that considering the incident wave as a plane wave $u^i(x) = e^{i\omega d\cdot x}$, then $\mathcal{W}^i = 0$ as

$$\begin{aligned} \mathcal{W}^i &= -i\omega\int_{\partial B_R}\overline{u}^i i\omega u^i - u^i\cdot(-i\omega d)\overline{u}^i\nu(x)d\sigma(x) \\ &= \omega^2\int_{\partial B_R} d|u^i|^2 + d|u^i|^2 d\sigma(x) \\ &= 2\omega^2 d\int_{\partial B_R} d\sigma(x) \\ &= 0. \end{aligned}$$

Intuitively speaking, since we are measuring the flux of energy over a sphere, it can be seen that the contribution of a plane wave cancel outs, as the same amount of energy that gets in, gets out. In the presence of absorbing scatterers, by conservation of energy the rate of absorption is $\mathcal{W}^a = -\mathcal{W}$, Hence

$$\mathcal{W}^a + \mathcal{W}^s = -\mathcal{W}'.$$

The term $\mathcal{W}'$ is called the extinction rate and it is the rate at which the energy is removed by the scatterers from the illuminating plane wave.

DEFINITION 4.6. The scattering, absorbtion and extintion cross-sections, respectively Q^s, Q^a, Q^{ext} are

$$Q^s = \frac{\mathcal{W}^s}{V}, \quad Q^a = \frac{\mathcal{W}^a}{V}, \quad Q^{\text{ext}} = \frac{\mathcal{W}^{\text{ext}}}{V},$$

where $V(x) = |u^i(x)\nabla\overline{u}^i(x) - \overline{u}^i(x)\nabla u^i(x)|$. In our case where we have considered a plane wave, this value is constant equal to 2ω.

DEFINITION 4.7. In dimension 3, the scattering amplitude A_∞ is defined as the function that satisfies

$$u^s(x) = u(x) - u^i(x) = \frac{e^{i\omega|x|}}{|x|} A_\infty[\varepsilon,\mu,\omega]\left(\frac{x}{|x|}, d\right) + O\left(\frac{1}{|x|^2}\right)$$

THEOREM 4.8. **Optical theorem** *For dimension 3, and $u^i(x) = e^{i\omega d\cdot x}$ an incident plane wave, we have that*

$$\begin{aligned} Q^{ext}[\varepsilon,\mu,\omega](d) &= Q^s[\varepsilon,\mu,\omega](d) + Q^a[\varepsilon,\mu,\omega](d) \\ &= \frac{4\pi}{\omega} Im\left[A_\infty[\varepsilon,\mu,\omega]\,(d,d)\right] \\ Q^s[\varepsilon,\mu,\omega](d) &= \int_{|\hat{x}|=1} |A_\infty[\varepsilon,\mu,\omega](d,d)|^2\, d\sigma(\hat{x}) \end{aligned}$$

4.2.2.2. *The Quasi-Static Limit*. We start by recalling the small volume expansion in the far-field. The following asymptotic expansion holds.

PROPOSITION 4.9. *Assume that $D = \delta B + z$. As δ goes to zero the scattered field u^s can be written as follows:*

(4.18)

$$\begin{aligned} u^s(x) \quad = \quad & -k_m^2\left(\frac{\varepsilon_c}{\varepsilon_m} - 1\right)|D|\Gamma_{k_m}(x,z)u^i(z) - \nabla_z\Gamma_{k_m}(x,z)\cdot M(\lambda,D)\nabla u^i(z) \\ & + O\left(\frac{\delta^4}{\text{dist}(\lambda,\sigma(\mathcal{K}_D^*))}\right) \end{aligned}$$

for x away from D. Here, $\text{dist}(\lambda,\sigma(\mathcal{K}_D^*))$ *denotes* $\min_j|\lambda-\lambda_j|$ *with λ_j being the eigenvalues of $\mathcal{K}_D^*$.*

Assume for simplicity that $\varepsilon_c = \varepsilon_m$. Consider the scattering amplitude A_∞ (4.7). We explicitly compute it. Take $u^i(x) = e^{ik_m d\cdot x}$ and assume again for simplicity that $z = 0$. Equation (4.18) yields, for $|x| \gg \frac{1}{\omega}$,

$$u^s(x) = \frac{e^{ik_m|x|}}{4\pi|x|} ik_m\left(ik_m\frac{x}{|x|} - \frac{x}{|x|^2}\right)\cdot M(\lambda,D)d + O(\frac{\delta^4}{\text{dist}(\lambda,\sigma(\mathcal{K}_D^*))})\,.$$

Since we are in the far-field region, we can write that, up to an error of order $\delta^4/\text{dist}(\lambda,\sigma(\mathcal{K}_D^*))$,

$$u^s(x) = -k_m^2\frac{e^{ik_m|x|}}{4\pi|x|}\left(\frac{x}{|x|}\cdot M(\lambda,D)d\right) + O\left(\frac{1}{|x|^2}\right)\,. \tag{4.19}$$

In the next proposition we write the extinction and scattering cross-sections, Q_m^{ext} and Q_m^s, in terms of the polarization tensor.

PROPOSITION 4.10. *The leading-order term (as δ goes to zero) of the average over the orientation of the extinction cross-section of a randomly oriented nanoparticle is given by*

$$Q_m^{ext} = -\frac{4\pi k_m}{3}\Im\left[\text{trace}M(\lambda, D)\right], \tag{4.20}$$

where trace *denotes the trace of a matrix. The leading-order term of the average over the orientation scattering cross-section of a randomly oriented nanoparticle is given by*

$$Q_m^{s} = \frac{k_m^4}{9\pi}\left|\text{trace}M(\lambda, D)\right|^2. \tag{4.21}$$

PROOF. Remark from (4.19) that the scattering amplitude A_∞ in the case of a plane wave illumination is given by

$$A_\infty\left(\frac{x}{|x|}, d\right) = -\frac{k_m^2}{4\pi}\frac{x}{|x|}\cdot M(\lambda, D)d. \tag{4.22}$$

Using Theorem 4.8, we can see that for a given orientation

$$Q^{ext} = -4\pi k_m \Im\left[d\cdot M(\lambda, D)d\right].$$

Therefore, if we integrate Q^{ext} over all illuminations we find that

$$Q_m^{ext} = -k_m\Im\left[\int_S d\cdot M(\lambda, D)d\, d\sigma(d)\right].$$

Since $\Im M(\lambda, D)$ is symmetric, it can be written as $\Im M(\lambda, D) = P^t N(\lambda)P$, where P is unitary and N is diagonal and real. Then, by the change of variables $d = P^t x$ and using spherical coordinates, it follows that

$$Q_m^{ext} = -k_m\left[\int_S x\cdot N(\lambda)x d\sigma(x)\right],$$

and therefore,

$$Q_m^{ext} = -\frac{4\pi k_m}{3}\left[\text{trace}N(\lambda)\right] = -\frac{4\pi k_m}{3}\Im\left[\text{trace}M(\lambda, D)\right]. \tag{4.23}$$

Now, we compute the averaged scattering cross-section. Let $\Re M(\lambda, D) = \widetilde{P}^t\widetilde{N}(\lambda)\widetilde{P}$ where $\widetilde{P}$ is unitary and $\widetilde{N}$ is diagonal and real. We have

$$\begin{aligned} Q_m^{s} &= \frac{k_m^4}{16\pi^2}\iint_{S\times S}\left|x\cdot M(\lambda, D)d\right|^2 d\sigma(x)\, d\sigma(d), \\ &= \frac{k_m^4}{16\pi^2}\left[\iint_{S\times S}\left|\widetilde{x}\cdot N(\lambda)\widetilde{d}\right|^2 d\sigma(\widetilde{x})d\sigma(\widetilde{d}) + \iint_{S\times S}\left|\widetilde{x}\cdot \widetilde{N}(\lambda)\widetilde{d}\right|^2 d\sigma(\widetilde{x})\, d\sigma(\widetilde{d})\right]. \end{aligned}$$

Then a straightforward computation in spherical coordinates gives

$$Q_m^{s} = \frac{k_m^4}{9\pi}\left|\text{trace}M(\lambda, D)\right|^2,$$

which completes the proof. □

From Theorem 4.8, we obtain that the averaged absorption cross-section is given by

$$Q_m^{a} = -\frac{4\pi k_m}{3}\Im\left[\text{trace}M(\lambda, D)\right] - \frac{k_m^4}{9\pi}\left|\text{trace}M(\lambda, D)\right|^2.$$

Therefore Q_m^a blows up at plasmonic resonances, as the trace of the polarization tensor does.

REMARK 4.11. Notice that both the absorption and the scattering cross sections of the nanoparticle explodes when there is plasmonic resonances, this counter intuitive effect is interesting by itself as the amount of light energy emitted to it is not being augmented. This is why it is possible to both heat the nanoparticle for treatment purposes and to measure the scattering for imaging.

4.2.3. An Upper Bound for the Averaged Extinction Cross-Section. The goal of this section is to derive an upper bound for the modulus of the averaged extinction cross-section Q_m^{ext} of a randomly oriented nanoparticle. Most of the details and proofs will be omitted as being way too lengthy, for further reference see the course notes.

Recall that the entries $M_{lm}(\lambda, D)$ of the polarization tensor $M(\lambda, D)$ are given by

$$M_{lm}(\lambda, D) := \int_{\partial D} x_l (\lambda I - \mathcal{K}_D^*)^{-1}[\nu_m](x)\, d\sigma(x)\,. \tag{4.24}$$

For a $\mathcal{C}^{1,\alpha}$ domain D in $\mathbb{R}^d$, $\mathcal{K}_D^*$ is compact and self-adjoint in $\mathcal{H}^*$ (defined in the course). Thus, we can write

$$(\lambda I - \mathcal{K}_D^*)^{-1}[\psi] = \sum_{j=0}^{\infty} \frac{(\psi, \varphi_j)_{\mathcal{H}^*} \otimes \varphi_j}{\lambda - \lambda_j}\,,$$

with (λ_j, φ_j) being the eigenvalues and eigenvectors of $\mathcal{K}_D^*$ in $\mathcal{H}^*$. Hence, the entries of the polarization tensor M can be decomposed as

$$M_{lm}(\lambda, D) = \sum_{j=1}^{\infty} \frac{\alpha_{lm}^{(j)}}{\lambda - \lambda_j}\,, \tag{4.25}$$

where $\alpha_{lm}^{(j)} := (\nu_m, \varphi_j)_{\mathcal{H}^*} (\varphi_j, x_l)_{-\frac{1}{2},\frac{1}{2}}$. Note that $(\nu_m, \chi(\partial D))_{-\frac{1}{2},\frac{1}{2}} = 0$. So, considering the fact that $\lambda_0 = 1/2$, we have $(\nu_m, \varphi_0)_{\mathcal{H}^*} = 0$ and so, $\alpha_{lm}^{(0)} = 0$.

The following lemmas are useful for us.

LEMMA 4.12. *We have*

$$\alpha_{l,l}^{(j)} \geq 0, \quad j \geq 1\,.$$

LEMMA 4.13. *Let*

$$M_{lm}(\lambda, D) = \sum_{j=1}^{\infty} \frac{\alpha_{l,m}^{(j)}}{\lambda - \lambda_j}$$

be the (l, m)-entry of the polarization tensor M associated with a $\mathcal{C}^{1,\alpha}$ domain $D \Subset \mathbb{R}^d$. Let δ_{lm} denote the Kronecker symbol. Then, the following properties hold:

(i)

$$\sum_{j=1}^{\infty} \alpha_{l,m}^{(j)} \quad = \quad \delta_{lm} |D|\,;$$

(ii)

$$\sum_{j=1}^{\infty} \lambda_i \sum_{l=1}^{d} \alpha_{l,l}^{(j)} \quad = \quad \frac{(d-2)}{2}|D|\,;$$

(iii)

$$\sum_{j=1}^{\infty} \lambda_j^2 \sum_{l=1}^{d} \alpha_{l,l}^{(j)} \quad = \quad \frac{(d-4)}{4}|D| + \sum_{l=1}^{d} \int_D |\nabla \mathcal{S}_D[\nu_l]|^2 dx\,.$$

Let $\lambda = \lambda' + i\lambda''$. We have

$$\left|\Im(\text{trace}(M(\lambda, D)))\right| = \sum_{j=1}^{\infty} \frac{|\lambda''| \sum_{l=1}^{d} \alpha_{l,l}^{(j)}}{(\lambda' - \lambda_j)^2 + \lambda''^2}. \tag{4.26}$$

For $d = 2$ the spectrum $\sigma(\mathcal{K}_D^*)\backslash\{1/2\}$ is symmetric. For $d = 3$ this is no longer true. Nevertheless, for our purposes, we can assume that $\sigma(\mathcal{K}_D^*)\backslash\{1/2\}$ is symmetric by defining $\alpha_{l,l}^{(j)} = 0$ if λ_j is not in the original spectrum.

THEOREM 4.14. *Let $M(\lambda, D)$ be the polarization tensor associated with a $\mathcal{C}^{1,\alpha}$ domain $D \Subset \mathbb{R}^d$ with $\lambda = \lambda' + i\lambda''$ such that $|\lambda''| \ll 1$ and $|\lambda'| < 1/2$. Then,*

$$\begin{aligned}\left|\Im(\text{trace}(M(\lambda, D)))\right| \leq & \frac{d|\lambda''||D|}{\lambda''^2 + 4\lambda'^2} \\ & + \frac{1}{|\lambda''|(\lambda''^2 + 4\lambda'^2)} \left(d\lambda'^2|D| + \frac{(d-4)}{4}|D| + \sum_{l=1}^{d} \int_D |\nabla \mathcal{S}_D[\nu_l]|^2 dx + 2\lambda' \frac{(d-2)}{2}|D| \right) \\ & + O(\frac{\lambda''^2}{4\lambda'^2 + \lambda''^2})\,.\end{aligned}$$

The bound in the above theorem depends not only on the volume of the particle but also on its geometry.

4.2.3.1. *Bound for ellipses.* If D is an ellipse whose semi-axes are on the x_1- and x_2- axes and of length a and b, respectively, then its polarization tensor takes the form,

$$M(\lambda, D) = \begin{pmatrix} \dfrac{|D|}{\lambda - \frac{1}{2}\frac{a-b}{a+b}} & 0 \\ 0 & \dfrac{|D|}{\lambda + \frac{1}{2}\frac{a-b}{a+b}} \end{pmatrix}. \tag{4.27}$$

On the other hand, in $\mathcal{H}^*(\partial D)$,

$$\sigma(\mathcal{K}_D^*)\backslash\{1/2\} = \left\{ \pm\frac{1}{2}\left(\frac{a-b}{a+b}\right)^j, \quad j = 1, 2, \dots \right\}.$$

Then, from (4.25), we also have

$$M(\lambda, D) = \begin{pmatrix} \sum_{j=1}^{\infty} \frac{\alpha_{1,1}^{(j)}}{\lambda - \frac{1}{2}\left(\frac{a-b}{a+b}\right)^j} & \sum_{j=1}^{\infty} \frac{\alpha_{1,2}^{(j)}}{\lambda - \frac{1}{2}\left(\frac{a-b}{a+b}\right)^j} \\ \sum_{j=1}^{\infty} \frac{\alpha_{1,2}^{(j)}}{\lambda - \frac{1}{2}\left(\frac{a-b}{a+b}\right)^j} & \sum_{j=1}^{\infty} \frac{\alpha_{2,2}^{(j)}}{\lambda - \frac{1}{2}\left(\frac{a-b}{a+b}\right)^j} \end{pmatrix}.$$

Let $\lambda_1 = \dfrac{1}{2}\dfrac{a-b}{a+b}$ and $\mathcal{V}(\lambda_j) = \{i \in \mathbb{N} \text{ such that } \mathcal{K}_D^*[\varphi_i] = \lambda_j \varphi_i\}$. It is clear now that

$$\sum_{i \in \mathcal{V}(\lambda_1)} \alpha_{1,1}^{(i)} = \sum_{i \in \mathcal{V}(-\lambda_1)} \alpha_{2,2}^{(i)} = |D|, \quad \sum_{i \in \mathcal{V}(\lambda_j)} \alpha_{1,1}^{(i)} = \sum_{i \in \mathcal{V}(-\lambda_j)} \alpha_{2,2}^{(i)} = 0 \tag{4.28}$$

for $j \geq 2$ and

$$\sum_{i \in \mathcal{V}(\lambda_j)} \alpha_{1,2}^{(i)} = 0$$

for $j \geq 1$. taking all together , we can conclude that

$$|\Im(\mathrm{Tr}(M(\lambda, D)))| \leq \frac{|\lambda''|}{2} \sum_{j=1}^{\infty} \frac{4\lambda'^2 \beta^{(j)} + \lambda''^2(\beta^{(j)} + \beta^{(j)})}{\lambda''^2(4\lambda'^2 + \lambda''^2)} + O(\frac{\lambda''^2}{4\lambda'^2 + \lambda''^2}).$$

Note that for for any ellipse $\widetilde{D}$ of semi-axes of length a and b, $\Im(\mathrm{trace}(M(\lambda, \widetilde{D}))) = \Im(\mathrm{trace}(M(\lambda, D)))$. Then using Lemma 4.13 we obtain the following result.

COROLLARY 4.14.1. For any ellipse $\widetilde{D}$ of semi-axes of length a and b, we have

$$|\Im(\mathrm{trace}(M(\lambda, \widetilde{D})))| \leq \frac{|\widetilde{D}|4\lambda'^2}{|\lambda''|(\lambda''^2 + 4\lambda'^2)} + \frac{2|\lambda''||\widetilde{D}|}{\lambda''^2 + 4\lambda'^2} + O(\frac{\lambda''^2}{4\lambda'^2 + \lambda''^2}). \tag{4.29}$$

Figure 4.9 shows (4.29) and the average extinction of two ellipses of semi-axis a and b, where the ratio $a/b = 2$ and $a/b = 4$, respectively.

We can see from (4.26), Lemma 4.12 and the first sum rule in Lemma 4.13 that for an arbitrary shape B, $|\Im(\mathrm{trace}(M(\lambda, B)))|$ is a convex combination of $\frac{|\lambda''|}{(\lambda' - \lambda_j)^2 + \lambda''^2}$ for $\lambda_j \in \sigma(\mathcal{K}_B^*) \backslash \{1/2\}$. Since ellipses put all the weight of this convex combination in $\pm\lambda_1 = \pm\frac{1}{2}\frac{a-b}{a+b}$, we have for any ellipse $\widetilde{D}$ and any shape B such that $|B| = |\widetilde{D}|$,

$$|\Im(\mathrm{trace}(M(\lambda^*, B)))| \leq |\Im(\mathrm{trace}(M(\lambda^*, \widetilde{D})))|$$

with

$$\lambda^* = \pm\frac{1}{2}\frac{a-b}{a+b} + i\lambda''.$$

Thus, bound (4.29) applies for any arbitrary shape B in dimension two. This implies that, for a given material and a given desired resonance frequency ω^*, the optimal shape for the extinction resonance (in the quasi-static limit) is an ellipse of semi-axis a and b such that $\lambda'(\omega^*) = \pm\frac{1}{2}\frac{a-b}{a+b}$.

As conclusion, this bound allows us to conclude when a shape is optimal for the desired plasmonic resonance at a given size.

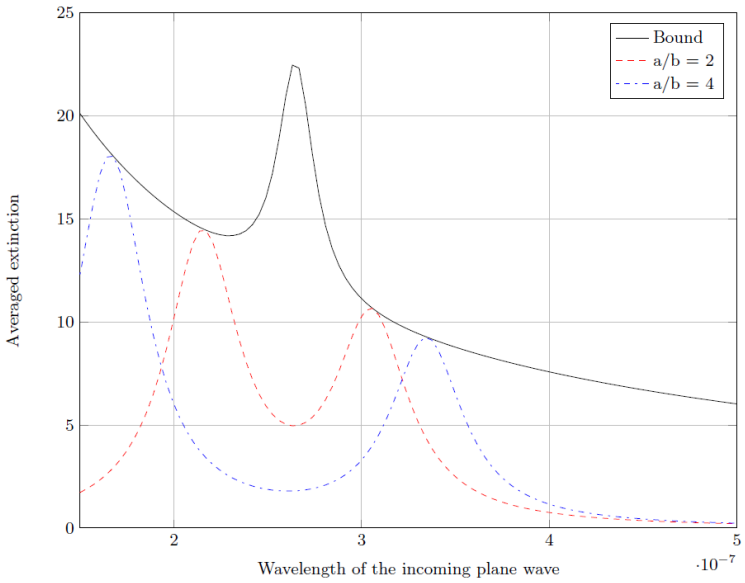

FIGURE 4.9. Optimal bound for ellipses.